

# DESIGN AND FABRICATION OF PEROVSKITE SOLAR CELLS FOR TANDEM STRUCTURES



Miss Kwanruthai Butsriruk

จุฬาลงกรณ์มหาวิทยาลัย  
CHULALONGKORN UNIVERSITY

A Dissertation Submitted in Partial Fulfillment of the Requirements  
for the Degree of Doctor of Philosophy in Physics

Department of Physics

FACULTY OF SCIENCE

Chulalongkorn University

Academic Year 2021

Copyright of Chulalongkorn University

การออกแบบและประดิษฐ์เซลล์สุริยะเพอรอฟสไกต์สำหรับโครงสร้างแบบแทนเดม



วิทยานิพนธ์นี้เป็นส่วนหนึ่งของการศึกษาตามหลักสูตรปริญญาวิทยาศาสตรดุษฎีบัณฑิต

สาขาวิชาฟิสิกส์ ภาควิชาฟิสิกส์

คณะวิทยาศาสตร์ จุฬาลงกรณ์มหาวิทยาลัย

ปีการศึกษา 2564

ลิขสิทธิ์ของจุฬาลงกรณ์มหาวิทยาลัย

Thesis Title                    DESIGN AND FABRICATION OF  
PEROVSKITE SOLAR CELLS FOR  
TANDEM STRUCTURES  
By                                    Miss Kwanruthai Butsriruk  
Field of Study                    Physics  
Thesis Advisor                    Assistant Professor SOJIPHONG  
    CHATRAPHORN, Ph.D.  
Thesis Co Advisor                Assistant Professor Thiti Taychatanapat, Ph.D.

---

Accepted by the FACULTY OF SCIENCE, Chulalongkorn  
University in Partial Fulfillment of the Requirement for the Doctor of  
Philosophy

..... Dean of the FACULTY OF  
SCIENCE  
(Professor POLKIT SANGVANICH, Ph.D.)

#### DISSERTATION COMMITTEE

..... Chairman  
(Associate Professor Thiti Bovornratanaraks,  
Ph.D.)

..... Thesis Advisor  
(Assistant Professor SOJIPHONG  
CHATRAPHORN, Ph.D.)

..... Thesis Co-Advisor  
(Assistant Professor Thiti Taychatanapat, Ph.D.)

..... Examiner  
(Assistant Professor Salinporn Kittiwatanakul,  
Ph.D.)

..... Examiner  
(Associate Professor TONPHONG  
KAEWKONGKA, Ph.D.)

..... External Examiner  
(Associate Professor Rachsak Sakdanuphab,  
Ph.D.)

ขวัญฤทัย บุตรศรีรักษ์ : การออกแบบและประดิษฐ์เซลล์สุริยะเพอรอฟสไกต์สำหรับโครงสร้างแบบแทนเดม . ( DESIGN AND FABRICATION OF PEROVSKITE SOLAR CELLS FOR TANDEM STRUCTURES ) อ.ที่ปรึกษาหลัก : ผศ. ดร. โสจิพงษ์ ฉัตรารักษ์, อ.ที่ปรึกษาร่วม : ผศ. ดร. ธิติ เตชชนพัฒน์

ในวิทยานิพนธ์นี้ มีการอธิบายกระบวนการผลิตสำหรับการผลิตเซลล์สุริยะชนิดเพอรอฟสไกต์ (PSCs) ที่เหมาะสมสำหรับโครงสร้างแบบแทนเดม เราพบว่าเงื่อนไขต่างๆ ของการผลิตมีผลกระทบต่อคุณสมบัติของฟิล์มคูดกลืนแสงเพอรอฟสไกต์ และประสิทธิภาพการแปลงพลังงาน (PCE) ของ PSCs อย่างมีนัยสำคัญ เพื่อให้ได้คุณภาพที่ดีที่สุด ฟิล์มคูดกลืนแสงเพอรอฟสไกต์ ถูกเตรียมโดยการเคลือบแบบหมุนเหวี่ยงด้วยสองขั้นตอน จากสารตั้งต้น  $\text{PbI}_2$  และ  $\text{CH}_3\text{NH}_3\text{I}$  (MAI) และเซลล์สุริยะให้ PCE สูงสุด 17.2% และ 15.4% สำหรับ PSCs แบบปกติและแบบกลับด้านตามลำดับ PSCs เหล่านี้สามารถนำไปใช้กับการออกแบบ และการผลิตเซลล์สุริยะแบบแทนเดม (TSC) ที่ประกอบด้วย PSCs เป็นเซลล์ย่อยด้านบน และเซลล์สุริยะชนิดคอปเปอร์อินเดียมแกลเลียมไดซัลไฟด์ ( $\text{Cu}(\text{In}, \text{Ga})\text{Se}_2$  หรือ CIGS) เป็นเซลล์ย่อยด้านล่าง ในวิทยานิพนธ์นี้ TSCs ถูกประดิษฐ์ขึ้นเป็นเซลล์สุริยะแบบแทนเดมทั้งแบบสองชั้น (2T) และแบบสี่ชั้น (4T) ซึ่ง PSCs ทั้งแบบปกติ และแบบกลับด้านทำหน้าที่เป็นเซลล์ย่อยด้านบนสุด ได้รับการพัฒนาด้วยกลยุทธ์หลายประการ สำหรับเซลล์สุริยะแบบ 4T แทนเดมได้รับ PCE 22.6% และ 17.6% โดยเซลล์ย่อยด้านบนเป็น PSCs แบบปกติ และแบบกลับด้านตามลำดับ



สาขาวิชา ฟิสิกส์

ลายมือชื่อนิพนธ์

ปีการศึกษา 2564

.....  
ลายมือชื่อ อ.ที่ปรึกษาหลัก

.....  
ลายมือชื่อ อ.ที่ปรึกษาร่วม

.....

## 5872845023 : MAJOR PHYSICS

KEYWORD:

RD:

Kwanruthai Butsriruk : DESIGN AND FABRICATION OF PEROVSKITE SOLAR CELLS FOR TANDEM STRUCTURES . Advisor: Asst. Prof. SOJIPHONG CHATRAPHORN, Ph.D. Co-advisor: Asst. Prof. Thiti Taychatanapat, Ph.D.

In this thesis, fabrication processes for making perovskite solar cells (PSCs) suitable for tandem structures are described. We find that different conditions of fabrication significantly affect the perovskite absorber film properties and power conversion efficiency (PCE) of PSCs. To achieve the best quality, perovskite absorber films were prepared by two-step spin coating from  $\text{PbI}_2$  and  $\text{CH}_3\text{NH}_3\text{I}$  (MAI) precursors, and solar cell yielded a maximum PCE of 17.2% and 15.4% for a normal and an inverted PSCs, respectively. These PSCs can be applied to the design and fabrication of tandem solar cells (TSCs) that consist of PSCs as a top subcell and copper indium gallium diselenide ( $\text{Cu}(\text{In}, \text{Ga})\text{Se}_2$  or CIGS) solar cells as a bottom subcell. In this thesis, TSCs are fabricated as both two-terminal (2T) and four-terminal (4T) tandem solar cells. Both normal and inverted perovskite, which act as a top subcell, are developed with several strategies. For a 4T tandem solar cell, a PCE of 22.6% and 17.6% are achieved with the top subcells being the normal and inverted PSCs, respectively.

จุฬาลงกรณ์มหาวิทยาลัย  
CHULALONGKORN UNIVERSITY

Field of Study:	Physics	Student's Signature
Academic Year:	2021	.....
		Advisor's Signature
		.....
		Co-advisor's Signature
		.....

## ACKNOWLEDGEMENTS

First of all, thanks a lot to my parents for giving me encouragement, enthusiasm, and invaluable assistance. Without all this, I might not be able to complete this subject property.

Second, my deepest thanks to Asst. Prof. Dr. Sojiphong Chatraphorn as supervisor, who supported me with valuable teaching, suggestions, advising, and showing several knowledge and different processes of this study. He helped all the times when advised, and he gave the right direction toward completion of this thesis and gave me the possibility to complete my project. Whenever I have any doubts, he will be there to answer my questions paternally and help me clear up these matters. His cooperation was very precious to me, without which I would have been incapable of producing this dissertation work.

Thirdly, I would like to thank Asst. Prof. Dr. Thiti Taychatanaphat as co-adviser for giving me the opportunity and guidance.

Besides that, I would like to thank Mr. Pornsak Panchawirat as a staff member in the Semiconductor Physics Research Laboratory (SPRL) who helped with scanning electron microscope (SEM) measurements for my results in this project.

Last but not least, I'd like to thank Mr. Passakorn Phiromruk, who has contributed, pushed, and supported me in various ways. He is my kind younger brother in my laboratory.

Kwanruthai Butsriruk

## TABLE OF CONTENTS

	<b>Page</b>
.....	iii
ABSTRACT (THAI) .....	iii
.....	iv
ABSTRACT (ENGLISH).....	iv
ACKNOWLEDGEMENTS.....	v
TABLE OF CONTENTS.....	vi
LIST OF TABLES.....	x
LIST OF FIGURES .....	xii
CHAPTER I.....	1
INTRODUCTION .....	1
1.1 Objectives of the research.....	5
1.2 Scope of the research .....	5
CHAPTER II.....	6
LITERATURE REVIEWS .....	6
2.1 ABX <sub>3</sub> perovskite materials group for Single-junction solar cells.....	6
2.1.1 Halide anions for X-Site replacing.....	8
2.1.2 Metal cation for B-Site replacement .....	9
2.1.3 Organic or inorganic cation for A-Site replacement .....	9
2.2 Conventional PSCs and Inverted PSCs .....	9
2.3 CuInGaSe <sub>2</sub> (CIGS) solar cells .....	10
2.4 Tandem cell .....	12
2.4.1 Perovskite-Based Double-Junction Solar Cells.....	12
2.4.2 Perovskite/Chalcogenide Cells.....	15
CHAPTER III .....	19
THEORY .....	19

3.1 Band gap energy ( $E_g$ ).....	19
3.2 P-N junction.....	20
3.3 I-V curve.....	22
3.3.1 Parameters for evaluating solar cells.....	23
3.3.1.1 Current-voltage (IV) curve.....	23
3.3.1.2 Short circuit current density ( $J_{sc}$ ).....	24
3.3.1.3 Open circuit voltage ( $V_{oc}$ ).....	24
3.3.1.4 Power conversion efficiency (PCE) and fill factor (FF).....	24
3.3.1.5 Parasitic resistances.....	25
3.4 Hysteresis and charge recombination.....	26
CHAPTER IV.....	28
FILM FABRICATION AND CHARACTERIZATION.....	28
4.1 Main deposition technologies of thin-film.....	28
4.1.1 Solution deposition methods for perovskite device fabrication.....	28
4.1.2 Thermal Evaporation.....	31
4.2 Materials for PSCs fabrication.....	32
4.3 Characterization techniques.....	33
4.3.1 Device characterization.....	33
4.3.2 Absorption and transmission measurements.....	33
4.3.3 Atomic force microscope (AFM).....	34
4.3.4 Contact angle.....	35
4.3.5 External quantum efficiency (EQE) measurement.....	36
4.3.6 Scanning electron microscopy (SEM).....	37
4.4 Cleaning the surface of FTO glass substrate.....	39
4.5 Etching FTO.....	40
4.6 UV-Ozone cleaner.....	40
CHAPTER V.....	42
EXPERIMENTS, RESULTS AND DISCUSSION.....	42
5.1 Normal structure PSCS.....	42



5.1.1 Finding suitable $Mp-TiO_2$ on normal PSCs .....	42
<i>Results and discussions of finding suitable <math>Mp-TiO_2</math> on normal PSCs</i> .....	44
5.1.2 Dissolved $PbI_2$ with different solvents .....	48
<i>Results and discussions of dissolved <math>PbI_2</math> with different solvents</i> .....	49
5.1.3 An anti-solvent .....	50
<i>Results and discussions of an anti-solvent</i> .....	51
5.2 Inverted structure PSCs .....	55
5.2.1 HTM options .....	55
5.2.1.1 Concentration and thickness of $NiO_x$ .....	55
<i>Results and discussions of concentration and thickness of <math>NiO_x</math></i> .....	55
5.2.1.2 Different products of PEDOT: PSS.....	57
<i>Results and discussions of different products of PEDOT: PSS</i> .....	60
5.2.1.3 Suitable condition for PTAA.....	61
<i>Results and discussions of suitable condition for PTAA</i> .....	61
5.2.2 Metal contact .....	63
<i>Results and discussions of metal contact</i> .....	63
5.2.3 Washing surface of PTAA .....	65
<i>Results and discussions of washing surface of PTAA</i> .....	67
5.2.4 Large active area ( $0.2\text{ cm}^2$ ) preparation of inverted PSCs for tandem solar cells fabrication .....	70
<i>Results and discussions of large active area (<math>0.2\text{ cm}^2</math>) preparation of inverted PSCs for tandem solar cells fabrication</i> .....	71
5.3 Four-terminal (4T) PSCs-CIGS tandem solar cells .....	72
<i>Results and discussions of four-terminal (4T) PSCs-CIGS tandem solar cells</i> .....	73
CHAPTER VI.....	79
CONCLUSIONS.....	79
APPENDICES .....	81
APPENDIX A.....	81
List of Symbols and Abbreviations .....	81
REFERENCES .....	85

VITA.....92



จุฬาลงกรณ์มหาวิทยาลัย  
**CHULALONGKORN UNIVERSITY**

## LIST OF TABLES

	<b>Page</b>
Table 1. Disadvantages and advantages of 2T and 4T tandem solar cells[6, 7].	5
Table 2. Responding between thickness and current of several materials.	17
Table 3. Comparison of scalable solution processing for perovskite device.	30
Table 4. Materials used in the experiment of the conventional and inverted structure.	32
Table 5. All photovoltaic parameters of different precursor solutions, $\text{M}_p\text{-TiO}_2$ : Ethanol, 1: 4 ( $\text{M}_4$ ), 1: 5 ( $\text{M}_5$ ), and 1: 7 ( $\text{M}_7$ ) v/v, on the inverted device.	46
Table 6. Photovoltaic parameters of different $\text{M}_p\text{-TiO}_2$ dilutions, such as $\text{M}_4$ , $\text{M}_5$ , and $\text{M}_7$ , with spin speeds of 5000, 4000, and 3000 rpm for 30 sec.	48
Table 7. Summary of the photovoltaic parameters derived from J-V measurements along with activation energy for using pure DMF, DMF and DMSO in a 1:4 ratio, and DMF and DMSO in a 4:1 ratio (showing the best performance).	50
Table 8. Device performances of the inverted perovskite cells using different anti-solvents.	53
Table 9. All photovoltaic parameters result by the J-V measurement.	57
Table 10. All photovoltaic parameters result by the J-V measurement.	60
Table 11. Device performance of the inverted perovskite cells using PTAA HTL with different spin speeds between 2000 and 3000 rpm for 30 s.	62
Table 12. Conductivity value for Al, Au and Ag metal [90].	64
Table 13. Device performance of the inverted perovskite cells using different metal contacts.	65
Table 14. Statistical values of solar cell photovoltaic parameters displaying the average values and standard deviations and the maximum values (in the parentheses) of the inverted PSCs fabricated from pristine and post-treated PTAA (batch of 25 devices each).	70
Table 15. Statistical values of solar cell photovoltaic parameters displaying the average values and standard deviations and the maximum values (in the parentheses) of the inverted PSCs fabricated from pristine and post-treated PTAA (batch of 15 devices each).	72

Table 16. Device performances of single-junction and 4T tandem solar cells.....78



## LIST OF FIGURES

	Page
Figure 1. Publication year for PV devices [1].....	1
Figure 2. Crystal structure of perovskite $ABX_3$ [3]. .....	2
Figure 3.(a) Schematic illustration of a perovskite/silicon tandem artifact (b) Photons emitted through the perovskite cell first can be mostly absorbed in the visible region of the solar spectrum. The near-infrared light (NIR) part is harvested via the silicon solar cells [1]. .....	3
Figure 4. Set of J-V curves for simulation and experimental work of tandem devices, and the single junction material as top subcells and bottom subcells [4]. .....	3
Figure 5. (a) two-terminals (2T) tandem model, (b) four-terminals (4T) tandem model [1]. .....	4
Figure 6. The best research efficiency trend, which is described with developing device lists [10]. .....	6
Figure 7. The highest efficiency chart of solar cells for photovoltaic (PV) technologies is plotted from 1976 to the present and the associated timeline of each solar cell [14]. .....	7
Figure 8. Perovskite compounds with (a) cubic, (b) tetragonal, and (c) orthorhombic structure [14]. .....	8
Figure 9. Effective absorption coefficient of a $CH_3NH_3PbI_3$ ( $MAPbI_3$ ) absorber thin film compared with other typical photovoltaic materials [15] (left) and band gap energy (right) of several perovskite materials [1]. .....	8
Figure 10. Schematic representation of PSCs structure: (a) n-i-p mesoscopic, (b) n-i-p planar, (c) p-i-n planar, and (d) p-i-n mesoscopic. ETL, electron transport layer; HTL, hole transport layer. ....	10
Figure 11. Architecture of CIGS solar cells.....	11
Figure 12. A schematic of an inline co-evaporation CIGS system.....	11
Figure 13. The architecture of tandem solar cells.....	12
Figure 14. The architecture of (a) two-terminal (2T) and (b) four-terminal (4T) tandem solar cells.....	13
Figure 15. Top and bottom cell bandgap energy spectrum diagram [34]. .....	14

Figure 16. Harvest the light spectrum of several absorber materials [1].	14
Figure 17. Working principles for metals, semiconductors, and insulators, respectively.	19
Figure 18. Schematic diagrams for circuit of a p-n junction.	20
Figure 19. Energy band (E) diagram of a P-N junction (a) before and (b) after merging the N-type and P-type regions.	21
Figure 20. Schematic of the depletion zone.	22
Figure 21. The electric field at the P-N junction drives the collection of photogenerated electrons and holes into N-type and P-type semiconductor regions, respectively.	23
Figure 22. The I-V curve and PV curve of an ideal cell presentation of $P_m$ at a bias of $V_{max}$ . The FF value equals 1 when the I-V curve is in the area of the outer rectangle.	25
Figure 23. Schematic circuit of solar cell.	26
Figure 24. The J-V curve of varying directions and rates of scanning from planar PSCs [62].	27
Figure 25. Blade coating method.	29
Figure 26. Slot-die coating method.	29
Figure 27. Spray coating method.	29
Figure 28. Spin-coating method.	30
Figure 29. Thickness of spin-coated thin films for different spin speed with spin time fixed at 30 s [72].	31
Figure 30. Illustration of a thermal evaporation system.	31
Figure 31. A diagram depicting the relationship between the intensity of film and the thickness of film.	34
Figure 32. An atomic force microscope (AFM) on the right with controlling computer on the left.	35
Figure 33. Schematic illustration of in situ atomic force microscopy (AFM).	35
Figure 34. An example of an FTO surface with a contact angle.	36
Figure 35. (a) a low contact angle ( $\theta < 30^\circ$ ) with good wettability, known as hydrophilic; (b) a higher contact angle, known as hydrophobic ( $\theta \geq 90^\circ$ ); and (C) a high contact angle with poor wettability ( $\theta > 120^\circ$ ), known as super-hydrophobic.	36
Figure 36. External quantum efficiency (EQE) of solar cell [73].	37

Figure 37. Schematic drawing of the typical Scanning Electron Microscope (SEM) column.....	38
Figure 38. Cleaning FTO surface method.....	39
Figure 39. Etching FTO surface method.....	40
Figure 40. The UV Ozone cleaner (left) and the inside of the UV Ozone cleaner (right). .....	40
Figure 41. (a) Chemical reaction, (b) Principle of UV ozone treatment.....	41
Figure 42. Fabrication of inverted perovskite device processes; (a) Cp-TiO <sub>2</sub> film, (b) Mp-TiO <sub>2</sub> film, (c) PbI <sub>2</sub> film, (d) MAI film, and (e) spiro-OMeTAD film. ....	44
Figure 43. Surface (above) and cross-section (below) image of Ti-Nanoxide T600/SC and Ti-Nanoxide T300/SC under spin speed 5000 rpm for 30s. ....	45
Figure 44. J-V characteristics of normal perovskite device with Ti-Nanoxide T600/SC (red line) and Ti-Nanoxide T300/SC (blue line). ....	45
Figure 45. Cross-section images of different precursor solutions, Mp-TiO <sub>2</sub> : Ethanol, (a) 1: 4 (M4), (b) 1: 5 (M5), and (c) 1: 7 (M7) v/v. ....	46
Figure 46. J-V curve of different precursor solutions, Mp-TiO <sub>2</sub> : Ethanol, (a) 1: 4 (M4), (b) 1: 5 (M5), and (c) 1: 7 (M7) v/v.....	46
Figure 47. J-V curve of various spin speeds at (a) 5000, (b) 4000, (c) 3000 rpm for 30 s with M4, M5 and M7, respectively. ....	47
Figure 48. The J-V characteristics under illumination of the perovskite solar cells are indicated in the legend. ....	49
Figure 49. Cross-section SEM (scale bar = 100 nm) images of perovskite film (P); for (a) without anti-solvent, (b) with addition of CB and (c) with addition of TO, as the anti-solvents. ....	51
Figure 50. Top-view SEM images of perovskite film with the application of CB anti-solvent at (a) 5 s, (b) 10 s and (c) 15 s; TO anti-solvent at (d) 5 s, (e) 10 s and (f) 15 s after spinning the 2 <sup>nd</sup> layer of MAI solution. ....	52
Figure 51. Optical absorption of perovskite absorber films vs. wavelength for various volume of (a) CB and (b) TO.....	53
Figure 52. Box chart plots of PCE of PSCs vs. volume of CB and TO anti-solvents for small active area of 0.06 cm <sup>2</sup> , which forward and reverse direction of J-V measurement refer to f and r, respectively. ....	54
Figure 53. Surface SEM images of 1 M NiO <sub>x</sub> -covered FTO glass at spin speeds of (a) 5000, (b) 6000, (c) 7000, and (d) 8000 rpm.....	56

Figure 54. Optical transmission of 1 M NiO <sub>x</sub> covered FTO glass at spin speeds of 5000 (blue line), 6000 (red line), 7000 (violet line) and 8000 (orange line). .....	56
Figure 55. J-V characteristics of the inverted perovskite device with a concentration of 0.5 M (left) and 1 M NiO <sub>x</sub> (right) by using different spin speed between 5000, 6000, 7000, and 8000 rpm for 30 s, respectively.....	57
Figure 56. Fabrication of inverted perovskite device processes; (a) PEDOT:PSS film, (b) PbI <sub>2</sub> film, (c) MAI film, (d) PC <sub>61</sub> BM film, and (e) BCP film. ....	59
Figure 57. The J-V curve of all types of PEDOT:PSS such as Al 4083, PH 1000, and HTL solar 3 with different spin speeds between 5000 and 6000 rpm for 30 s. ....	60
Figure 58. J-V curve of PTAA at spin speed 2000 (blue) and 3000 (red line) rpm for 30 s. ....	62
Figure 59. Current-voltage characteristics measured under standard 1 sun condition (AM 1.5 G, 100 mW/cm <sup>2</sup> ) of 1 M NiO <sub>x</sub> covered FTO glass at spin speed 5000 rpm (greenline), PEDOT:PSS (HTL solar 3) covered FTO glass at spin speed 6000 rpm (red line), and PTAA covered FTO glass at spin speed 3000 rpm (blue line). The inset shows the solar parameters of different HTMs.....	63
Figure 60. Device fabricated using different contact materials: (a) Al, (b) Au, and (c) Ag.....	64
Figure 61. J-V characteristics of the inverted perovskite devices with different metal contacts such as Au (blue line), Ag (red line), and Al (green line). ....	64
Figure 62. Box chart plots of using PTAA as hole transport material on an inverted structure for 0.06 cm <sup>2</sup> active cell area. ....	65
Figure 63. Defection on the PTAA surface from the washing process. ....	66
Figure 64. Fabrication procedures of inverted perovskite device. ....	67
Figure 65. Comparisons of optical transmission spectra of pristine and post-treated PTAA layers (left) and MAPbI <sub>3</sub> - perovskite on pristine and post-treated PTAA layers(right).....	68
Figure 66. Contact angles of the PTAA films; (a) pristine, and post-treated PTAA by washing with 200 µl of DMF and followed by (b) 50 µl TO, (c) 75 µl TO, (d) 50 µl CB and (e) 75 µl CB. ....	68
Figure 67. AFM surface morphologies of the PTAA films; (a) pristine, and post-treated PTAA by washing with 200 µl of DMF and followed by (b) 50 µl TO, (c) 75 µl TO, (d) 50 µl CB and (e) 75 µl CB. ....	68



Figure 68. (a) J-V curves of PSCs for both pristine and post-treated PTAA. Solar cell parameters of PSCs; (b) $V_{OC}$ , (c) $J_{SC}$ , (d) Fill Factor and (e) PCE of PSCs comparing between pristine PTAA and post-treated PTAA.....	69
Figure 69. Box chart plots of using F4-TCNQ doped PTAA as hole transport material on inverted structure (above) and the J-V characteristics of F4-TCNQ doped PTAA on inverted PSCs for 0.2 cm <sup>2</sup> active cell area (below). .....	71
Figure 70. Device schematics of the fabricated (a) two-terminal (2T), (b) four-terminal (4T) perovskite/CIGS tandem solar cells. ....	74
Figure 71. J-V characteristics under illumination of the normal and the inverted perovskite solar cell as indicated in the legend.....	74
Figure 72. Cross-section images of (a) normal PSCs, (b) inverted PSCs, and (c) two-terminals (2T) inverted perovskite-CIGS tandem solar cells (AZO is ZnO(Al)/i-ZnO). .....	75
Figure 73. The J-V curve of two-terminal (2T) tandem device. The inset shows the photovoltaic parameters of 2T tandem cells. ....	76
Figure 74. J-V curves of the best-performing tandem device together with CIGS stand-alone (blue line), normal perovskite stand-alone (red line), inverted perovskite stand-alone (light blue line), 4T CIGS filtered with normal perovskite (brown line), and 4T CIGS filtered with inverted perovskite (violet line). ....	76
Figure 75. EQE spectra of the perovskite, CIGS subcells and the four-terminal (4T) perovskite-CIGS tandem device. ....	77

# CHAPTER I

## INTRODUCTION

Recently, 80% of the energy consumption in the world is from fossil fuels, which generates a ton of CO<sub>2</sub> and leads to an average temperature increase on the earth, or global warming. To decrease CO<sub>2</sub> emissions and prevent global warming, solar energy is the new generation of green energy of all other alternatives. Accordingly, solar photovoltaic (PV), which is the conversion of sunlight into electricity using semiconducting materials, is attracting huge interest and being studied to improve solar PV. Figure 1 demonstrates the evolution of PV published since 1980, and the number of related scientific articles is shown in the vertical axis. Many articles are still continuously published to develop solar technologies.

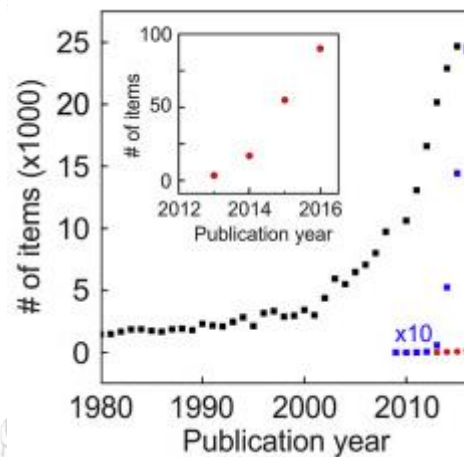


Figure 1. Publication year for PV devices [1].

In the 1990s, organic halide solar cells based on metal-halide (ABX<sub>3</sub>) perovskites were introduced as a new application in transistor technology and light-emitting diodes. Perovskite has a crystal structure of ABX<sub>3</sub> as shown in figure 2, where A is an organic cation (ethylammonium, methylammonium, or CH<sub>3</sub>NH<sub>3</sub>, or NH<sub>2</sub>CH<sub>3</sub>NH<sub>2</sub>), B is a divalent metal cation (Pb<sup>2+</sup>, Sn<sup>2+</sup>, Sr<sup>2+</sup> and other rare metals), and X is a monovalent halide anion (Cl<sup>-</sup>, I<sup>-</sup>, and Br<sup>-</sup>). Perovskite has been known as an absorber layer for solar cells and it is called perovskite solar cells (PSCs), which have exhibited great performance in the past decade. The power conversion efficiency (PCE) of PSCs has remarkably jumped from a modest 2.2% in 2006 to over 20.1% in 2014 [2]. Recently, scientists have been developing perovskite materials that are environmentally friendly and stable over time.

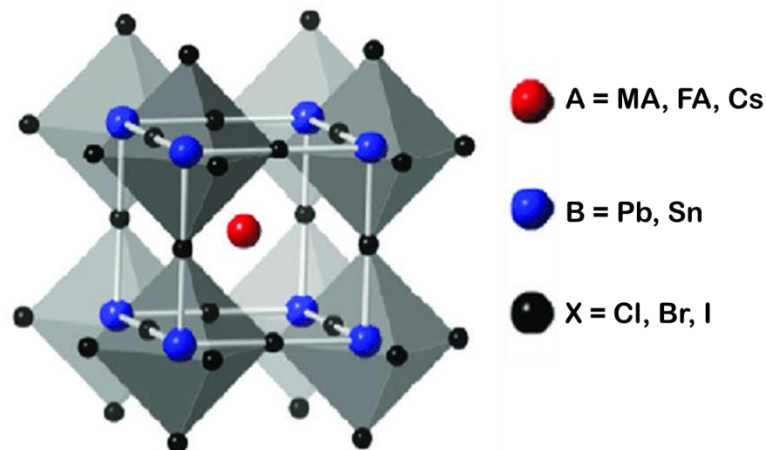


Figure 2. Crystal structure of perovskite  $ABX_3$  [3].

The absorbing material depends on the bandgap energy ( $E_g$ ). Specifically, the range of suitable  $E_g$  for using solar cells is 1.1 eV to 1.74 eV.  $CH_3NH_3PbI_3$  (MAPbI<sub>3</sub>) perovskite films can absorb photons with wavelengths up to 600 nm ( $E_g$  of MAPbI<sub>3</sub> is about 1.6 eV), which is advantageous for solar cell applications.

Tandem solar cells are made up of different subcells, each of which can absorb a different wavelength of light. Tandem solar cells are commonly comprised of two different devices; one is a top solar cell with a relatively large band gap absorber and the other is a bottom solar cell with a relatively small band gap. In this study, the top device for tandem solar cells is PSCs and the bottom cell is copper indium gallium selenide ( $CuIn_{1-x}Ga_xSe_2$  or CIGS) as illustrated in figure 3 (a).

Moreover, a double-junction tandem solar cell architecture allows the top subcells to absorb photons at higher energies (shorter wavelengths) while lower energies (longer wavelengths) enter deeper into the solar device and are harvested by the bottom subcells. On the contrary, a single-junction device can only harvest light energy that is lower than  $E_g$ , as seen in figure 3 (b). As a result, the PCE of tandem solar cells is superior to that of a single-junction device, as presented in figure 4.

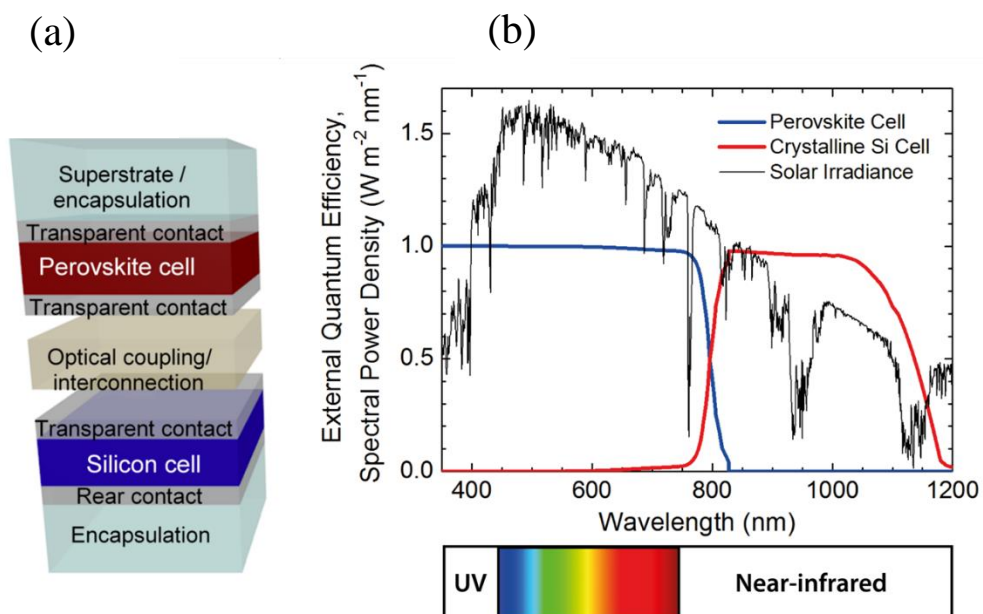


Figure 3.(a) Schematic illustration of a perovskite/silicon tandem artifact (b) Photons emitted through the perovskite cell first can be mostly absorbed in the visible region of the solar spectrum. The near-infrared light (NIR) part is harvested via the silicon solar cells [1].

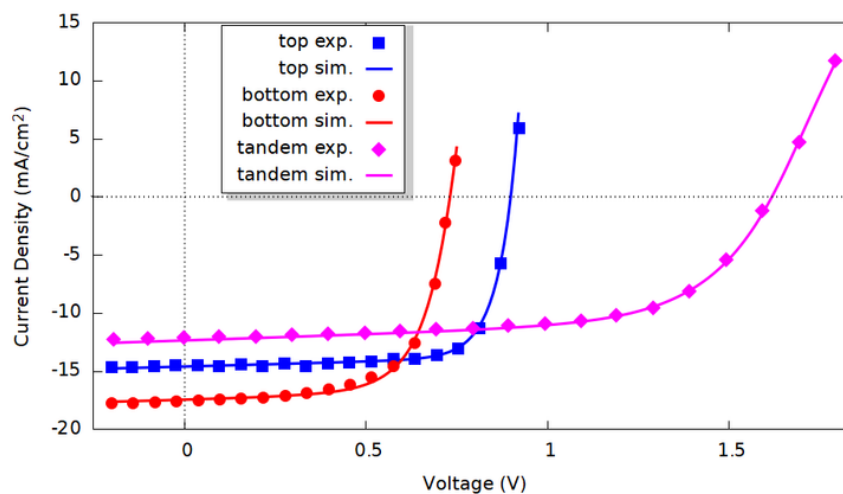


Figure 4. Set of J-V curves for simulation and experimental work of tandem devices, and the single junction material as top subcells and bottom subcells [4].

As said earlier, tandem solar cells configurations consist of two or more cells and are expected to absorb all of the solar light range from the subsequent cells. Tandem solar cells can be classified into two types: two-terminal (2T) and four-terminal (4T) tandem solar cells. Figure 5(a) shows a two-terminal (2T) tandem solar device, each subcell requires a combination layer or a suitable band gap energy to achieve reasonable line alignment for appropriate charge transfer. Nevertheless, this structure must have the same current in both top and bottom subcells due to the fact that subcells produce lower photocurrents, which is limited. Whereas a four-terminal (4T) tandem solar cell (figure 5(b)) is introduced to achieve a higher photocurrent with an external connection, which different junctions inside a 4T tandem cell device are used to increase 2T tandem solar cells.

Typically, two-terminal tandem solar cells are more of interest due to improved optical loss, parasitic absorption, as well as a relatively lower cost. But the transparent conductive materials are required for two-terminal tandem solar cells. The pros and cons of two-terminal (2T) tandem cells and four-terminal (4T) tandem cells are shown in Table 1.

The fabricated tandem device architectures were studied with several structures in 2009 [5]. For instance, stacking perovskite solar cells on top of silicon ones was selected, and it was found that this structure could increase the absorption of sunlight. A III-V semiconductor or organic solar cell as a bottom cell and a perovskite solar cell as a top cell were studied, and the performance of tandem cells can also be improved. Therefore, a perovskite device can be integrated inside tandem cells and act as the front subcells while the bottom subcells are various, such as silicon, CIGS, or perovskite devices.

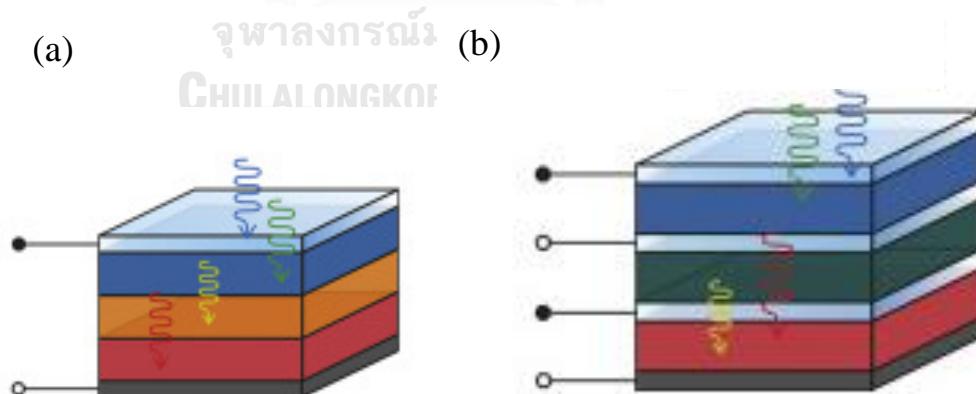


Figure 5. (a) two-terminals (2T) tandem model, (b) four-terminals (4T) tandem model [1].

Table 1. Disadvantages and advantages of 2T and 4T tandem solar cells[6, 7].

	Disadvantage	Advantage
2T tandem solar cells	<ul style="list-style-type: none"> <li>• Current loss from current matching of the two layers</li> <li>• The solvent penetration during the fabrication of the top subcell can affect chemical properties of bottom subcell</li> </ul>	<ul style="list-style-type: none"> <li>• Easier fabrication because of fewer contacts</li> </ul>
4T tandem solar cells	<ul style="list-style-type: none"> <li>• Optical loss due to reflection at the air gap between top and bottom cells</li> </ul>	<ul style="list-style-type: none"> <li>• Top and bottom subcells are fabricated separately</li> <li>• Subcells work independently and as a result, the sum efficiency is just the total of every subcell</li> </ul>

From all of the above, a tandem solar cell has shown great promise to be an excellent device in the near future because it can harvest sunlight at a broader wavelength and achieve higher PCE compared to a single-junction solar cell. In this study, the tandem solar cell with PSCs as the top cells and CIGS as the bottom cells was chosen. Both two-terminal and four-terminal tandem solar cells were studied in this research.

### 1.1 Objectives of the research

1. To design and fabricate perovskite solar cells (PSCs) as part of tandem structures with  $\text{CuIn}_{1-x}\text{Ga}_x\text{Se}_2$  (CIGS) or Silicon (Si)
2. To find appropriate transparent conducting materials to connect perovskite solar cells with CIGS or Si
3. To characterize physical properties of the perovskite tandem solar cells

### 1.2 Scope of the research

1. Tandem solar cells that utilize perovskite as a top cell
2. Transparent conducting materials that can connect perovskite solar cells with CIGS or Si
3. Factors that affect physical properties of tandem solar cells with perovskite as a top cell

## CHAPTER II

### LITERATURE REVIEWS

#### 2.1 ABX<sub>3</sub> perovskite materials group for Single-junction solar cells

Methyl-ammonium lead iodide (MAPbI<sub>3</sub>) is one of the advanced organic-inorganic hybrid perovskite materials used for perovskite solar cells (PSCs) that is considered a new low-cost photovoltaic (PV) technology when compared with silicon solar cells. In 1839, the crystal structure of perovskite was discovered and designated by Gustav Rose, who is a German mineralogist, and the Russian mineralogist, Lev Perovskite [8]. In general, the crystal structure ABX<sub>3</sub> is the formula of organic-inorganic hybrid halide-based perovskites, where A is an organic cation (e.g., CH<sub>3</sub>NH<sub>3</sub><sup>+</sup> or CH(NH<sub>2</sub>)<sub>2</sub><sup>+</sup>), B is a divalent metal cation (e.g., Pb<sup>2+</sup> or Sr<sup>2+</sup>), and X is a monovalent halide anion (I<sup>-</sup>, Br<sup>-</sup> or Cl<sup>-</sup>). Firstly, dye-sensitized solar cells (DSSCs) as organic-inorganic hybrid halide-based perovskites have obtained a power conversion efficiency (PCE) of 3.8% since their advent in 2009 [8].

In 2012, a PCE of 9% was received when using spiro-OMeTAD as the hole transporting layer (HTL) due to enhanced hole mobility on PSCs [9]. After that, PSCs that were widely studied achieved a PCE of 22.1% in 2016. The best PCE from each year is presented in figure 6. The trend in this graph shows that the PCE of PSCs has been developing.

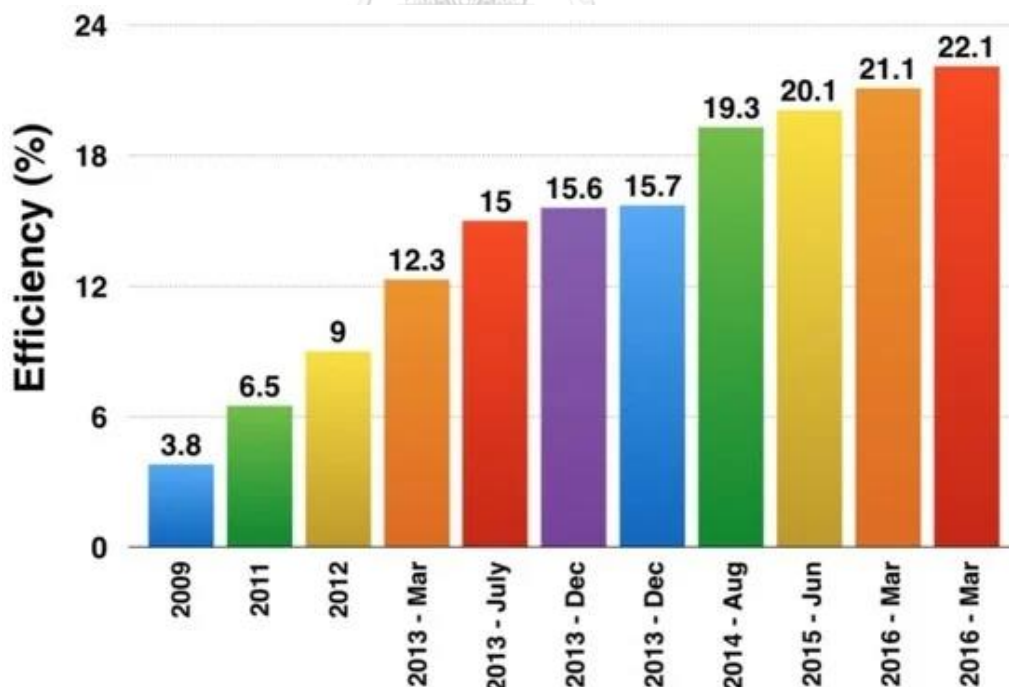


Figure 6. The best research efficiency trend, which is described with developing device lists [10].

Figure 7 shows the highest efficiency chart of solar cells for photovoltaic (PV) technologies from 1976 to present. In particular, the experimental efficiency of perovskite solar cells has been rapidly improved PCE more than other solar cells, from 3.8% to 25.5% [11, 12]. Thus, the PSC is one of the promising next generations of PV technologies.

When methyl-ammonium lead triiodide ( $\text{MAPbI}_3$ ) was investigated at room temperature, it formed a tetragonal structure (space group  $I4cm$ ) (figure 8(b)), and at 160 K, it formed an orthorhombic structure (space group  $Pnma$ ), as shown in figure 8(c), and figure 8(a) displays a cubic structure that occurred at 327 K [13]. The perovskite materials begin to absorb light at wavelength at 780 nm and their band gap can be estimated to be 1.6 eV, which is demonstrated in figure 9. It also has a high absorption coefficient, which can generate enough current when photon energy from sunlight is equal or lower than its  $E_g$ .

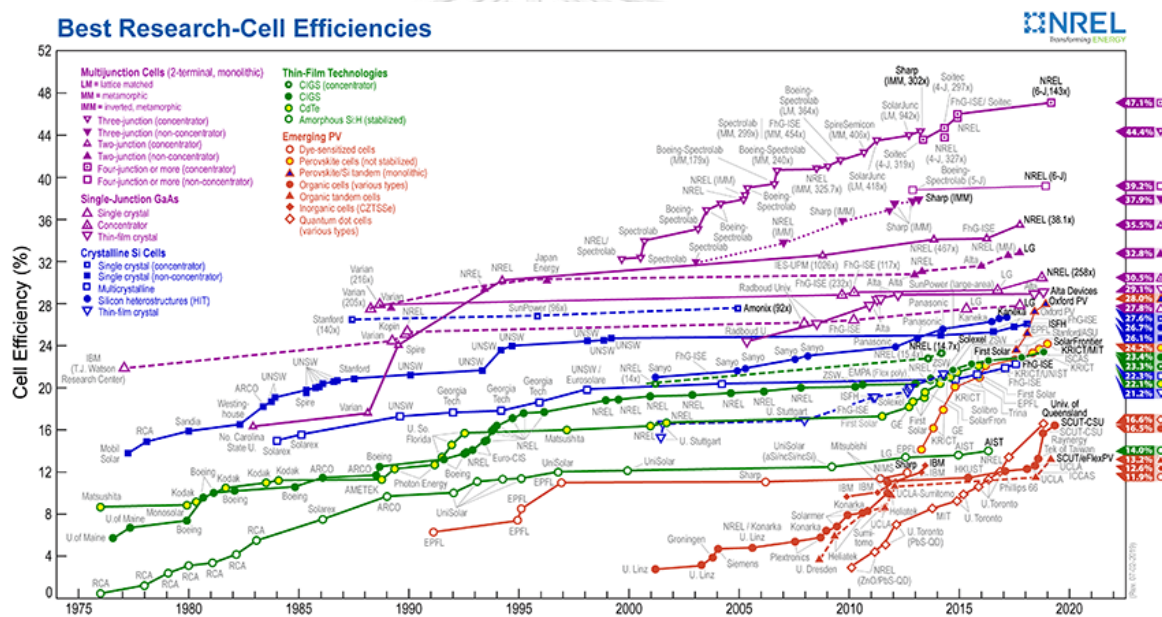


Figure 7. The highest efficiency chart of solar cells for photovoltaic (PV) technologies is plotted from 1976 to the present and the associated timeline of each solar cell [14].



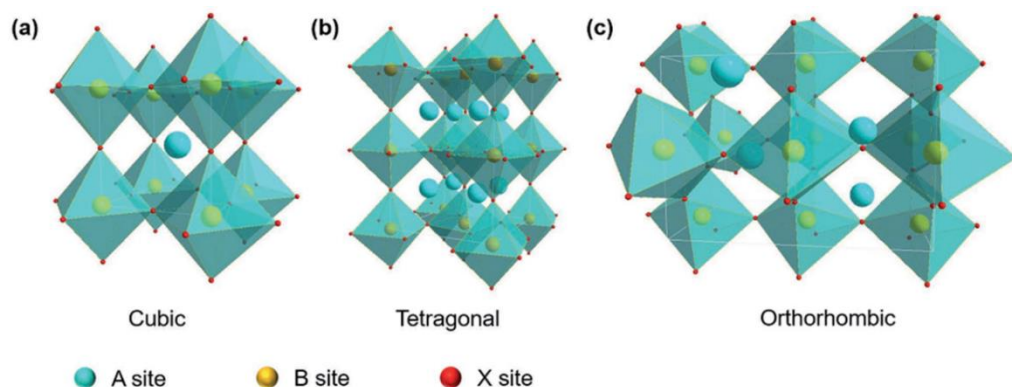


Figure 8. Perovskite compounds with (a) cubic, (b) tetragonal, and (c) orthorhombic structure [14].

Since a perovskite structure is  $ABX_3$ , many cations and anions can be used to form perovskite materials with different properties. For instance, the band gap can be tuned by changing halide ions (I or Br), organic cations (FA or MA), and divalent cations (Sn, Pb). Thus, the optical absorption edges of perovskites vary from 350 to 1,200 nm.

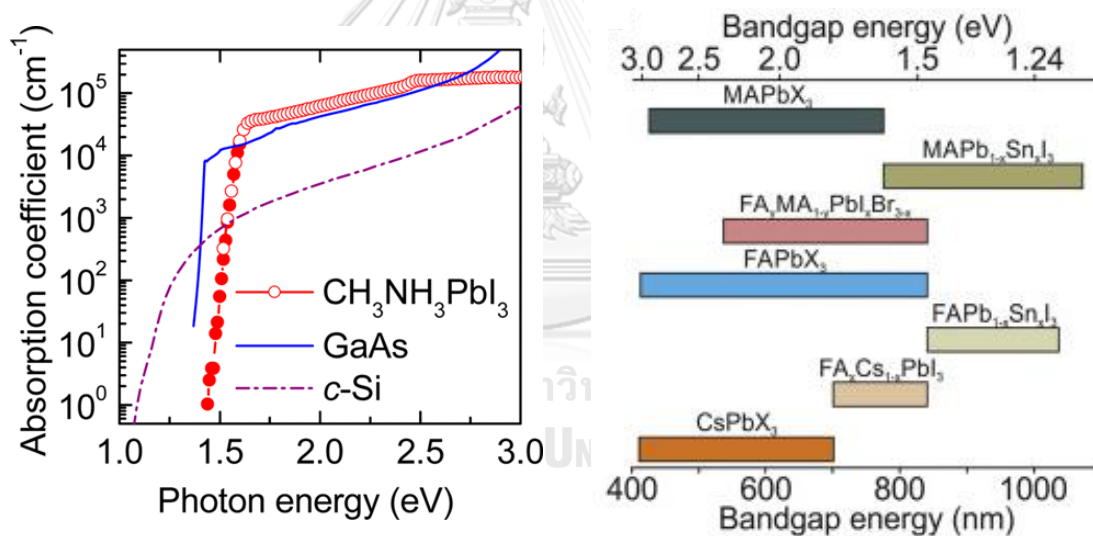


Figure 9. Effective absorption coefficient of a  $\text{CH}_3\text{NH}_3\text{PbI}_3$  ( $\text{MAPbI}_3$ ) absorber thin film compared with other typical photovoltaic materials [15] (left) and band gap energy (right) of several perovskite materials [1].

### 2.1.1 Halide anions for X-Site replacing

Seok et al. suggested changing from bromine (Br) to iodine (I) for  $\text{MAPbX}_3$  (or perovskite film) where MA is methyl-ammonium and  $\text{X}_3$  is triiodide that can be rewritten to  $\text{MAPbI}_3$ . At present, both  $\text{MAPbBr}_x\text{I}_{3-x}$  and  $\text{MAPbCl}_x\text{Br}_{3-x}$  perovskite films can cover all the visible regions of the spectrum that can be studied from many articles [13].

On the periodic table, I<sup>-</sup> is the biggest halide anion and is followed by Br<sup>-</sup> anion size, and the smallest one is Cl<sup>-</sup> (I<sup>-</sup> > Br<sup>-</sup> > Cl<sup>-</sup>). In addition, the absorption edge is shifted to the blue wavelength region, which changes E<sub>g</sub> from 1.6 eV of MAPbI<sub>3</sub> to 2.3 eV and 3.1 eV of MAPbBr<sub>3</sub> and MAPbCl<sub>3</sub> [16, 17], respectively.

### 2.1.2 Metal cation for B-Site replacement

The B site in ABX<sub>3</sub> of the perovskite structure replaced Pb<sup>2+</sup> [18] with Ge<sup>2+</sup> [19] or Sn<sup>2+</sup> [13] cation, which may have obtained an E<sub>g</sub> of 1.17 eV due to NIR absorption.

### 2.1.3 Organic or inorganic cation for A-Site replacement

The A-site cation must be the largest when compared with the B-site cation and X-site anion. At the A-site, the organic cation of the perovskite structure remained. The MAPbI<sub>3</sub> perovskite contains MA, Pb, and I. Furthermore, the MA is substituted with formamidinium (CH(NH<sub>2</sub>)<sub>2</sub><sup>+</sup>, FA) or Cs ions, both of which can be replaced by the organic cation. After the FA is replaced with the MA organic cation, bandgap energy (E<sub>g</sub>) can change from 1.6 eV to 1.45 eV [20, 21], which rewrote the formula as FAPbI<sub>3</sub>. Similarly, when a Cs cation is added, the perovskite structure changes to CsPbI<sub>3</sub> or CsSnI<sub>3</sub>, and its E<sub>g</sub> appears at a shorter wavelength [22]. As a result, these implements corresponded to changing E<sub>g</sub>.

Furthermore, metal mixtures have been studied, including FA<sub>y</sub>MA<sub>1-y</sub>PbI<sub>x</sub>Br<sub>3-x</sub> [23], FA<sub>y</sub>Cs<sub>1-y</sub>PbI<sub>x</sub>Br<sub>3-x</sub> [24], and FA<sub>y</sub>Cs<sub>1-y</sub>PbSnI<sub>3</sub> [17]. Also, triple Cs/MA/FA for perovskite is fabricated to improve stability and resist humidity [25].

## 2.2 Conventional PSCs and Inverted PSCs

The PSCs are categorized into 4 types as illustrated in figure 10;

- 1) n-i-p mesoscopic structure is a conventional PSCs (figure 10a),
- 2) n-i-p planar structure is a conventional PSCs (figure 10b),
- 3) p-i-n planar structure is an inverted PSCs (figure 10c),
- 4) p-i-n mesoscopic structure is an inverted PSCs (figure 10d),

where n is an N-type semiconductor (electron transport materials), i is an intrinsic semiconductor (perovskites), and p is a P-type semiconductor (hole transport materials). A mesoporous scaffold is employed for a mesoscopic structure. For example, a mesoporous titanium dioxide (Mp-TiO<sub>2</sub>) layer is used for an n-i-p mesoscopic structure which is deposited onto compact titanium dioxide (Cp-TiO<sub>2</sub>). Thus, perovskite film is sandwiched between ETM and HTM. Silvia et al. is one of several research groups reached PCE of >10% from PSCs in n-i-p planar device structure (see figure 18(b)) when device is fabricated with fullerene as electron transporting layer (ETL) [26]. Furthermore, PCE of 13.6% is achieved when fabricated with n-i-p mesoscopic [27] because it has low carrier recombination compared to Mp-TiO<sub>2</sub> and Cp-TiO<sub>2</sub> based perovskite devices.

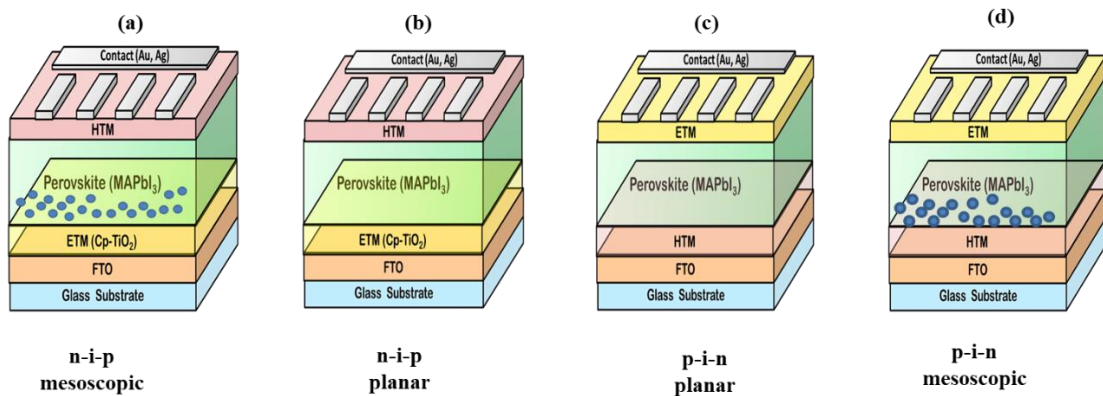


Figure 10. Schematic representation of PSCs structure: (a) *n-i-p* mesoscopic, (b) *n-i-p* planar, (c) *p-i-n* planar, and (d) *p-i-n* mesoscopic. ETL, electron transport layer; HTL, hole transport layer.

### 2.3 CuInGaSe<sub>2</sub>(CIGS) solar cells

Cu(In, Ga)Se<sub>2</sub> (or CIGS) solar cell is the most efficient thin film solar cell technology available today. Many researchers developed this thin film solar cell with a long history. In 1953, CuInSe<sub>2</sub> was developed for the first time [28]. The CIGS solar cells were widely produced around the world such as in the US, Europe, Japan, etc. The alloyed CIGS consisted of CuInSe<sub>2</sub> and CuGaSe<sub>2</sub> materials, which were proposed as the I-III-VI<sub>2</sub> semiconducting materials. [29]. The CIGS acts as the absorber layer of the thin film solar cells to generate charges from photons. The CIGS film is fabricated with elements of Cu, In, Ga, and Se via a time-dependent profile. The ratio of  $[\text{Cu}]/([\text{In}]+[\text{Ga}])$  is used to calculate the phase chemistry during deposition. Furthermore, the CIGS band gap profile is determined by the moderate Ga content on Cu(In, Ga)Se<sub>2</sub> with  $[\text{Ga}]/([\text{Ga}] + [\text{In}])$  ratio. The suitable band gap energy ( $E_g$ ) of a Cu(In, Ga)Se<sub>2</sub> solar cell ranged from 1.15 eV to 1.4 eV [30]. At the moment, the Cu(In, Ga)Se<sub>2</sub> solar cells have a power conversion efficiency (PCE) of 23.35%. [31]. Figure 11 depicts a Cu(In, Ga)Se<sub>2</sub> solar cell constructed layer by layer of 1  $\mu\text{m}$  molybdenum (Mo) layer, 2  $\mu\text{m}$  CIGS layer, 50 nm Cadmium sunfile (CdS) layer, 200 nm Zinc Oxide (ZnO) layer, and 1  $\mu\text{m}$  aluminum (Al). Several methods were used to grow these layers on the Cu(In, Ga)Se<sub>2</sub> solar cells. The production method for Mo and ZnO layers was the sputtering technique, whereas CIGS and CdS thin films were deposited with the co-evaporation technique of the elements (see figure 12) and chemical bath deposition (CBD) process from a mixing solution of cadmium (Cd) and thiourea, respectively. Furthermore, all these layers generate charges which flow through each layer from the back contact (Mo layer) to the front contact (Al metal electrode). The Al electrode is fabricated with an evaporation technique.

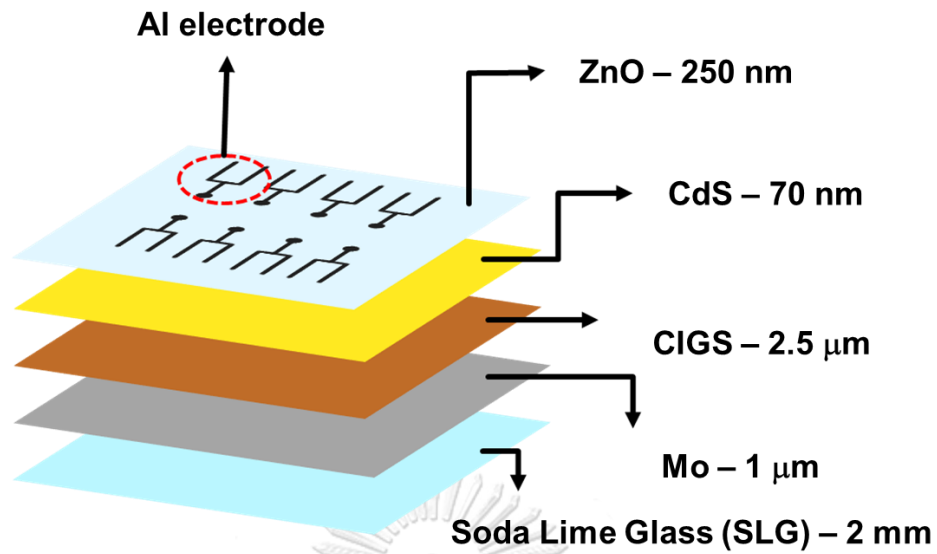


Figure 11. Architecture of CIGS solar cells.

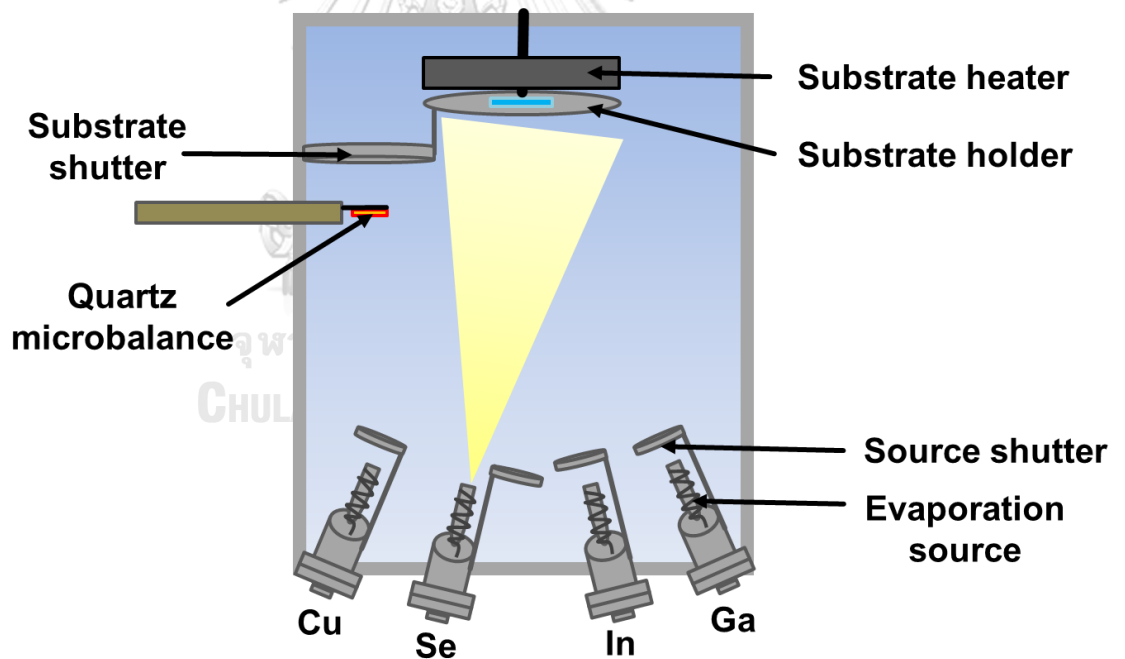


Figure 12. A schematic of an inline co-evaporation CIGS system.

## 2.4 Tandem cell

### 2.4.1 Perovskite-Based Double-Junction Solar Cells

To converse efficiency from solar devices, the simplest solar cells usually use one active junction, which is called a single junction, but it is limited that the best case presents a power conversion efficiency of no more than 30% [32]. To improve the experimental efficiency of solar cells, the active part of the solar spectrum is expanded to increase the absorption of incoming sunlight that has different wavelengths, i.e., generally the near infrared (NIR) and the near ultraviolet-visible (UV-visible). Thus, using several subcells on a device for absorbing different frequencies of sunlight is referred to as multi-junction solar cells (MJSC) or tandem solar cells (figure 13) to get more efficient at converting sunlight into electricity than single-junction cells. In terms of photovoltaic effect, the strategies of tandem solar cells mention mechanisms between chemical and mechanical procedures with three main steps.

First step, absorbing sunlight on tandem solar cells can improve electrons generation in the semiconducting device to knock loose.

Second step, creating an electrical current occurred with electron flowing inside circuit of semiconductor device.

Third step, wires are transferred and captured with current.

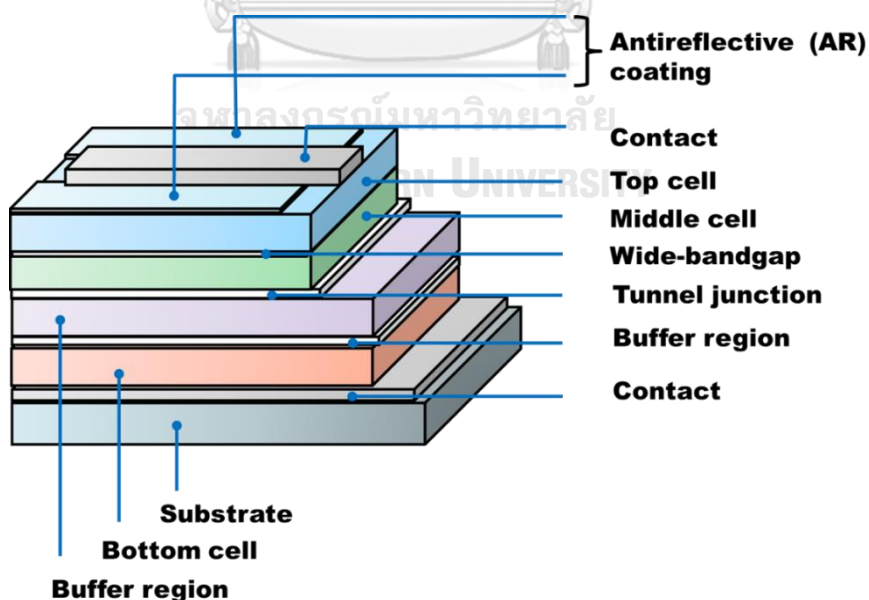


Figure 13. The architecture of tandem solar cells.

Nowadays, the best performance efficiency for very small devices is promoted by PCE of up to 45% [33]. Some tandem devices have two terminals (2T) and four terminals (4T), which are contacts for individual subcells to lead electrical connections to individual component subcells as shown in figure 14. 2T tandem solar cells have two contacts, while 4T tandem solar cells have four contacts. Recently, the experimental demonstration of tandem devices used perovskite solar cells as top subcells, which were combined with bottom subcells such as silicon (Si), copper indium gallium diselenide (CIGS), and other perovskite, which have narrower bandgap energy ( $E_g$ ) (see figure 15) to harvest light spectrum at higher wavelengths than the  $E_g$  of top subcells, as shown in figure 16. Moreover, many of these articles are widely studied by researchers who suggest and discuss procedures that affect the power conversion efficiency of devices. In this study, we focus on how to design and fabricate perovskite cells for a type 2T tandem solar cell to achieve PCE that displays the high-performance device. The J-V curve for measuring PCE by using commercial solar simulators is very complicated when there is a spectrum mismatch. Thus, the architecture and fabrication methodology of the solar module are used as a strategy to solve this problem.

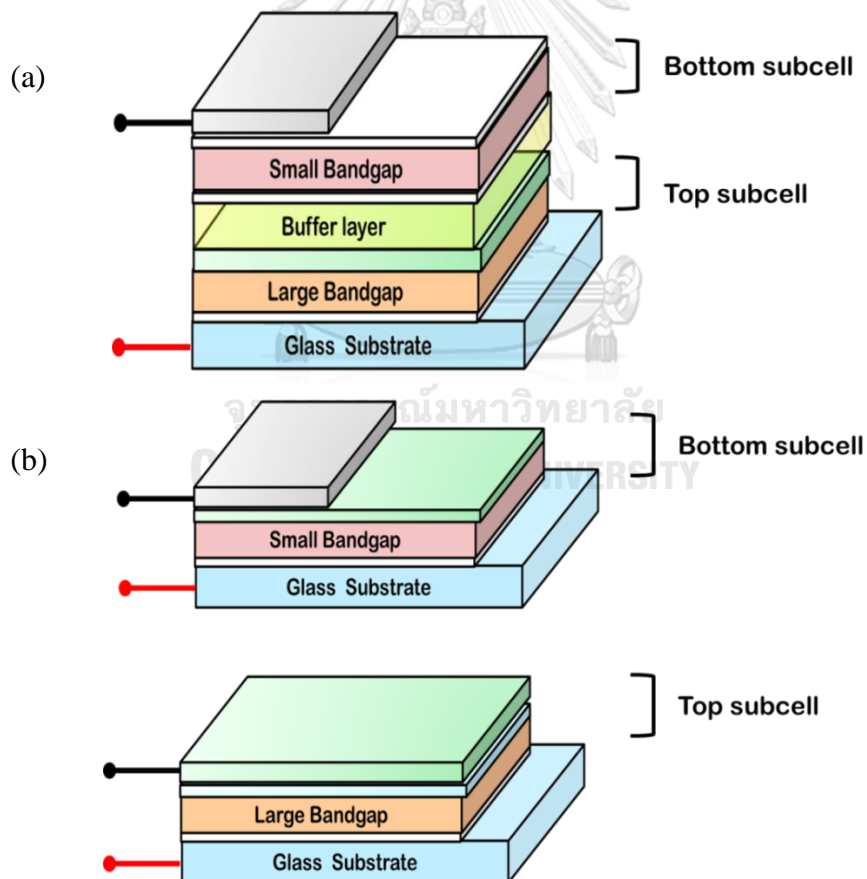


Figure 14. The architecture of (a) two-terminal (2T) and (b) four-terminal (4T) tandem solar cells.

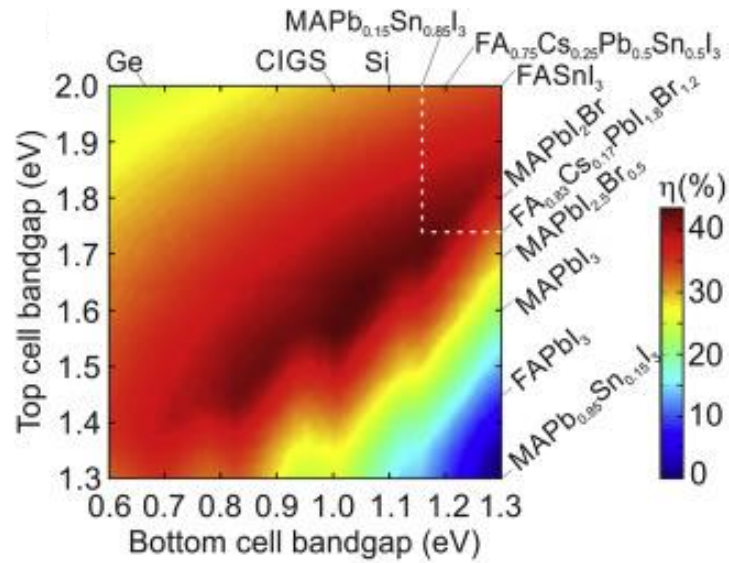


Figure 15. Top and bottom cell bandgap energy spectrum diagram [34].

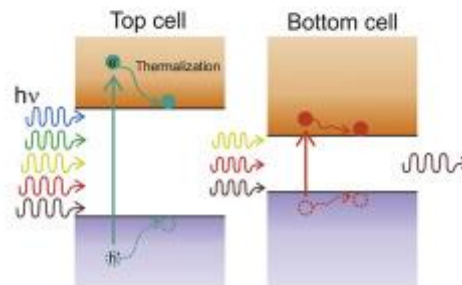
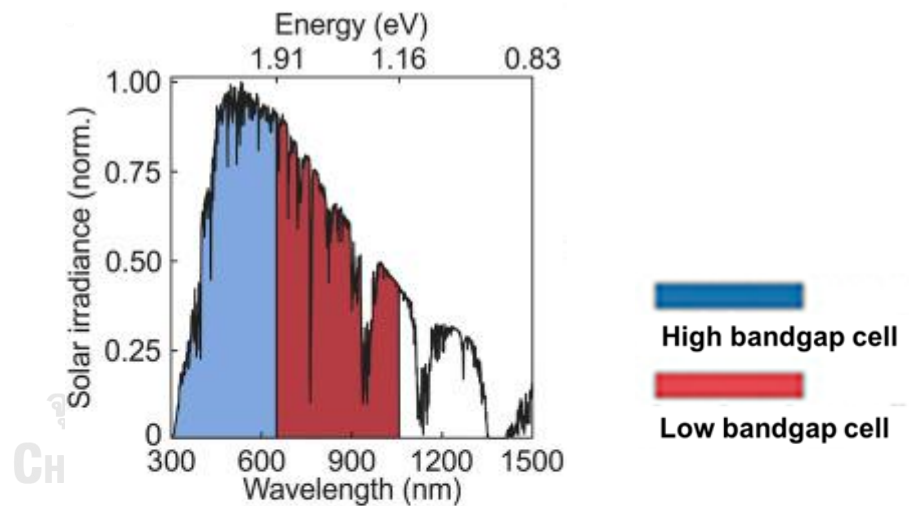


Figure 16. Harvest the light spectrum of several absorber materials [1].

### 2.4.2 Perovskite/Chalcogenide Cells

The combination of a perovskite device on a CIGS device is published as the best experimental PCE of 10.9% [35] with the 2T tandem configuration, which can improve material usage and parasitic losses. This action is called hysteresis [36]. However, a single circuit of a 2T tandem device needed to be current matched to the flowing current of each subcell [37]. Also, the bottom subcells needed a stable support combination with the top subcells by adjusting the deposition process. The CIGS device is used as a bottom subcell that replaces silicon solar cells for PV technology. Recently, this evolution of PV technology has reached a PCE of over 23.35% in CIGS devices [38]. The bandgap energy ( $E_g$ ) of CIGS and perovskite materials is between 1.1 and 1.24 eV and 1.17 and 3.1 eV, respectively [34, 39]. Those  $E_g$  are considered and tuned to combine for tandem devices that present performance efficiency with an optimized  $E_g$ . All processes for CIGS-perovskite tandem solar cells need to be fabricated below 200°C to prevent degradation of the p-n junction in CIGS.

In 2015, Todorov et al. suggested a two-terminal CIGS-based tandem device, which is the first report [40]. Researchers studied the use of 1.04 eV  $E_g$  of CIGS material that acted as an absorber layer in bottom subcells that have an architecture of CdS/CIGS/Mo/Si<sub>3</sub>N<sub>4</sub>/glass. Normally, the intrinsic ZnO layer is added in CIGS solar cells but reacts with perovskite. A fluoride-doped tin oxide (FTO) and an iodide-doped tin oxide (ITO) are coated on the glass by the sputtering method, in which the FTO or ITO film on the glass substrate is used as a transparent recombination layer or anode contact (rare contact). In fabrication, perovskite subcells are deposited on CIGS subcells at under 120°C. The MAPbI<sub>x</sub>Br<sub>3-x</sub> film acted as a perovskite absorber layer with  $E_g$  of 1.72 eV to fabricate a perovskite/CIGS tandem device, which got a PCE of 10.98% [40].

For the objective of third-generation PV technology, using all-perovskite tandem solar cells has been introduced to increase current generation for higher PCE, which is approximately the PCE of Si solar cells. The PSCs typically have high voltage and can collect sunlight power, which is in the range of 400 to 820 nm when fabricated by the Pb-based perovskites. These are reported in several articles [35, 36]. Moreover, a solvent engineering or anti-solvent method was studied in 2016 [41-43] to improve the uniformity of perovskite. Thus, the 4T tandem cell features a PCE of 21.0% with the FA<sub>0.3</sub>MA<sub>0.7</sub>PbI<sub>3</sub>/FA<sub>0.6</sub>MA<sub>0.4</sub>Pb<sub>0.4</sub>Sn<sub>0.6</sub>I<sub>3</sub> device, which is reported by Zhao et al. [44]. While 2T tandem cells is fabricated with perovskite-based tandem devices by reviewing of Rajagopa et al. [45] they display a PCE of 18.5% by using a combination of compositional, interfacial, optical, and semiconductor engineering such that the PCE of the 2T tandem device demonstrated photovoltage is less than the theoretical limit of 20% [46].

Many researchers who are focused on new alternatives to receiving high-performance solar devices in the near future expect the development of all-perovskite tandem cells. In addition, the motivation for this improvement is the enhanced



potential of the working device, which is the stability of the perovskite device with suitable band alignment of electron transport layer (ETL) and hole transport layer (HTL). This method can promote PCE of 30% with the perovskite-on-perovskite tandem structure represented by by Forgács et al. [45]. All tandem devices have the advantage that they obtain high conductivity or low resistance by considering suitable band alignment and also minimize current losses to enhance PCE by fabrication of suitable optical layers at the FTO or ITO substrate, anode contact, cathode contact, ETLs, and HTLs. The motivation of a monolithic tandem device needs to connect between bottom and top subcells with the same current density to transfer current between both two subcells in this series. It is called current-matching for 2T tandem devices. In addition, the aim of a buffer or an intermediate layer is used to separate electrons and holes.

In this work, with the glass/FTO/TiO<sub>2</sub>/MAPbI<sub>3</sub>/Spiro-OMeTAD/Au and glass/FTO/PTAA/MAPbI<sub>3</sub>/PC<sub>61</sub>BM/BCP/Ag architecture, which is a single junction with n-i-p and p-i-n structure, we obtained a maximum PCE of 16% and 15.4%, respectively. Hence, individual layers must be of appropriate thickness and photocurrent matching in order to harvest photons from sunlight, where the perovskite layer or absorber layer is limited to being thinner than 300 nm in order to generate charge at a wavelength ranging from 300 to 800 nm. In this device formation, we picked FTO as the anode (front) contact with a thickness of 300 nm, and the thickness of Au is 120 nm as a cathode or a metal back contact. Also, both Mp-TiO<sub>2</sub> and Cp-TiO<sub>2</sub> are used as ETLs with a thickness of 50 and 200 nm, respectively. The Spiro-OMeTAD layer acted as an HTL since it was deposited on top of the MAPbI<sub>3</sub> layer with a thickness of 150 nm. For tandem solar cells, the perovskite model needed to change structure from n-i-p (conventional structure) to p-i-n structure (inverted structure) to support current matching with other subcells. Moreover, we selected a 2T-based tandem model to reduce the refractive indices of the different subcells, which is an issue that occurred in a 4T tandem model. However, using the ABX<sub>3</sub> structure for perovskite devices, the optical transparent model must be the perovskite device employed as a top subcell for generally 2T tandem solar cells [47, 48].

Also, the inverted tandem structure can increase the transport of charge carriers. In particular, the front contact of a top subcells must be transparent to lead light to the next subcells that transparent contact aims to reduce optical losses. Even, the best fabrication of perovskite-based tandem solar cells (see Tables 2) used ITO as transparent contact. Many articles suggested several contacts to replace ITO, such as FTO, IZO, SiNWs, AgNWs, Ag or Au [46, 49-52]. In contrast, the differential thickness of each material affects the PCE of the device as well. However, the buffer layer is added on the HTL to prevent reaction between transparent contacts and the HTL when a buffer layer such as MoO<sub>x</sub>, ZnO, or BCP [8, 53, 54] is deposited with their very thin coating to defend the effect of optical transmittance from the front contact.

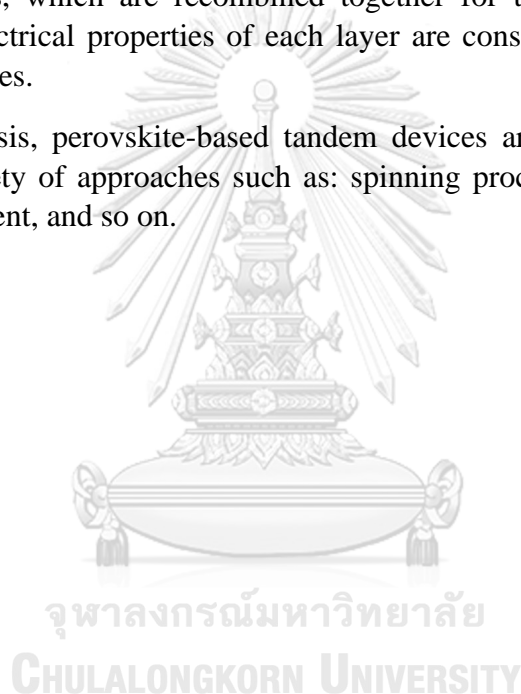
*Table 2. Responding between thickness and current of several materials.*

<b>Layer</b>	<b>Thickness (nm)</b>	<b>Current (mA/cm<sup>2</sup>)</b>
Glass	1.00 x 10 <sup>-6</sup>	0.2
ITO	50	0.77
ITO	100	3.56
ITO	150	3.68
TiO <sub>2</sub>	10	0.03
TiO <sub>2</sub>	40	0.03
TiO <sub>2</sub>	60	0.00
Spiro-OMeTAD	200	0.68
Spiro-OMeTAD	150	0.26
Perovskite Top subcells	400	14.16
Perovskite Bottom subcells	600	14.16
Gold	10	3.78
Gold	100	0.08
IZO	100	0.72
FTO	400	0.89
AgNWs	100	2.75
SnO <sub>2</sub>	10	0.00
C <sub>61</sub>	10	2.56
PEDOT: PSS	50	1.68

The most widely used materials are  $\text{TiO}_2$  and Spiro-OMeTAD as ETL and HTL in single-junction solar cells. Also, Spiro-OMeTAD acted as HTL is suggested to increase stability for work function in device. Recently,  $\text{NiO}_x$ , PEDOT: PSS and PTAA are introduced to invent as HTL for tandem cells [55]. However, Spiro-OMeTAD used as HTL to preserve good electrical qualification for a single-junction device while a double-junction device used the PEDOT as HTL that has optical transmittance properties better than the Spiro-OMeTAD. Finally, the next promising generation for the fabrication of ETL is using  $\text{PC}_{61}\text{BM}$  organic semiconductors when it can adjust optical properties in terms of solvent doping.

Regarding the 2T and 4T tandem solar cell models, several materials are invented in this work that is focused on the transparent contacts, ETL, buffer layer, and HTL sections, which are recombined together for the device. Hence, optical properties and electrical properties of each layer are considered to directly apply to tandem architectures.

In this thesis, perovskite-based tandem devices are pushed to achieve high PCE using a variety of approaches such as: spinning process, annealing, amount of solution, anti-solvent, and so on.



## CHAPTER III

### THEORY

#### 3.1 Band gap energy ( $E_g$ )

A semiconductor is a material that has an electrical conductivity between that of a conductor and an insulator. Figure 17 shows the band diagram of metal, semiconductor, and insulator. It consists of the conduction band ( $C_B$ ), the valence band ( $V_B$ ), and the fermi level ( $E_F$ ). Fermi level is demonstrated between the valence band and conduction band. The fermi level at absolute zero temperature is the highest energy level. The band gap of materials ( $E_g$ ) is the difference between the conduction band and the valence band. When a semiconductor obtains an external energy, e.g., sunlight that is equal or greater than the band gap, the electron will be excited from the valence band to the conduction band and become a free electron in the conduction band and a hole in the valence band. Since the band gap of an insulator is clearly broader than that of the semiconductor, the valence electron in an insulator cannot be excited to the conduction band and becomes a free electron.

A semiconductor can be divided into three types, which are i-type, N-type, and P-type. An N-type semiconductor is an intrinsic semiconductor (i-type) doped to increase the negative charge carriers, and the majority of the carriers of an N-type semiconductor are electrons. The P-type semiconductor is an intrinsic semiconductor (i-type) doped to increase the positive charge carriers, and the majority of the carriers of a P-type semiconductor are holes.

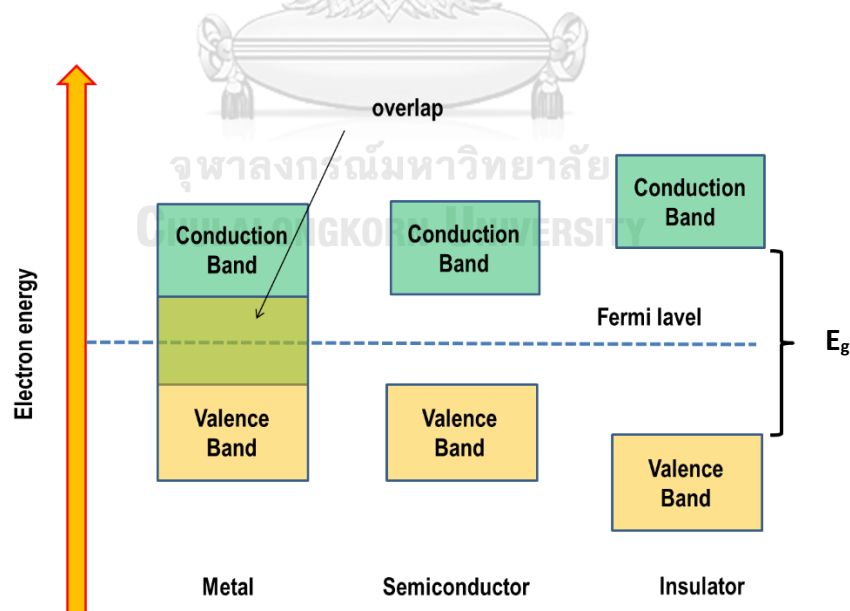


Figure 17. Working principles for metals, semiconductors, and insulators, respectively.

### 3.2 P-N junction

A semiconductor crystal has the n and p-regions when they are combined as the metallurgical boundary. It is called a "P-N junction." The p-n junction can be used as an isolated structure, a voltage-dependent capacitor, or a solar cell. Figure 18 depicts a P-N junction, which is a sandwich of N-type and P-type semiconductors. The P-type is on the right region, whereas on the left region is the N-type.

The junction is biased via a voltage ( $V$ ). The junction forward bias occurs when applying a positive voltage to the p-type region. When a negative voltage is applied to the p-doped region, this junction is called reversed-biased. The contact for the p-type region is called the anode, while the contact for the other region is called the cathode. Thus, in each of these regions, we have anions and cations.

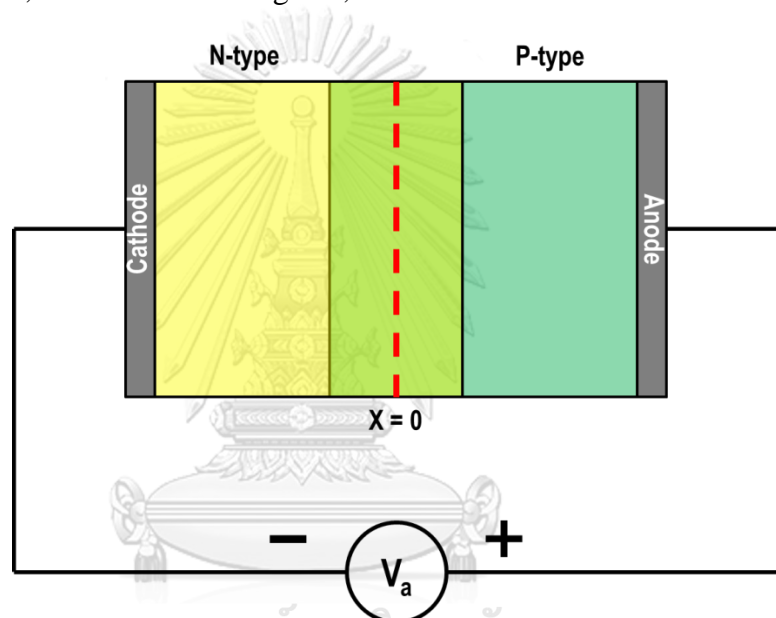


Figure 18. Schematic diagrams for circuit of a p-n junction.

The principle of PN-junction can be explained by a Gedanken experiment. After both semiconductor regions are brought together, the Fermi level of both regions should be equal (figure 19). Therefore, electrons in the N-type region flow to P-type and holes in P-type flow to N-type. The ionized donor in the N-type will act as a positive charge and the ionized acceptor will act as a negative charge, resulting in the electric field from N-type to p-type. This zone is called the depletion zone.

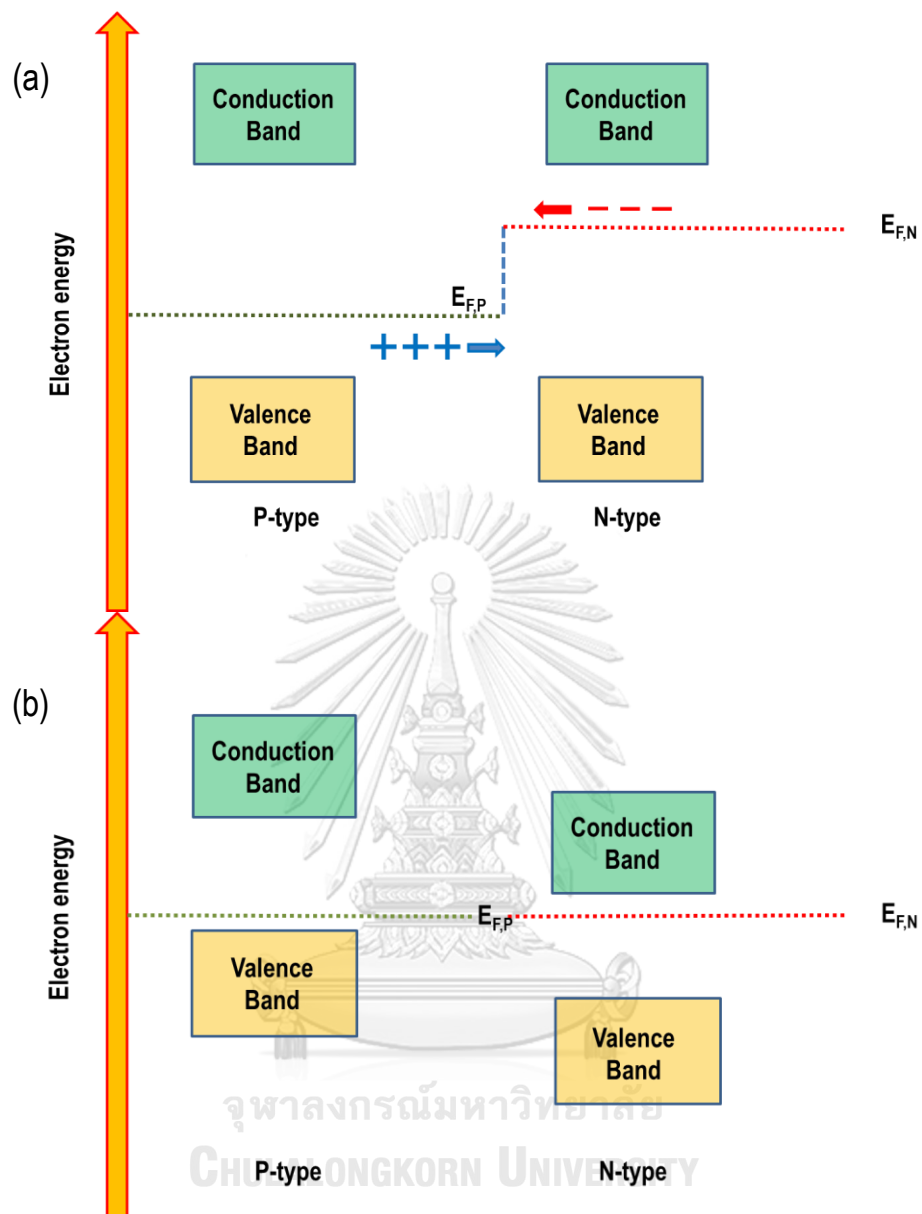


Figure 19. Energy band ( $E$ ) diagram of a P-N junction (a) before and (b) after merging the N-type and P-type regions.

In both semiconductor regions, as shown in figure 20, a space charge is created with a region of ionized donors and acceptors. Its name is the depletion zone.

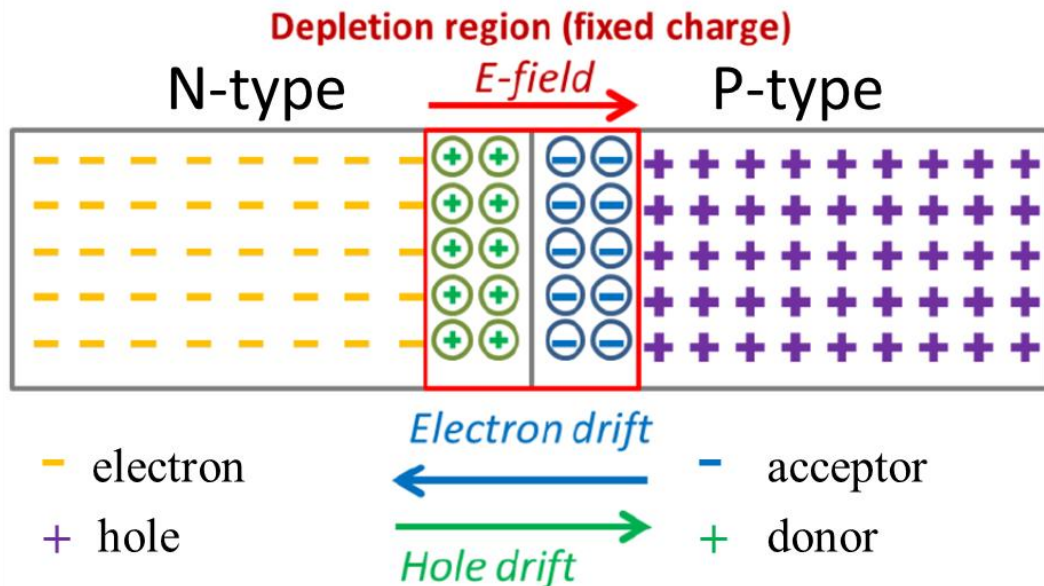


Figure 20. Schematic of the depletion zone.

### 3.3 I-V curve

The basics of the solar cell are that, from a basic science perspective, a solar cell is a combination of P-type and N-type semiconductors. Electrons ( $e^-$ ) are excited from the valence band to the conduction band after being activated by photon energy. Then electrons move from the P-type to the N-type zone resulting from an electrical field into the circuit. Finally, electrons will be collected at metal contact (see figure 21). Hence, when the P-N junction is biased, the photovoltaic parameters of the device, such as PCE, can be calculated by a computer program which shows the I-V curve.

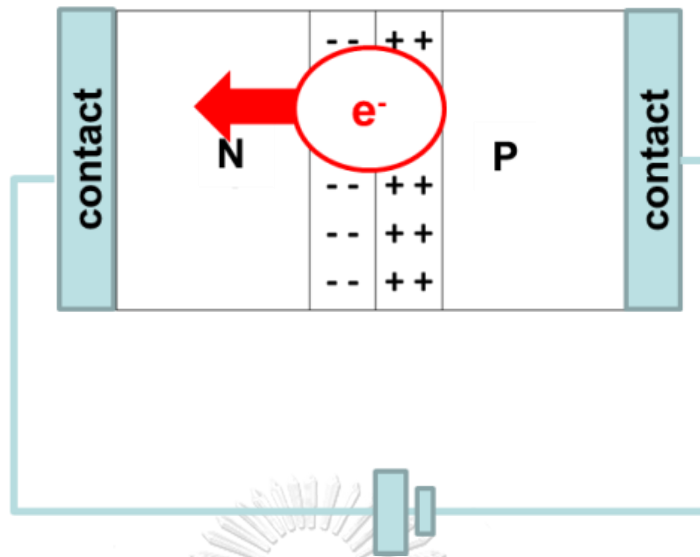


Figure 21. The electric field at the P-N junction drives the collection of photogenerated electrons and holes into N-type and P-type semiconductor regions, respectively.

### 3.3.1 Parameters for evaluating solar cells

Evaluation of solar cells consists of various parameters to examine the performance of a cell. The energy spectrum of the incident radiation intrinsically generates the amount of photocurrent. Since photovoltaic parameters are relative to the light source, the devices are measured under standard test conditions (STC). The STC for solar cells consists of the Air Mass 1.5 (1.5 AM) spectrum and is fixed with an incident power density of  $1000 \text{ W/m}^2$  and a temperature of  $25^\circ \text{C}$  [56].

#### 3.3.1.1 Current-voltage (IV) curve

The biased voltage on the device sweeps from forward bias ( $V > 0$ ) or reverse bias ( $V < 0$ ) and the IV curve will be attained. The IV curve demonstrates the current as a function of voltage and is used to determine the typical parameters, e.g., short-circuit current density and fill factor, and the behavior of devices within an electrical circuit.



### 3.3.1.2 Short circuit current density ( $J_{SC}$ )

Open circuit voltage ( $V_{OC}$ ) can occur under illumination and terminals are isolated. It occurs when the terminals are connected together. The output voltage ( $V$ ) is the range of 0 to  $V_{OC}$ , and the output current ( $I$ ) is the ratio of  $V$  to load resistance ( $R_L$ ). In the part of  $J_{SC}$  that can be determined as a formula as

$$J_{SC} = q \int b_S(E)QE(E)dE \quad (1)$$

Where  $q$  is the electronic charge  
 $b_S(E)$  is incident spectral photon flux density  
 $QE(E)$  is the cell's quantum efficiency.

Which device can produce that QEs corresponded to  $J_{SC}$ , the range  $E$  to  $E + dE$  on unit area in unit time is limited by the amount of photon energy.

### 3.3.1.3 Open circuit voltage ( $V_{OC}$ )

A load is connected between the terminals of a device and the terminals of which a potential difference exists. Then, additive voltage or bias in the dark can occur, which is dark current ( $I_{dark}$ ), which is an ideal diode. A form of

$$J_{dark}(V) = J_0(e^{qv/k_B T}) \quad (2)$$

For Equation (2),  $J_{dark}(V)$  is an ideal diode of dark current density

$k_B$  is Boltzmann's constant  
 $T$  is temperature in degrees Kelvin  
 and  $J_0$  is saturation current density [57].

Equation (3) is used to determine the  $V_{OC}$  for an ideal diode.

$$V_{OC} = \frac{k_B T}{q} \ln \left( \frac{J_{SC}}{J_0} + 1 \right) \quad (3)$$

### 3.3.1.4 Power conversion efficiency (PCE) and fill factor (FF)

The maximum power density ( $P_m$ ) is the maximum product of the corresponding voltage ( $V_m$ ) and current density ( $J_m$ ) of a device. A higher potential difference and a lower current result from  $R_L$ . Thus, both  $V_{OC}$  and  $J_{SC}$  values decreased, and they are now called  $V_m$  and  $J_m$ . The power conversion efficiency, or PCE, of a device is defined as the quotient of  $P_m$  and incident light power density ( $P_{in}$ ) as

$$PCE = \frac{J_m V_m}{P_{in}} \times 100 \quad (4)$$

The fill factor ( $FF$ ) is one of the important parameters because it tells the squareness of the J-V curve. The fill factor is defined as an equation (5). If the  $FF$  of a device is closed to 100%, the J-V curve is more square and close to an ideal device compared to  $FF$  that is closed to 0%.

$$FF = \frac{J_m V_m}{J_{sc} V_{oc}} \times 100 \quad (5)$$

The maximum power point for an ideal cell (the product of  $J_{sc}$  and  $V_{oc}$ ) is presented in the I-V curve and the  $P_m$  as shown in figure 22.

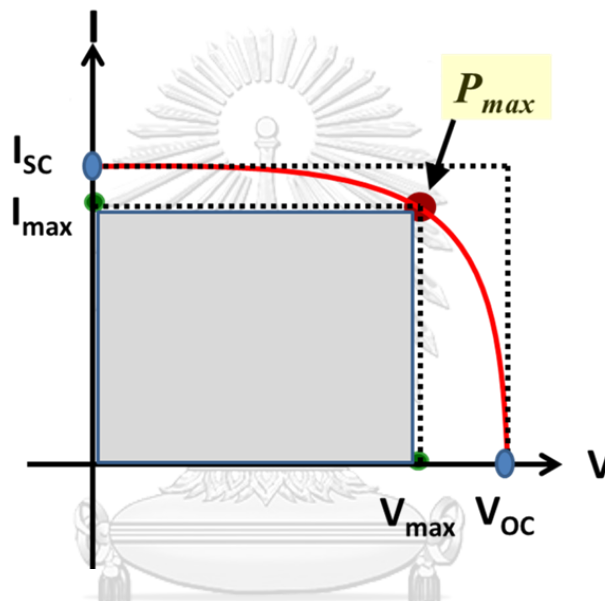


Figure 22. The I-V curve and PV curve of an ideal cell presentation of  $P_m$  at a bias of  $V_{max}$ . The  $FF$  value equals 1 when the I-V curve is in the area of the outer rectangle.

### CHULALONGKORN UNIVERSITY

#### 3.3.1.5 Parasitic resistances

An equivalent circuit to model a solar cell is added with series resistance ( $R_s$ ) and shunt resistance ( $R_{sh}$ ) as shown in figure 23. The resistance of the contact and leakage currents reduces the generated power by lowering the net current density. Both  $R_s$  and  $R_{sh}$  are two parasitic resistances in series and in parallel, respectively [57].  $R_s$  originates from the resistance of a cell material and resistive contacts, and  $R_{sh}$ , or parallel resistance, is caused by leakage currents at the edges, through the cell, and between contacts of different polarity.

The effect of resistance within a device is a reduction of the maximum power density. The device performs well, in which  $J_{sc}$ ,  $V_{oc}$ , and fill factor ( $FF$ ) are improved when  $R_s$  is the lowest and  $R_{sh}$  is the highest. In theory, a perfect device should have  $R_s = 0$  and  $R_{sh} = \text{infinity}$ .

The present model does not take into account capacitance elements such as charge traps that occur in charge trapping and detrapping processes between delayed photocurrent responses, seen as hysteresis in J-V curves.

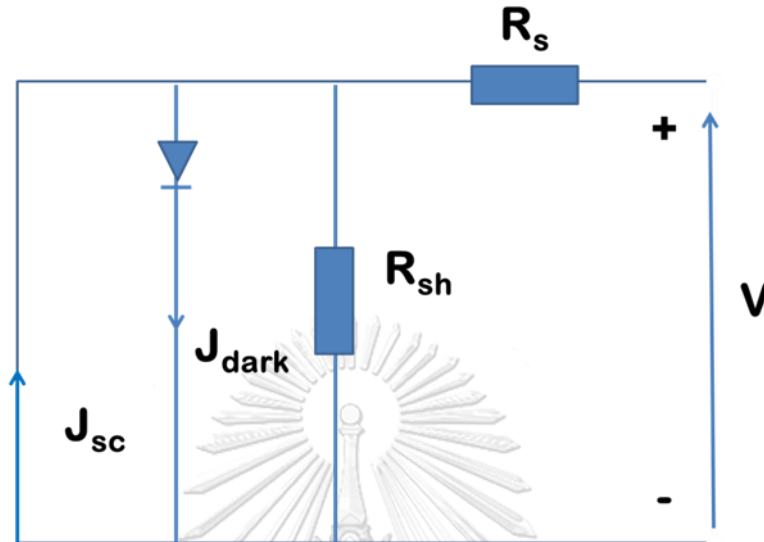


Figure 23. Schematic circuit of solar cell.

### 3.4 Hysteresis and charge recombination

The J-V curve is also dependent on the scan direction and rate. For example, figure 24 illustrates the J-V curves of the device with various directions and rates of scanning from the equipment. The direction of the scan is represented as backward or reverse scan, when scanning direction via sweeping from positive (open circuit voltage;  $V_{OC}$ ) to negative (short circuit voltage;  $V_{SC}$ ), while the opposite direction of scanning is called forward scan. This difference shows the J-V curve from reverse scan (red line) and forward scan (black line), as shown in figure 13a. This phenomenon is called current-voltage (I-V) hysteresis. The hysteresis behavior can indicate a problem or reveal an abnormal work function of a device. However, the effect of hysteresis behavior cannot be clearly understood. To find information about problems with this behavior, one must use numerous mechanisms that can analyze the causes. For perovskite solar cells, the hysteresis phenomenon is determined by mechanisms caused by

- (1) ferroelectric polarization [58]
- (2) ion migration [59]
- (3) charge trapping [60]
- (4) capacitive effects [61].

The requirements to accurately determine the problem are

- (1) fabrication of the solar cell appropriately and measurement of the solar device area
- (2) calibration of the illumination light source
- (3) determination of the steady state  $V_{OC}$ ,  $J_{SC}$  and monitoring on computer
- (4) Measurement of the J-V graph in reverse and forward directions using varying scan rates
- (5) Measurement of steady-state photocurrent at various sweeping voltages.

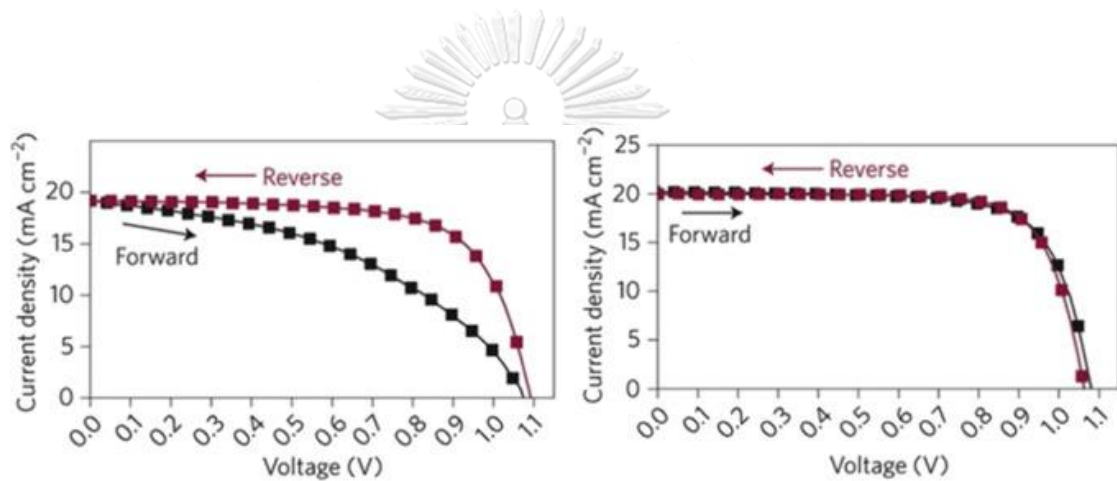


Figure 24. The J-V curve of varying directions and rates of scanning from planar PSCs [62].

## CHAPTER IV

### FILM FABRICATION AND CHARACTERIZATION

In this chapter, the fabrication of all films on PSCs including a spin-coating and evaporation process will be described. Moreover, the etching process, cleaning substrate, and materials for preparing the fabrication of PSCs are described in this chapter as well. In addition, the characterizations are also described, that is UV-VIS spectrophotometer, scanning electron microscope (SEM), atomic force microscopy (AFM), current-voltage (I-V) measurements, contact angle, and external quantum efficiency (EQE) were used to investigate the properties of all thin films and the PSCs.

#### 4.1 Main deposition technologies of thin-film

##### 4.1.1 Solution deposition methods for perovskite device fabrication

A simple perovskite device is deposited with scalable solution deposition methods such as blade coating, slot die coating, spray coating, or spin coating.

The blading coating method is to spread solution on substrates with a blade to obtain wet thin films as shown in figure 25. This technique can be controlled by keeping a distance between the blade and the substrate, then the blade moves across the substrate at a set speed. This method reduced perovskite ink waste more than the spin coating method. PSCs from this method have achieved a PCE > 19% [63, 64].

The second method, slot-die coating, is suggested to use a perovskite ink similar to the blade coating process [65, 66] as revealed in figure 26. The ink solution is applied above the substrate so that it can be controlled with slot-die coating [65]. The perovskite device fabricated by using this method still has a lower PCE than blade coating processing. Even so, the advantages of this method are yielded, and reproducibility is better than blade coating.

For spray coating, tiny liquid droplets are dispersed onto substrates with a nozzle, which is one part of spraying coating tools to generate droplets, such as flowing fast gas for pneumatic spraying and vibrating ultrasonic for ultrasonic spraying, as shown in figure 27 [67, 68]. Usually, both two sprays are commonly used as deposition processes and form a dense oxide layer on perovskite devices. However, those spraying fabrications show random droplet size and placement. Therefore, the substrate and solvent temperatures must be maintained as the rate of spraying increases. The spraying rate is controlled by the voltage that is applied between the spray nozzle and substrate.

On a laboratory scale, for the generation of thin films, the simplest preparation for applying a uniform film fabrication on a substrate is the spin coating method (Prasad et al. (2005), Tongpool and Yoriya (2005) [69, 70]). Finally, the material is diluted with a suitable solvent. A uniform liquid film covers the surface because of the centrifugal force from that spreading liquid. Then, the substrate coating is deposited with solution at various spinning speeds to determine the thickness of the film. The solvent of each solution is removed by the spinning process and annealing

process, which depends mainly on each solvent. The solvent evaporation rate depends mainly on the solvent.

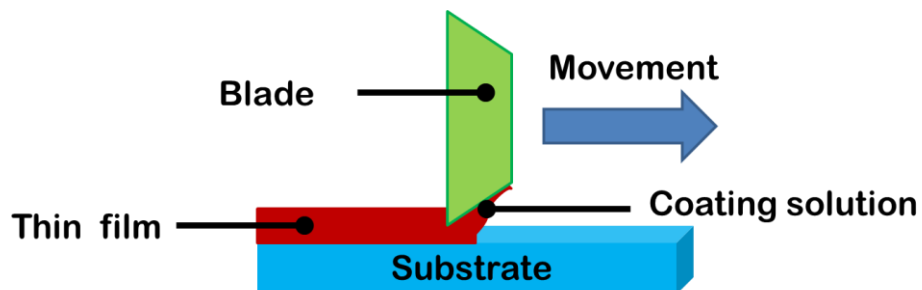


Figure 25. Blade coating method.

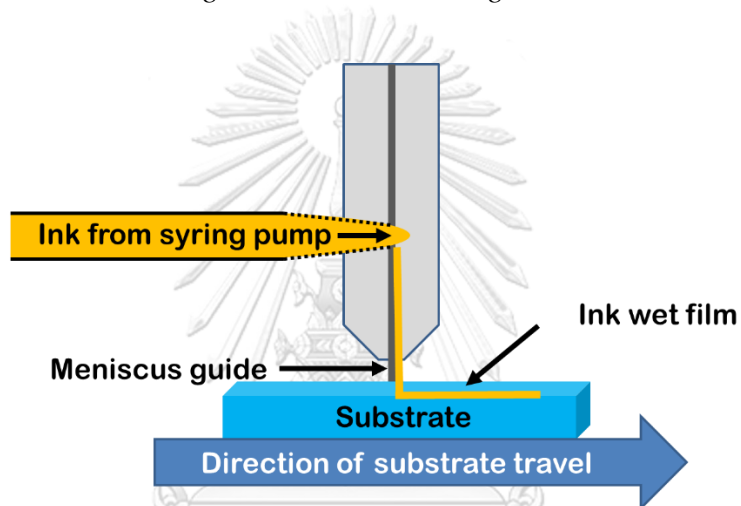


Figure 26. Slot-die coating method.

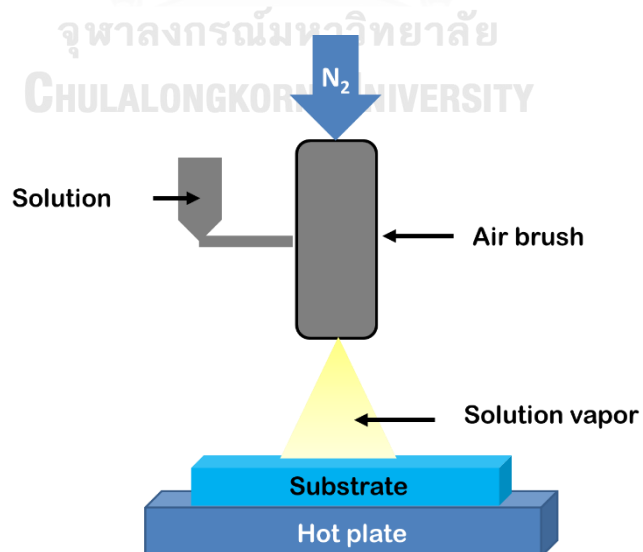


Figure 27. Spray coating method.

Using spin coating for thin films is widely studied. A schematic of the spinning coating is shown in figure 28. This method has three steps.

1. The solution is dropped on the substrate. Then, the dispensing solution covered the substrate.
2. The solution is adjusted to a thinner film with a high spinning speed.
3. The solvent is removed during the spinning process.



Figure 28. Spin-coating method.

In this thesis, the spin coating method was selected to fabricate all layers on PSCs. Because spin coating is widely used in micro-deposition and obtains a higher PCE than other methods, as shown in Table 3. It is used to apply thin films with a thickness  $< 10$  nm and fabricate uniform thin films onto flat substrates by centrifugal force, and the apparatus used for this technique is called a spin coater. Moreover, the spin-coating can control the thickness of the thin film by the speed of spinning, as shown in figure 29. A solution of material is dispensed onto the center of a wafer, which is then rotated at high speed. However, the concentration of solution and the solvent are another factor for film thickness.

Table 3. Comparison of scalable solution processing for perovskite device.

Processing	Roll to roll	Pattern	Power conversion efficiency (PCE) (%)
Blade coating	Yes	No	19.7 [64]
Slot-die coating	Yes	Yes	17.7 [66]
Spray coating	Yes	Yes	19.4 [67]
Spin coating	No	Yes	25.0 [71]

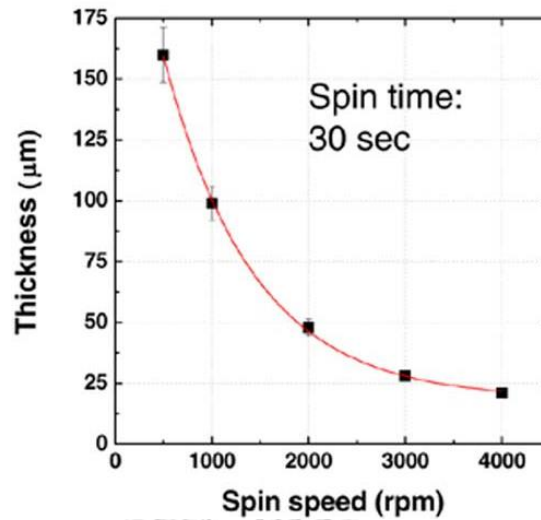


Figure 29. Thickness of spin-coated thin films for different spin speed with spin time fixed at 30 s [72].

#### 4.1.2 Thermal Evaporation

The thermal evaporation deposition method is the simplest technique that is shown in figure 30. The source material inside a vacuum chamber is baked with an electrical current passing through a metal plate where the source material is deposited. Afterward, surface atoms of material obtain sufficient energy that they can leave the surface to condense and coat the substrate, which is above the evaporating source material. In general, a boat in an evaporation vacuum chamber is used as a deposition position for materials.

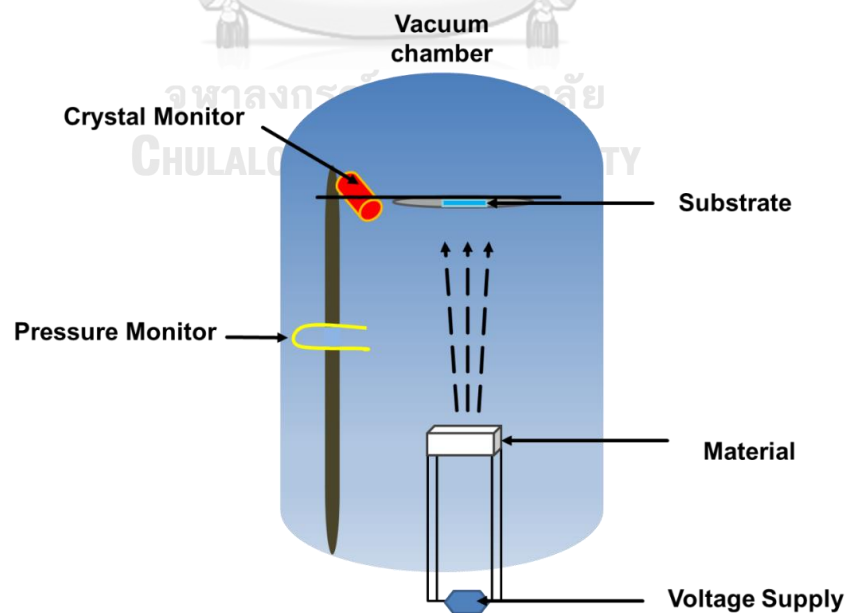


Figure 30. Illustration of a thermal evaporation system.



## 4.2 Materials for PSCs fabrication

The conventional cell structure of FTO/Cp-TiO<sub>2</sub>/Mp-TiO<sub>2</sub>/perovskite/Spiro-OMeTAD/Au is applied in this thesis. Meanwhile, the inverted perovskite solar cell structures of FTO/NiO<sub>x</sub>/perovskite/PC<sub>61</sub>BM/BCP/Au, FTO/PEDOT: PSS/perovskite/PC<sub>61</sub>BM/BCP/Au, FTO/PTAA/perovskite/PC<sub>61</sub>BM/BCP/Au or Ag are studied as well. A device consists of four cells with an active area of 0.06 and 0.2 cm<sup>2</sup> for each. All samples were made with a 3 cm x 3 cm FTO glass substrate whose sheet resistance is 15 Ω/sq. All used substances are displayed in Table 4.

*Table 4. Materials used in the experiment of the conventional and inverted structure.*

<b>Material</b>	<b>Attribute</b>	<b>Vendor</b>
Cp-TiO <sub>2</sub>	200 g	greatcellsolar
Mp-TiO <sub>2</sub> (Ti-Nanoxide T600/SC)	100 g	Solaronix
Mp-TiO <sub>2</sub> (Ti-Nanoxide T300/SC)	100 g	Solaronix
Mp-TiO <sub>2</sub> (30NR-D Titania Paste)	50 g	Greatcellsolar
NiO <sub>x</sub> (Nickel oxide)	≥ 99%	Sigma-Aldrich
Spiro-OMeTAD	>99.5%	Xi'an polymer light technology corp. (Xi'an, China)
PEDOT: PSS (A1 4083)	M121-100 ml	Ossila
PEDOT: PSS (HTL Solar 3)	M125-25 ml	Ossila
	CAS# 155090-83-8	
PEDOT: PSS (PH 1000)	M122-100 ml	Ossila
	CAS# 155090-83-8	
PbI <sub>2</sub>	99.99%	Xi'an polymer light technology corp. (Xi'an, China)
CH <sub>3</sub> NH <sub>3</sub> I (MAI)	CAS RN: 14965-49-2	Dyesol
PTAA	MW ≥ 6000	Xi'an polymer light technology corp. (Xi'an, China)
PC <sub>61</sub> BM (phenyl-C61-butyric acid methyl ester)	> 99%	Xi'an polymer light technology corp. (Xi'an, China)
BCP (Bis(trifluoromethane) sulfonamide lithium salt)	>99.0%	Sigma-Aldrich
F4-TCNQ (2,3,5,6-Tetrafluoro-7,7,8,8-tetracyanoquino dimethane)	1 g, No.:LT-E208	Luminescence Technology
Li-TFSI (lithium bistrifluoromethanesulfonimide)	≥ 99.0%	Sigma-Aldrich
t-BP (4-tert-butylpyridine)	96%	Sigma-Aldrich
DMF (N,N-Dimethylformamide)	> 99.8%	Sigma-Aldrich
DMSO (N,N-Dimethylsulfoxide)	≥ 99.9%	Sigma-Aldrich
CB (chlorobenzene)	> 99.8%	Sigma-Aldrich

Material	Attribute	Vendor
Acetonitrile	99.8%	Sigma-Aldrich
TO (toluene)	$\geq 99.9\%$	Merck
IPA (2-Propanol)	$> 99.5\%$	Sigma-Aldrich
Ethylene glycol	99.8%	Sigma-Aldrich
Ethylenediamine	$\geq 99.5\%$	Sigma-Aldrich
Ethanol	$\geq 99.9\%$	Merck
ZINC POWDER	99.8%	Ajax Finechem

### 4.3 Characterization techniques

#### 4.3.1 Device characterization

Applying an external potential bias to the cell while recording the generated photocurrent with a digital source meter (Keithley model 238) can be used to determine the current density-voltage (J-V) characteristics. A solar cell is measured by a solar simulator (Yamashita Denso; model YSS-80) with an active area of 0.06 and 0.2 cm<sup>2</sup>. The voltage sweep was in the range of -0.1 to 1.2 V. J-V measurements were taken at 25 °C.

#### 4.3.2 Absorption and transmission measurements

A UV-VIS spectrophotometer (Shimadzu; model UV-1601PC) is used to measure the optical properties of each sample. Materials can absorb photon energy ( $E_{ph}$ ) in a range of different wavelengths. The absorption  $E_{ph}$  depends on material concentration.

Transmission is determined by exposing the original light beam (or incident light;  $I_0$ ) to the sample, and measuring transmission light ( $I_T$ ). A detector is used to charge  $E_{ph}$  transfer to electricity, such as a silicon photodiode and a photomultiplier tube detector.

The relation of transmission (T), absorption (A), and reflectance (R) are shown in the below equation.

$$R=I_R/I_0 \quad \text{and} \quad T+R+A=1,$$

which  $I_T$  is intensity of transparent of light  
 $I_R$  is intensity of reflection of light  
 $I_0$  is intensity of incident light  
 and  $d$  is film thickness.

From graph (31), it can show that  $I_T = I_0 e^{-\alpha d}$

and percent transmission (%T) of light  $\%T = \frac{I_T}{I_0} \times 100$

so, absorption coefficient is related to new equation  $\alpha = \frac{-1}{d} \ln \left[ \frac{\%T}{100} \right]$ .

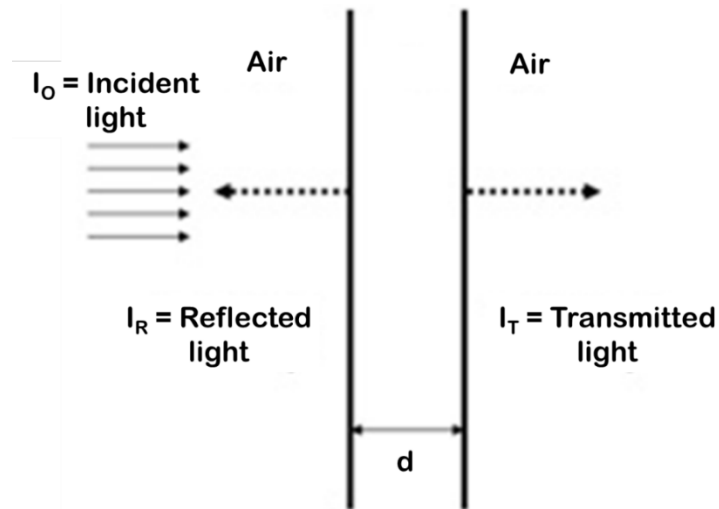


Figure 31. A diagram depicting the relationship between the intensity of film and the thickness of film.

#### 4.3.3 Atomic force microscope (AFM)

The atomic force microscope (AFM) (Veeco; model Dimension 3100) shown in figure 32 was used to measure properties at a nanometer scale such as magnetism, height, and friction. A probe of the AFM is touched to the surface of the sample to measure and collect data. After the scanning AFM probe microscope raster-scans are finished, an image is formed and shown on the computers' screen.

Figure 33 shows the function of an Atomic Force Microscope (AFM). It has three major working principles that include surface sensing, detection, and imaging. The laser source of AFM transports its beam to the probe tip, which is the end of the cantilever. After that, the detector detects the reflection of the beam from the cantilever.

The flat surface of the sample is measured by scanning the cantilever above a surface area of interest. The deflection beam is produced by the position-sensitive photodiode (PSPD). Its imaging map of the surface depends on how raised or how low the sample surface is.



Figure 32. An atomic force microscope (AFM) on the right with controlling computer on the left.

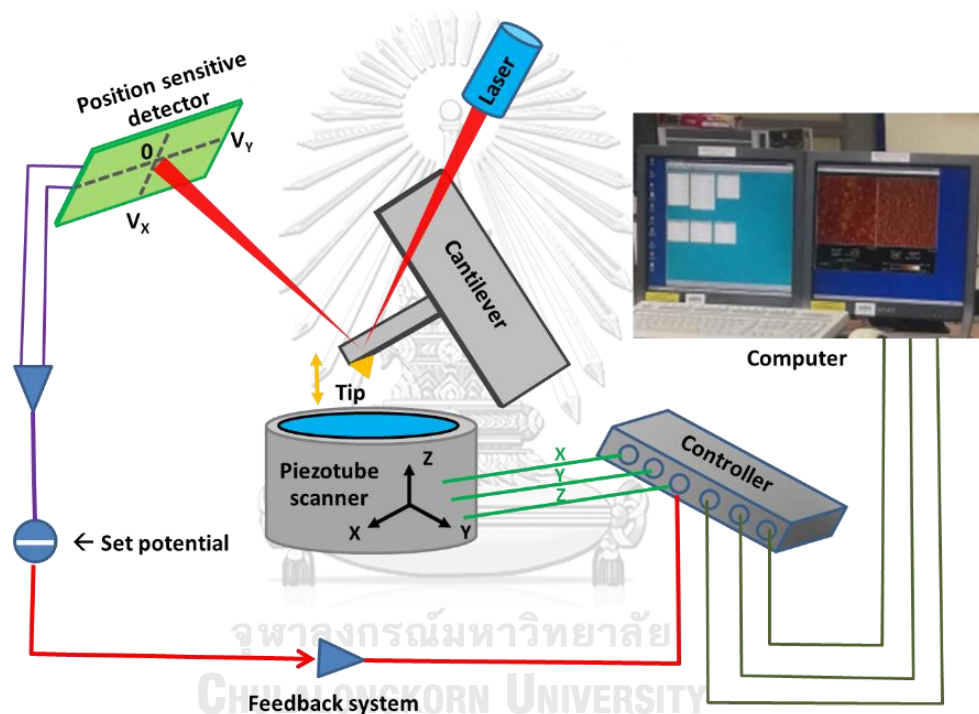


Figure 33. Schematic illustration of in situ atomic force microscopy (AFM).

#### 4.3.4 Contact angle

The surface properties of materials can be characterized by contact angles,  $\theta$  (theta). Contact angle data depends on the quality of the substrate surface, such as roughness and heterogeneity of the substrate surface. Normally, the contact angles are accurately determined between the tangent of the drop surface at the contact line (which is a section of the interaction between the solid and the liquid) and the surface (see figure 34).

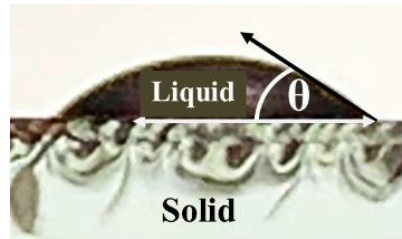


Figure 34. An example of an FTO surface with a contact angle.

If the contact angle is close to  $0^\circ$ , the liquid is very strongly attracted to the hydrophilic solid surface. For hydrophobic solid surfaces, the surface will have a contact angle of up to  $90^\circ$ . If the contact angle is equal or larger than  $90^\circ$ , the solid surface is called super-hydrophobic, as shown in figure 35 below.

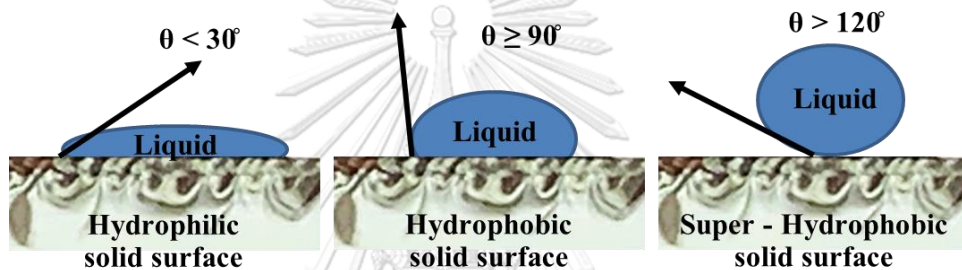


Figure 35. (a) a low contact angle ( $\theta < 30^\circ$ ) with good wettability, known as hydrophilic; (b) a higher contact angle, known as hydrophobic ( $\theta \geq 90^\circ$ ); and (c) a high contact angle with poor wettability ( $\theta > 120^\circ$ ), known as super-hydrophobic.

#### 4.3.5 External quantum efficiency (EQE) measurement

An external quantum efficiency (EQE) measurement is used to observe solar cells' behavior in a specific range of wavelengths. The EQE technique was used in this study to investigate the photoinduced degradation of tandem solar cells with Cu (In, Ga)Se<sub>2</sub> (CIGS) acting as bottom cells and PSCs acting as top cells. Normally, an electron-hole pair on the solar device is produced from each photon for an ideal solar cell. Afterward, they will go toward the depletion region and then be separated and collected. If all these photons did not have more energy than bandgap energy ( $E_g$ ), they could not be photocarriers. The quantum efficiency (QE) is determined first before calculating the EQE value. The QE is the ratio of the number of all carriers collected by the solar device to the number of all photons of a given energy incident on the solar cells. Nevertheless, all these photons of absorbing wavelength and collecting the resulting minority carriers occurred, and then the QE at that particular wavelength is unity. A function of wavelength or of energy may be determined by the QE. If photon energy is lower than the  $E_g$ , the QE value is zero. This value can be calculated with current density (J) from current-voltage measurement.

Figure 36 shows a QE curve for an ideal solar device by the tan/gold square line. The recombination effects from electron and hole pairs are defected on the device, reducing the QE for most solar cells. Meanwhile, the collection effects may also be the QE, such as carriers generated at wavelengths of 350 nm (blue light), which is very close to the device surface. In addition, at wavelength  $\sim 800$  nm (green light) demonstrated reducing the QE that may be effects of an absorption in the bulk of a solar. Thus, the QE can be measured as the collection probability of the generation profile of a single wavelength and normalized to the incident number of all photons at that wavelength.

The effect of optical losses from transmission and reflection is used to achieve the external quantum efficiency (EQE) curve. If both transmission and reflection are not lost, which means the solar device can generate collectable carriers that are the internal quantum efficiency (IQE).

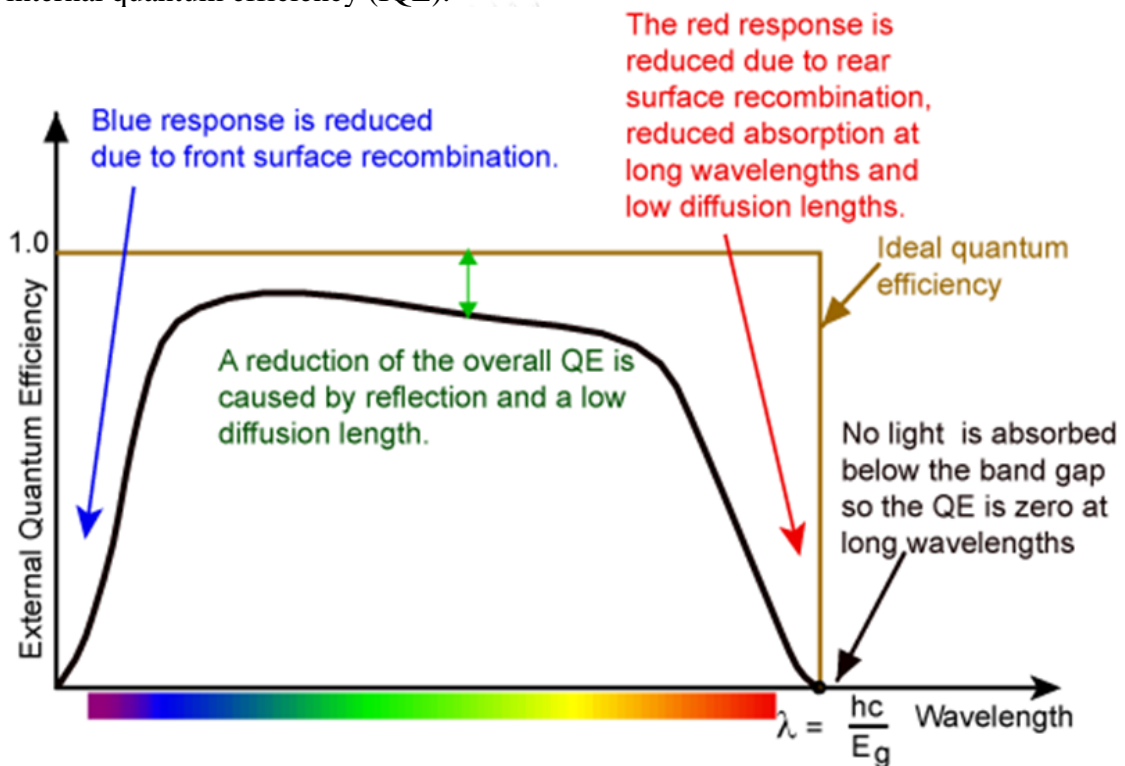


Figure 36. External quantum efficiency (EQE) of solar cell [73].

#### 4.3.6 Scanning electron microscopy (SEM)

Scanning electron microscopy (SEM) is the common method for imaging the microstructure and morphology of materials. The SEM is used in the semiconductor industry and typically provides two-dimensional images by generating contrast of features on a surface by differential charging. SEMs generally have a resolution of tens of nanometers, with the best field emission SEMs approaching a resolution of 1.5 nm. An electron beam in SEM has low energy, which is radiated to the material. It scans the sample surface. In 2003, Sampath Kumar et al. reported that multi-interactions occur as the beam reaches and enters the material, which leads to the emission of photons and electrons from or near the sample surface. An image is

formed by receiving signals produced by the electron–sample interactions that are detected with different types of detectors depending on the mode of SEM being used. A SEM is composed of several components (see figure 37), including:

- The electron gun is set on top of the column and emits electrons. Typically, electron energy levels accelerated to 0.1-30 keV are then measured.
- Forming high-resolution images was made with a high-diameter electron beam from a hairpin tungsten gun.
- Forming a small concentrated electron spot on the sample is touched by the electron beam, which controls focus and shape with electromagnetic lenses and apertures.
- A high-vacuum environment is allowed to reduce the number of scattered or absorbed electrons in the air.

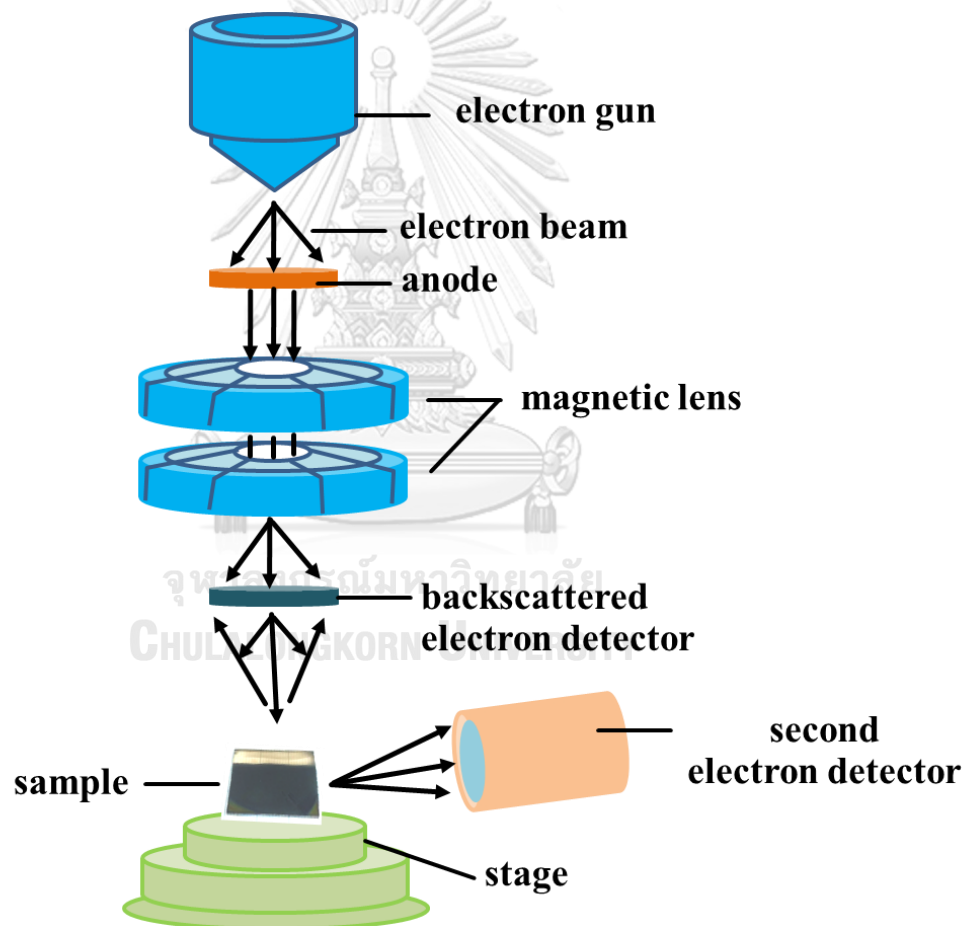


Figure 37. Schematic drawing of the typical Scanning Electron Microscope (SEM) column.

#### 4.4 Cleaning the surface of FTO glass substrate

Fluoride doped tin oxide (FTO) coated glasses were used as the substrates on PSCs. The substrate's surface needs to be cleaned with solvents because the FTO surface has contaminants such as oil, dust, etc. Suitable solvents such as water and water-alcohol mixtures can remove contaminants. They are used to remove polar contaminants, which are polar solvents. Non-polar solvents can be used to remove non-polar contaminants. Both polar and non-polar can be cleansed from the substrate by detergents containing wetting agents. The interfacial energy between different materials is reduced by wetting agents, which lower the surface energy of liquids and surfactants, such as oil and water. Various methods of mechanical disturbance and suitable addition of cleaning fluids are used to remove particulate contaminants, such as spraying, ultrasonic and mega sonic cleaning methods. In this work, the ultrasonic cleaner is used to immerse the substrate in alcohol and adjacent collapsing cavitation bubbles, which remove dust from the surface while operating at 18-120 kHz.

In cleaning processes as shown in figure 38, FTO glass was cleaned by dipping in detergent solution with the ratio of typically deionized water (DI water) to the detergent solution being 1 : 30 (30 ml of detergent solution in 1,500 ml of DI water) for 30 min. Afterward, FTO glass was washed with DI water to remove bubbles of detergent solution. After washing, the substrate was dipped in DI water for 30 min. And then, the FTO glass substrate was cleaned with acetone and isopropanol (IPA) by dipping the substrate in each solution for 20 min, respectively. To prevent particles from sticking firmly on the wet surface during drying, the substrate can be blown off with nitrogen gas ( $N_2$ ) as fast as possible to remove absorbed fluids.

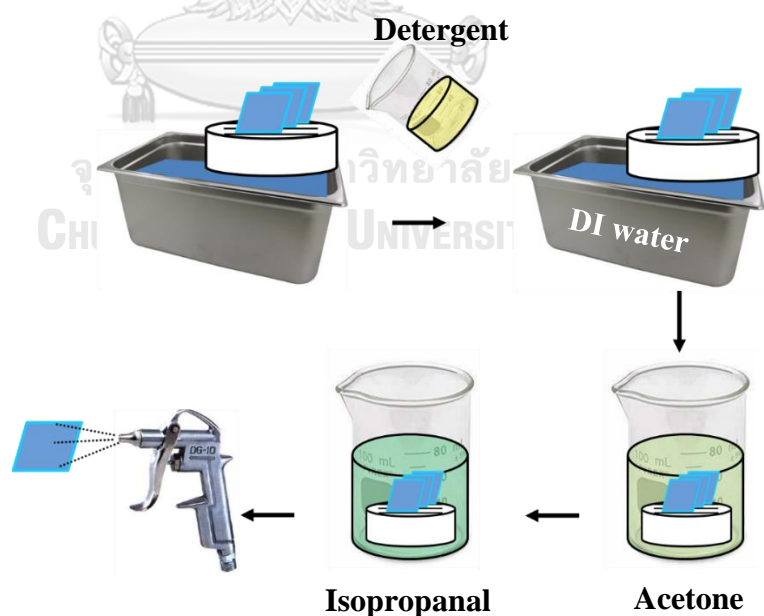


Figure 38. Cleaning FTO surface method.



#### 4.5 Etching FTO

A FTO (fluorine-doped tin oxide) conductive thin film, which is coated on a glass substrate, is a transparent conductive metal oxide that can be used as transparent electrodes for perovskite solar cells. But some parts of FTO must be removed to prevent short-circuit. Etching-FTO is chosen to mask the area. This can be done with photoresists, resistant masks, or kapton tape that is resistant to the etching solution. The FTO surface without kapton tape is coated with zinc powder, and then hydrochloric acid is added to the zinc powder. Once the reaction is finished, remove the kapton tape as seen in figure 39.

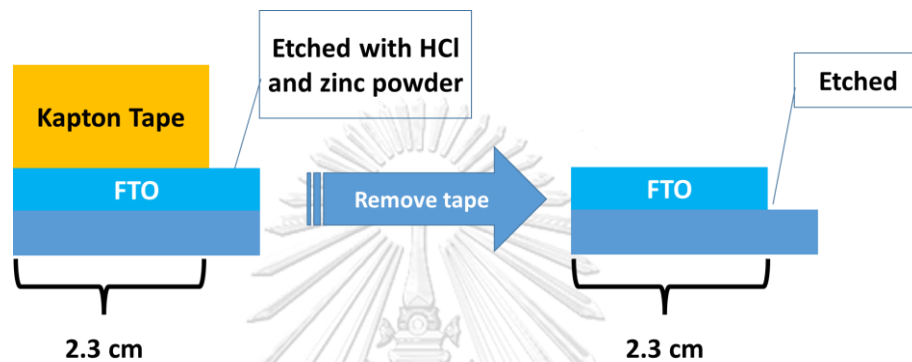


Figure 39. Etching FTO surface method.

#### 4.6 UV-Ozone cleaner

A UV-Ozone cleaning procedure is used to not only ensure that the surface is non-acidic, dry, and non-destructive atomic surface. But also remove contaminants such as dust and salts which cannot be changed to volatile products by oxidizing action. This process is inexpensive to set up and operate at room temperature, as shown in figure 40.

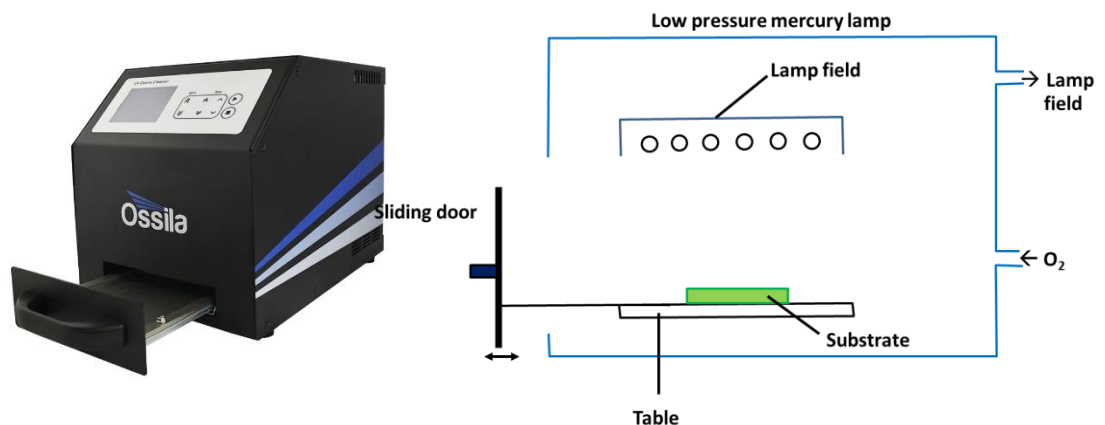
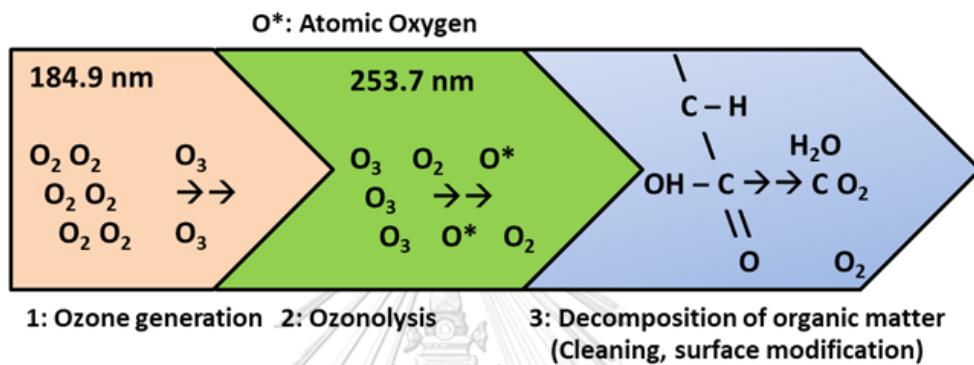


Figure 40. The UV Ozone cleaner (left) and the inside of the UV Ozone cleaner (right).

Intense wavelengths of 185.9 nm and 253.7 nm of ultraviolet light are generated within the UV-Ozone mechanism. The 184.9 nm wavelength produces O<sub>3</sub> and excites organic molecules on the surface, as shown in figure 41.

(a)



(b)

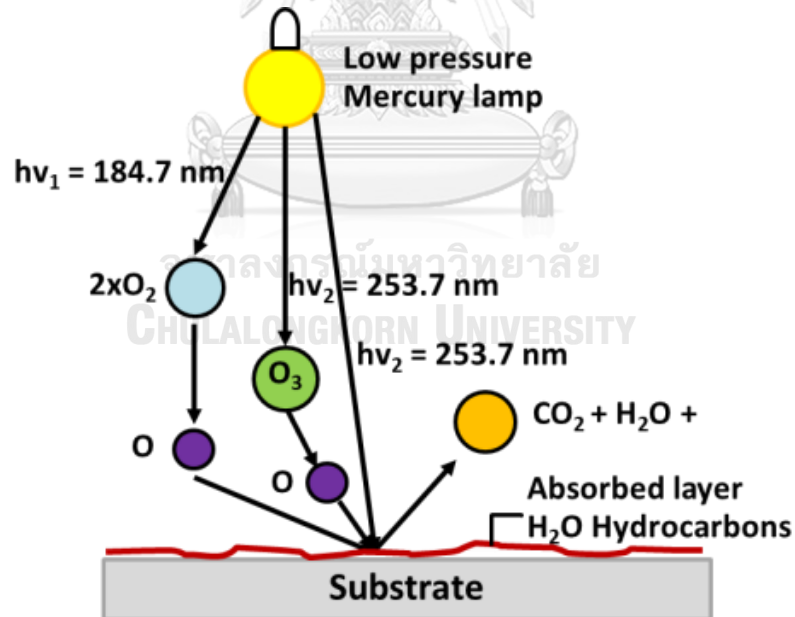


Figure 41. (a) Chemical reaction, (b) Principle of UV ozone treatment.

## CHAPTER V

### EXPERIMENTS, RESULTS AND DISCUSSION

In this chapter, the results of all layers on PSCs and the development of multi-junction (tandem) devices, in which PSCs act as top subcells, are discussed. All layers are fabricated by spin coating and their properties are discussed in terms of optical absorption, optical transmission, surface morphology, crystal structure, rough mean square (RMS) roughness, contact angle, external quantum efficiency (EQE), and I-V characteristics.

#### 5.1 Normal structure PSCS

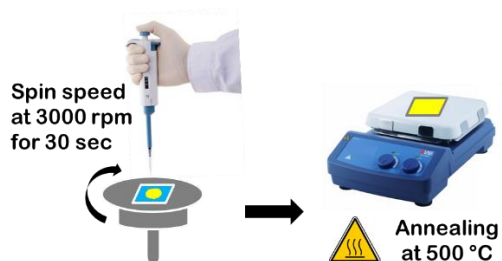
##### 5.1.1 Finding suitable Mp-TiO<sub>2</sub> on normal PSCs

Titanium dioxide (TiO<sub>2</sub>) is chemically inert, stable under sunlight, whose band gap ( $E_g$ ) values is  $\sim 3.0$  eV and very opaque [74], which has led to promising photovoltaic applications. Naturally, TiO<sub>2</sub> absorbs only UV ray. The compact and uniform TiO<sub>2</sub> electron transport layer (ETL) is prepared from a high temperature processing to improve the crystallinity of TiO<sub>2</sub> material, which leads to the aggregation of small particles. In this work, the normal perovskite solar cells (PSCs) structure is based on methylammonium lead iodide (MAPbI<sub>3</sub>) via a two-step spin coating method. The mesoporous TiO<sub>2</sub> (Mp-TiO<sub>2</sub>) is varied in thickness from 300 nm to 500 nm, where Mp-TiO<sub>2</sub> is directly coated on a compact TiO<sub>2</sub> (Cp-TiO<sub>2</sub>)/FTO substrate by varying the type of Mp-TiO<sub>2</sub> solution, and spin speed. The Mp-TiO<sub>2</sub> ETL thickness can improve photovoltaic properties of PSC performance such as open circuit voltage ( $V_{OC}$ ), fill factor (FF), and current density ( $J_{SC}$ ) because of the Mp-TiO<sub>2</sub> constitution, enhancing the contact area for electron injection at the interface between ETL and perovskite film and decreasing the distance of carrier transport [75, 76].

In this study, a Cp-TiO<sub>2</sub> layer was coated on the FTO surface substrate at a spin speed of 3000 rpm for 30 s and then heated on the hotplate at 500 °C for 30 min, as shown in figure 42(a). The Mp-TiO<sub>2</sub> is then deposited on the Cp-TiO<sub>2</sub> surface with different types of Mp-TiO<sub>2</sub> between Ti-Nanoxide T600/SC material and Ti-Nanoxide T300/SC material under a spin speed of 5000 rpm for 30 s and then baked at 500 °C for 30 min, as shown in figure 45(b). As shown in figure 42(c)-(d), the 400 nm thick perovskite films were made by combining PbI<sub>2</sub> film (0.461 g PbI<sub>2</sub>/1 ml DMF (N,N-Dimethylformamide)) and methylammonium iodide (MAI) solution (0.010 g MAI/1 ml IPA). The PbI<sub>2</sub> solution is stirred on a hot plate at 70 °C for 12 hours while the MAI solution is stirred at room temperature. They are kept in the glovebox at a relative humidity (RH) of less than 30%. The PbI<sub>2</sub> solution plays as the first precursor is covered above the electron transport layer (ETL) at a spin speed of 3000 rpm for 30 s and then residual solvent is removed on a hot plate at 70 °C for 20 min. The second precursor solution is the MAI solution that is deposited over the PbI<sub>2</sub> surface twice at a spin speed of 2000 rpm for 20 s, and each spin MAI solution is loaded on the PbI<sub>2</sub> film for 30 s (called loading time for 30 s). Then it is annealed at 120 °C for 15 min. spiro-OMeTAD as hole transport layer (HTL) is spin-coated above the top of the perovskite film at 3000 rpm for 30 seconds. All samples are kept in the dry box for 12 hours before the 80-100 nm thick Au metal contact is thermally evaporated on HTL. 0.0723 g of spiro-OMeTAD powder is mixed in 1 ml of CB and 28.8  $\mu$ l of 4-tert-

butylpyridine (t-BP), and then 0.520 g of lithium bistrifluoromethanesulfonimide (Li-TFSI) salt is mixed in 1 ml of acetonitrile.

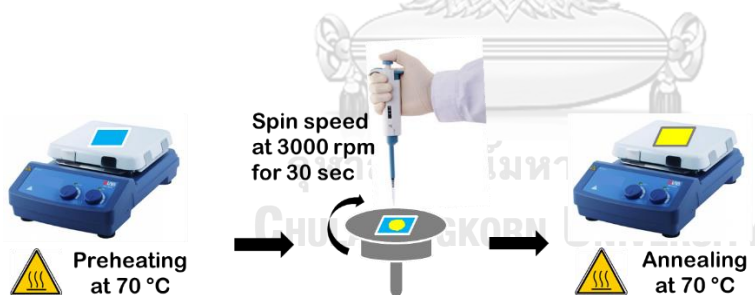
(a) Cp-TiO<sub>2</sub> film



(b) Mp-TiO<sub>2</sub> film



(c) PbI<sub>2</sub> film



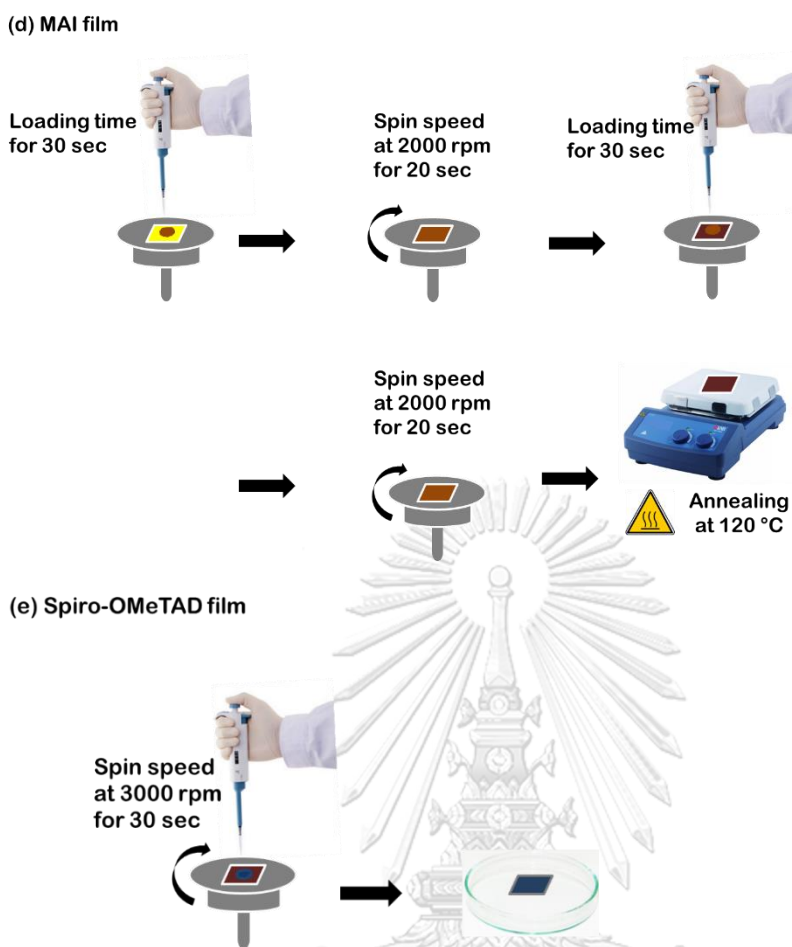


Figure 42. Fabrication of inverted perovskite device processes; (a)  $Cp-TiO_2$  film, (b)  $Mp-TiO_2$  film, (c)  $PbI_2$  film, (d) MAI film, and (e) spiro-OMeTAD film.

#### Results and discussions of finding suitable $Mp-TiO_2$ on normal PSCs

The smooth surface, in other words, no particles residual on the surface of samples, has been studied via controlling the type of  $TiO_2$  ETL solution, the concentration of  $TiO_2$  ETL solution, and spin speed. For the first time, the Ti-Nanoxide T600/SC material for deposition of  $Mp-TiO_2$  is better than the Ti-Nanoxide T300/SC material because it can decrease particles on the surface of the sample as shown in figure 43(above) The thickness of using Ti-Nanoxide T600/SC material as  $Mp-TiO_2$  is 396 nm, which is thicker than using Ti-Nanoxide T300/SC material (188 nm) as shown in figure 43(below). The J-V curves of both materials are shown in figure 44.

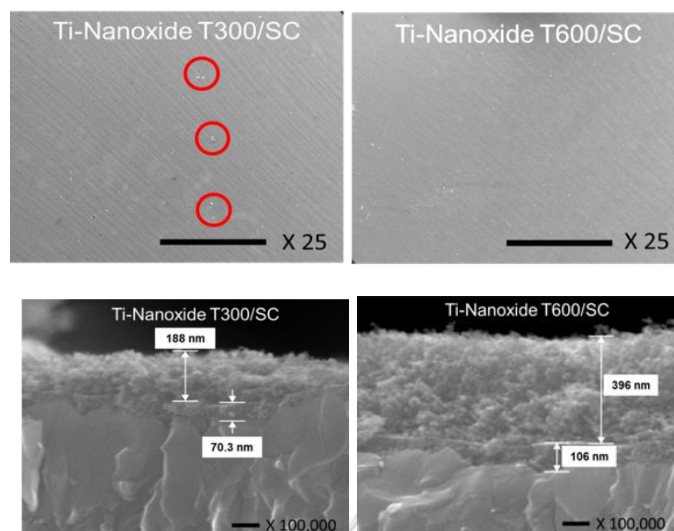


Figure 43. Surface (above) and cross-section (below) image of Ti-Nanoxide T600/SC and Ti-Nanoxide T300/SC under spin speed 5000 rpm for 30s.

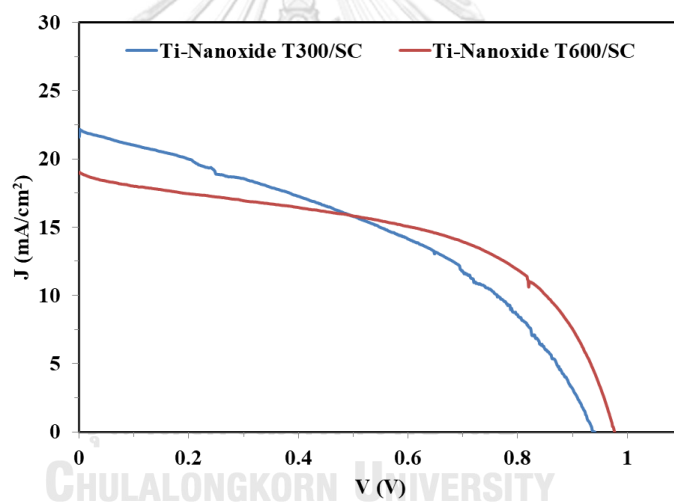


Figure 44. J-V characteristics of normal perovskite device with Ti-Nanoxide T600/SC (red line) and Ti-Nanoxide T300/SC (blue line).

However, the particle's residuals still occurred on the surface of the samples, and the J-V measurement results showed low fill factor (FF) and low open-circuit voltage ( $V_{oc}$ ). The 30NR-D Titania Paste, as another type of Mp-TiO<sub>2</sub> solution, is chosen to increase high density and completely cover the surface of samples without particles. To control thickness, different precursor solutions of Mp-TiO<sub>2</sub>: Ethanol are varied to 1:4 (is M4), 1:5 (is M5), and 1:7 (is M7) v/v. The solutions are deposited on Cp-TiO<sub>2</sub>/FTO at a spin speed of 5000 rpm for 30 s. The thickness of Mp-TiO<sub>2</sub> from each condition is demonstrated with the SEM technique in figure 45. The thickness of Mp-TiO<sub>2</sub> decreases as the control of ethanol increases, which can be great for PSCs because thinner ETL might better facilitate carrier to the contact (FTO). This is

consistent with the J-V measurements. Figure 46 shows the PSCs with different Mp-TiO<sub>2</sub> precursor ratios. The best PCE of 9.5% is obtained from 1:7 v/v.

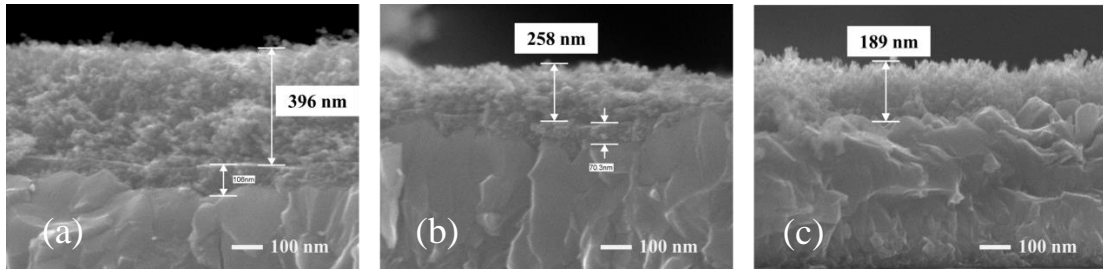


Figure 45. Cross-section images of different precursor solutions, Mp-TiO<sub>2</sub>: Ethanol, (a) 1: 4 (M4), (b) 1: 5 (M5), and (c) 1: 7 (M7) v/v.

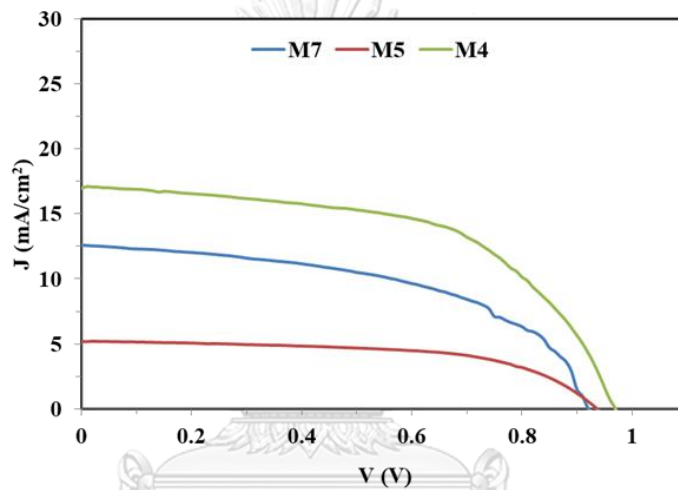


Figure 46. J-V curve of different precursor solutions, Mp-TiO<sub>2</sub>: Ethanol, (a) 1: 4 (M4), (b) 1: 5 (M5), and (c) 1: 7 (M7) v/v.

Table 5. All photovoltaic parameters of different precursor solutions, Mp-TiO<sub>2</sub>: Ethanol, 1: 4 (M4), 1: 5 (M5), and 1: 7 (M7) v/v, on the inverted device.

Condition	J <sub>sc</sub> (mA/cm <sup>2</sup> )	V <sub>oc</sub> (v)	FF (%)	PCE (%)
M4 5000 rpm for 30 s /Cp-TiO <sub>2</sub>	16.11	0.95	61.29	9.38
M5 5000 rpm for 30 s /Cp-TiO <sub>2</sub>	16.11	1.03	57.48	9.53
M7 5000 rpm for 30 s /Cp-TiO <sub>2</sub>	12.78	0.94	49.65	5.97

Moreover, increasing PCE via using a suitable uniform and dense Mp-TiO<sub>2</sub> layer as ETL on PSCs is analyzed. The Mp-TiO<sub>2</sub> layer has been varied at spin speeds

of 3000, 4000, and 5000 rpm to vary the thickness. The J-V curve of different spin speeds of different Mp-TiO<sub>2</sub> solutions is revealed in figure 50.

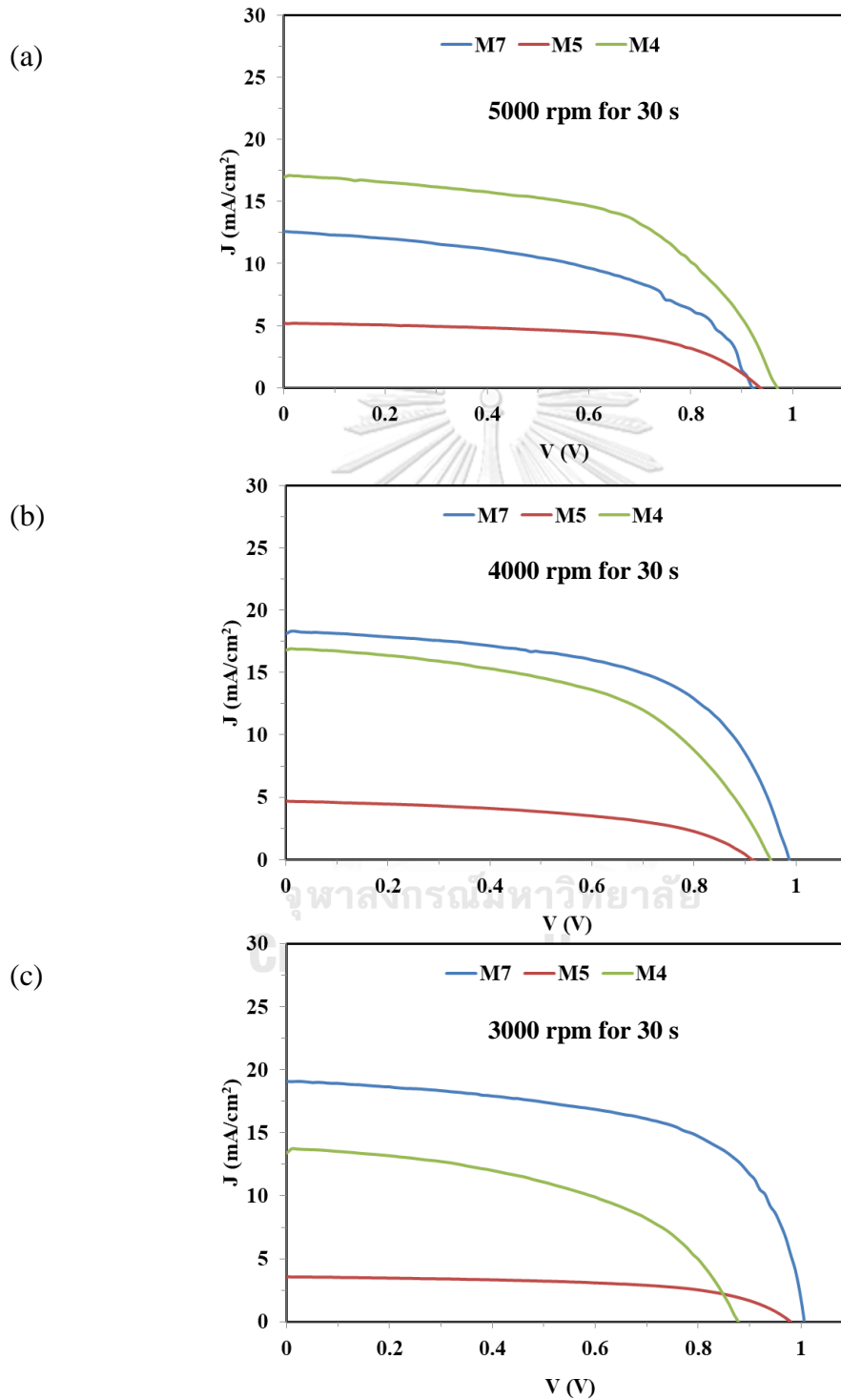


Figure 47. J-V curve of various spin speeds at (a) 5000, (b) 4000, (c) 3000 rpm for 30 s with M4, M5 and M7, respectively.



As a result, deposition of the Mp-TiO<sub>2</sub> layer at 3000 rpm with M7 results is advantageous for a higher FF and a higher PCE. All photovoltaic parameters are summarized in Table 6.

*Table 6. Photovoltaic parameters of different Mp-TiO<sub>2</sub> dilutions, such as M4, M5, and M7, with spin speeds of 5000, 4000, and 3000 rpm for 30 sec.*

Condition	J <sub>sc</sub> (mA/cm <sup>2</sup> )	V <sub>oc</sub> (v)	FF (%)	PCE (%)
M4 5000 rpm for 30 s /Cp-TiO <sub>2</sub>	16.11	0.95	61.29	9.38
M5 5000 rpm for 30 s /Cp-TiO <sub>2</sub>	16.11	1.03	57.48	9.53
M7 5000 rpm for 30 s /Cp-TiO <sub>2</sub>	12.78	0.94	49.65	5.97
M4 4000 rpm for 30 s /Cp-TiO <sub>2</sub>	17.62	0.92	49.67	8.05
M5 4000 rpm for 30 s /Cp-TiO <sub>2</sub>	16.79	0.98	54.86	9.02
M7 4000 rpm for 30 s /Cp-TiO <sub>2</sub>	23.63	0.90	48.75	10.39
M4 3000 rpm for 30 s /Cp-TiO <sub>2</sub>	13.40	0.88	50.42	5.95
M5 3000 rpm for 30 s /Cp-TiO <sub>2</sub>	15.48	0.90	50.22	6.99
M7 3000 rpm for 30 s /Cp-TiO <sub>2</sub>	16.07	1.02	60.26	10.88

### 5.1.2 Dissolved PbI<sub>2</sub> with different solvents

In this step, the perovskite layer is formed with two precursors between PbI<sub>2</sub> as the first precursor, and the second precursor is methylammonium iodide (MAI or CH<sub>3</sub>NH<sub>3</sub>I), which are coated on the TiO<sub>2</sub> layer, respectively. The PbI<sub>2</sub> with different solvent in MAPbI<sub>3</sub>(CH<sub>3</sub>NH<sub>3</sub>PbI<sub>3</sub>), the different solvents to dissolve PbI<sub>2</sub> are studied; pure dimethylformamide (DMF), and mixtures of DMF and DMSO (N, N-Dimethylsulfoxide) with the ratios of (4:1) and (1:4).

In this work, both a 50 nm thick Cp-TiO<sub>2</sub> layer and a 300 nm thick Mp-TiO<sub>2</sub> are deposited on the FTO surface substrate with spin coating at 3000 rpm for 30 s and then baked at 500 °C for 30 min. The 400 nm thick perovskite films were formed with a combination of PbI<sub>2</sub> film (0.461 g of PbI<sub>2</sub>/1 ml of DMF (N,N-Dimethylformamide) and DMSO (N,N-Dimethylsulfoxide) with three different solvents of pure dimethylformamide (DMF), and mixtures of DMF: DMSO with the ratios of (4:1) and

(1:4) and methyammonium iodide (MAI) solution (0.010 g MAI/1 ml IPA). The  $\text{PbI}_2$  solution is stirred on a hot plate at 70 °C for 12 hours while the MAI solution is stirred at room temperature. They are kept in the glovebox at a humidity (RH) of less than 30%.  $\text{PbI}_2$  as the first precursor, which is coated above the electron transport layer (ETL) at spin speed of 3000 rpm for 30 s, and then residual solvent in  $\text{PbI}_2$  is removed on a hot plate at 70 °C for 20 min. The second precursor solution is the MAI solution that is deposited over the  $\text{PbI}_2$  surface twice at spin speed of 2000 rpm for 20 s, and each spin MAI solution is holed on the  $\text{PbI}_2$  film for 30 s (called loading time for 30 s). During the second spin off of MAI, anti-solvent is applied and then it is annealed at 120 °C for 15 min. The top of the perovskite film is coated with a 150 nm thick spiro-OMeTAD hole transport layer (HTL) by spin-coating at 3000 rpm for 30 s. All samples are kept in the dry box for 12 hours before the 80-100 nm thick Au contact is thermally evaporated on HTL. Spiro-OMeTAD solution is mixed from 0.0723 g of spiro-OMeTAD powder in 1 ml CB and 28.8  $\mu\text{l}$  of 4-tert-butylpyridine (t-BP) and then added with 0.520 g of lithium bistrifluoromethanesulfonimide (Li-TFSI) salt in 1 ml of acetonitrile.

#### *Results and discussions of dissolved $\text{PbI}_2$ with different solvents*

The current density-voltage characterization of all samples is indicated in figure 48, and all photovoltaic parameters are summarized in Table 7.

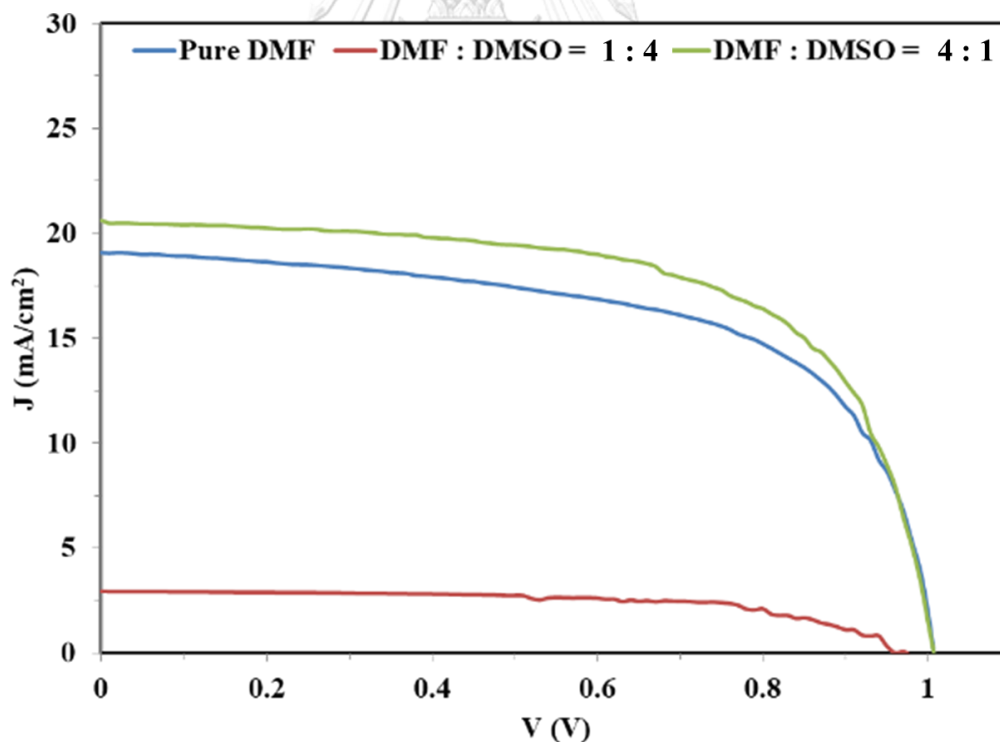


*Figure 48. The J-V characteristics under illumination of the perovskite solar cells are indicated in the legend.*

*Table 7. Summary of the photovoltaic parameters derived from J-V measurements along with activation energy for using pure DMF, DMF and DMSO in a 1:4 ratio, and DMF and DMSO in a 4:1 ratio (showing the best performance).*

Parameters	Pure DMF	DMF:DMSO = 1 : 4	DMF:DMSO = 4 : 1
V <sub>oc</sub> (V)	1.0	0.9	1.0
J <sub>sc</sub> (mA/sq.cm.)	16.1	23.3	20.6
Fill Factor (%)	60.3	45.1	63.0
PCE (%)	10.9	9.3	13.12

The results indicate that the suitable solvent for PbI<sub>2</sub> is a ratio of DMSO and DMF of 4:1, which leads to an improved performance of the perovskite device. The maximum PCE of 11.9% was achieved for the cell prepared by using the solvent in a 4:1 ratio for DMF:DMSO.

### 5.1.3 An anti-solvent

An anti-solvent is a solvent in which the compound is less soluble and used to wash another solvent [77]. Both chlorobenzene (CB) and toluene (TO) are used as the anti-solvents during the growth of the perovskite films. The anti-solvent is applied to improve the morphology, grain size of the perovskite films and efficiency of the solar devices.

In this section, a 50 nm thick Cp-TiO<sub>2</sub> layer and a 300 nm thick Mp-TiO<sub>2</sub> layer are deposited on the FTO surface substrate using spin coating at 3000 rpm for 30 s and then baked at 500 °C for 30 minutes. PbI<sub>2</sub> film (0.461 g of PbI<sub>2</sub>/1 ml of DMF (N,N-Dimethylformamide) and DMSO (N,N-Dimethylsulfoxide) in a 4:1 ratio) and methylammonium iodide (MAI) solution (0.010 g MAI/1 ml IPA) were used to create the 400 nm thick perovskite films. The PbI<sub>2</sub> solution is stirred on a hot plate at 70 °C for 12 hours while the MAI solution is stirred at room temperature. They are kept in the glovebox at a relative humidity (RH) of less than 30%. The PbI<sub>2</sub> solution plays as the first precursor is covered above the electron transport layer (ETL) at a spin speed of 3000 rpm for 30 s and then residual solvent is removed on a hot plate at 70 °C for 20 min. The second precursor solution is the MAI solution that is deposited over the PbI<sub>2</sub> surface twice at a spin speed of 2000 rpm for 20 s, and each spin MAI solution is held on the PbI<sub>2</sub> film for 30 s (called loading time for 30 s). During the second spin off of MAI, anti-solvent is applied and then it is annealed at 120 °C for 15 min. The top of the perovskite film is coated with a 150 nm thick spiro-OMeTAD hole transport layer (HTL) by spin-coating at 3000 rpm for 30 s. All samples are kept in the dry box for 12 hours before the 80-100 nm thick Au contact is thermally evaporated on HTL. Then 0.0723 g of spiro-OMeTAD powder is mixed in 1 ml of CB and 28.8 l of 4-tert-butylpyridine (t-BP), and then 0.520 g of lithium bistrifluoromethanesulfonimide (Li-TFSI) salt is mixed in 1 ml of acetonitrile. In this work, researcher studied the types, the amounts, and the beginning times of chlorobenzene (CB) or toluene (TO) anti-solvents under investigation. After spinning the MAI solution, the amount of anti-solvents is varied from 25 to 150 µl, and the elapsed time is varied from 5 to 15 seconds.

### Results and discussions of an anti-solvent

Figure 49 shows the cross-section images and surface morphology of different perovskite layers (without anti-solvent, with the addition of CB, and with the addition of TO) by using a field-mission scanning electron microscope (FESEM; JEOL Model JSM-7001F). The surface morphology shows the addition of an anti-solvent can improve the grain growth of perovskite film compared to one without an anti-solvent. In addition, no pin-hole on perovskite films with anti-solvent is observed. So, the anti-solvents aid in increasing the growth of the perovskite thin films and improving the morphology of the surface. The cross-section images show no significant difference between the applications of CB and TO anti-solvents.

Figure 50 shows the morphologies of perovskite films (a)-(c) for CB at 5, 10, and 15 s after spinning MAI solution, and (d)-(f) for TO at 5, 10, and 15 s after spinning MAI solution, respectively. Figure 50 (a) depicts the grain size of perovskite films with CB anti-solvent applied at 5 s after the application of MAI solution, which is larger than for both CB and TO anti-solvents under other conditions.

A spectrophotometer (Shimadzu Model UVPC1600) is used to investigate the absorbance of the perovskite layer, which is in the range of 400-1000 nm. In figure 51, both CB and TO anti-solvents are independent of the type or amount of anti-solvent applied due to all of them showing the similar photon absorption threshold around 770–780 nm.

Photovoltaic parameters such as open-circuit voltage ( $V_{oc}$ ), short-circuit current density ( $J_{sc}$ ), fill factor (FF), and PCE were measured under AM1.5. Both forward (f) and reverse (r) directions between -0.1 and 1.2 V of bias voltage are determined by using the J-V measurements in the section of the active cell areas of the device under investigation, which are 0.06 and 0.2 cm<sup>2</sup> with the box chart. Both forward (f) and reverse (r) directions of PSCs with small active cell areas of 0.06 cm<sup>2</sup> are presented in figure 52(a) - (c) for PSCs with different amounts of CB anti-solvent at 5, 10, and 15 s after spinning the MAI solution, respectively, whereas (d) - (f) for PSCs with different amounts of TO anti-solvent at 5, 10, and 15 s after spinning the MAI solution. The best set PCE of 16.8% is obtained from 50  $\mu$ l of CB applied at 5 s elapsed time after spinning the MAI solution. Table 8 shows all average solar cell parameters from using CB anti-solvents on PSCs are better than those using TO anti-solvent for both active cell areas [78].

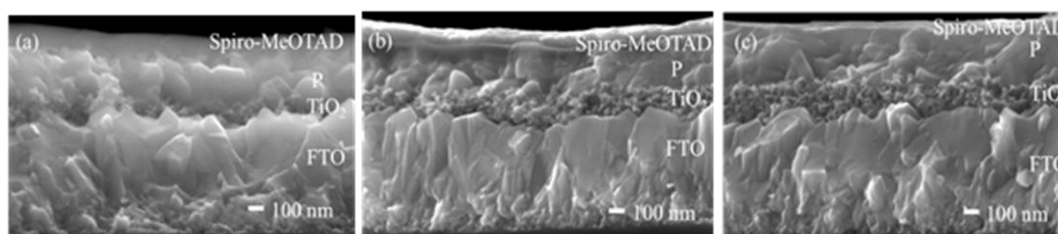


Figure 49. Cross-section SEM (scale bar = 100 nm) images of perovskite film (P); for (a) without anti-solvent, (b) with addition of CB and (c) with addition of TO, as the anti-solvents.

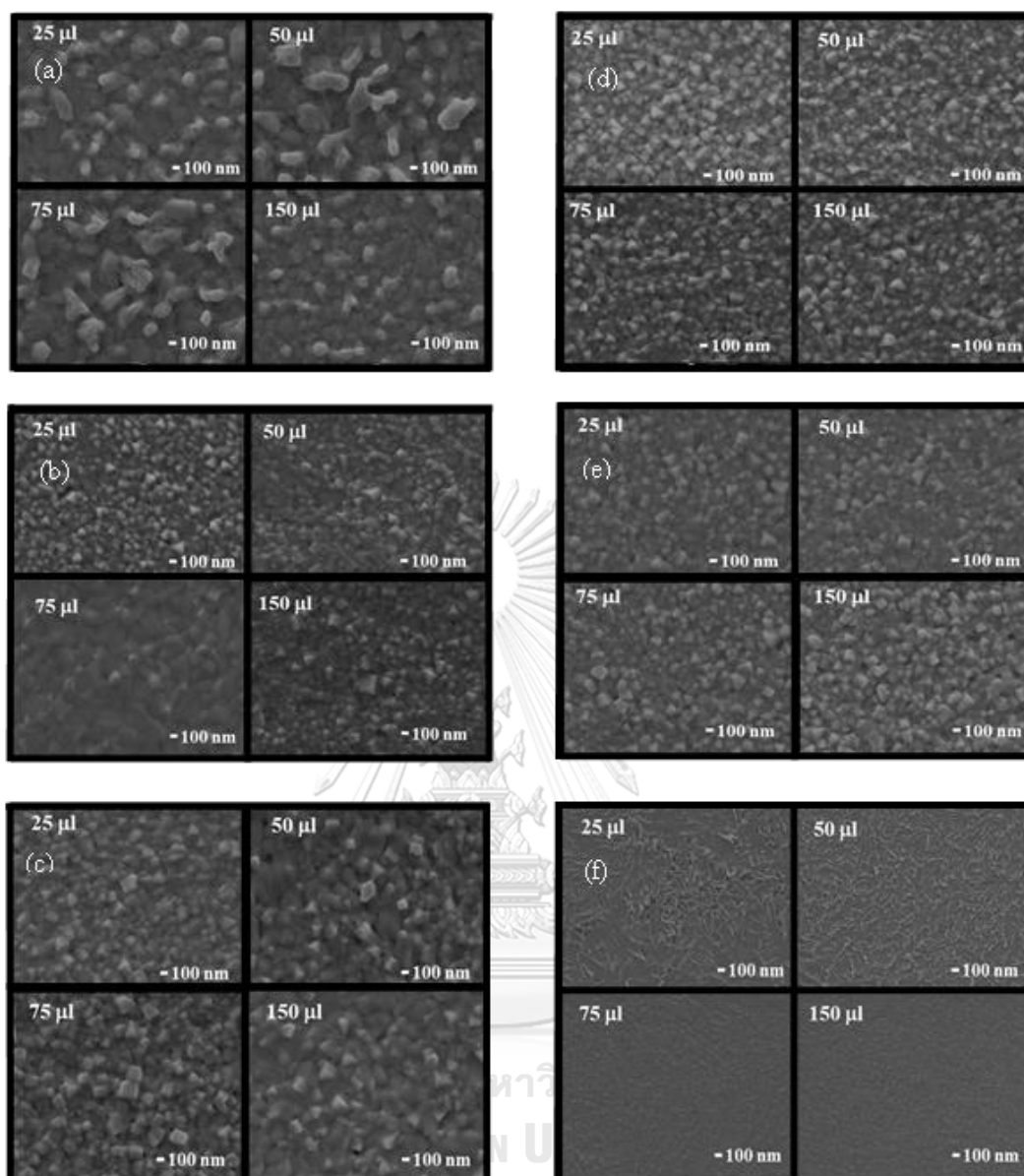


Figure 50. Top-view SEM images of perovskite film with the application of CB anti-solvent at (a) 5 s, (b) 10 s and (c) 15 s; TO anti-solvent at (d) 5 s, (e) 10 s and (f) 15 s after spinning the 2<sup>nd</sup> layer of MAI solution.

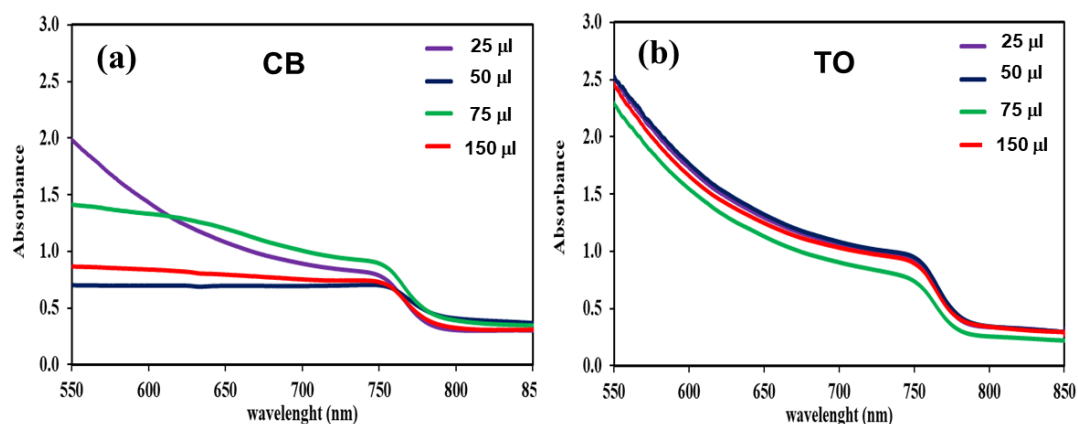


Figure 51. Optical absorption of perovskite absorber films vs. wavelength for various volume of (a) CB and (b) TO.

Table 8. Device performances of the inverted perovskite cells using different anti-solvents.

Solar cell parameters	with CB anti-solvent		with TO anti-solvent	
	cell area = 0.06 cm <sup>2</sup>	cell area = 0.2 cm <sup>2</sup>	cell area = 0.06 cm <sup>2</sup>	cell area = 0.2 cm <sup>2</sup>
V <sub>oc</sub> (V)	1.07 ± 0.01	0.98 ± 0.03	1.04 ± 0.02	1.0 ± 0.1
J <sub>sc</sub> (mA/cm <sup>2</sup> )	22.70 ± 0.8	16.49 ± 1.1	20.27 ± 0.9	17.8 ± 0.6
FF (%)	69.90 ± 1.3	65.00 ± 0.9	61.29 ± 2.3	51.60 ± 7.3
PCE (%)	15.9 ± 0.7	10.47 ± 1.3	13.02 ± 0.9	9.09 ± 2.0

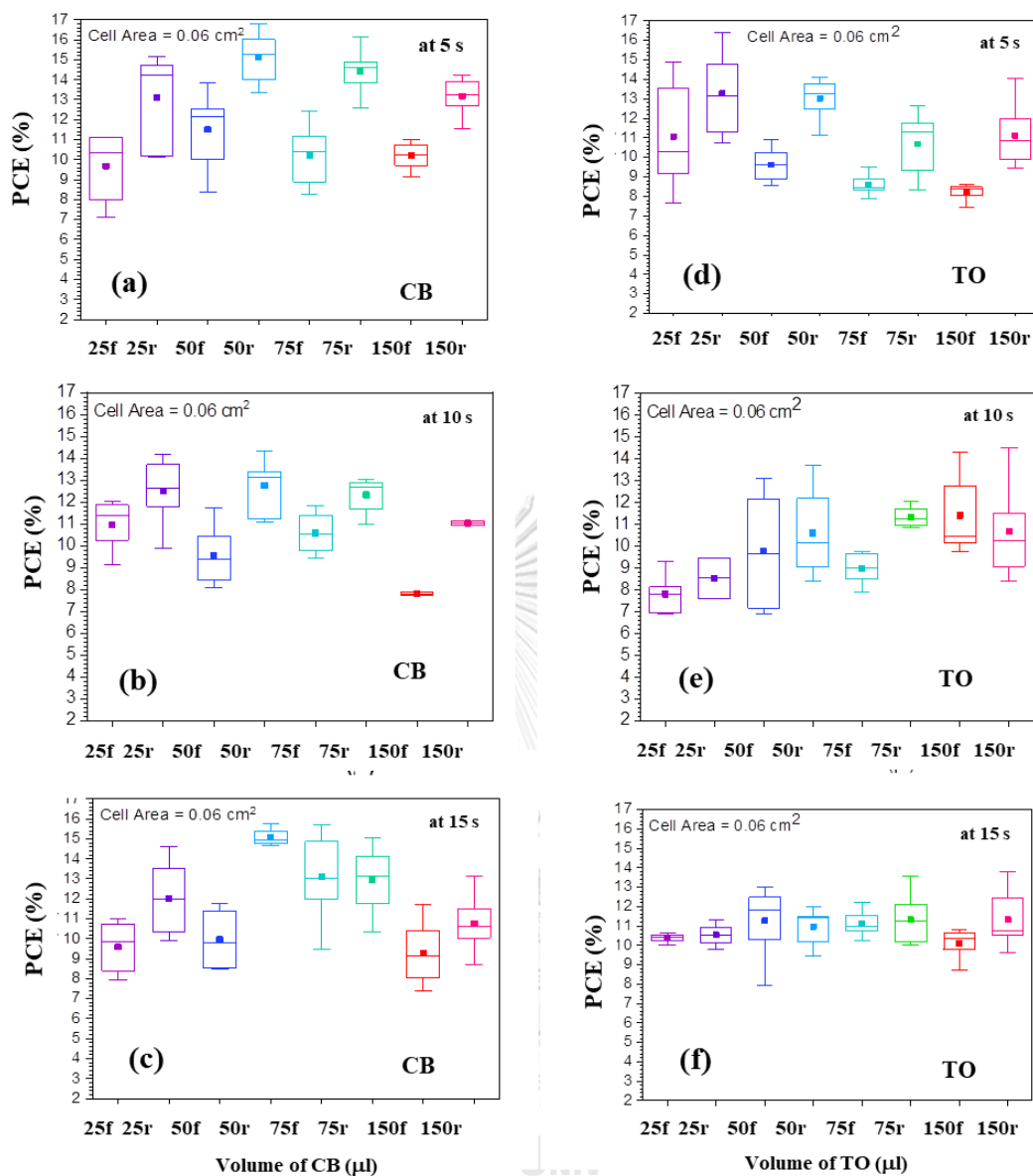


Figure 52. Box chart plots of PCE of PSCs vs. volume of CB and TO anti-solvents for small active area of  $0.06 \text{ cm}^2$ , which forward and reverse direction of J-V measurement refer to f and r, respectively.

## 5.2 Inverted structure PSCs

### 5.2.1 HTM options

The hole transport materials (HTMs) are one of the key compounds in perovskite solar cells (PSCs) for the p-i-n structured perovskite solar cells (PSCs). Nickel oxide ( $\text{NiO}_x$ ), PEDOT: PSS, PTAA are chosen as HTM [79]. They can affect the performance of PSCs. In addition, the morphology of the underlying hole transport layer (HTL) in PSCs plays a crucial role in determining the optoelectronic quality of the active perovskite absorber layer [80].

#### 5.2.1.1 Concentration and thickness of $\text{NiO}_x$

Nickel oxide ( $\text{NiO}_x$ ), as a p-type metal oxide, is used as a hole transporting layer (HTL). It is widely studied for the inverted perovskite device. In this work,  $\text{NiO}_x$  HTLs in PSCs will be discussed to get probable solutions to enhance development in power conversion efficiency (PCE) as well as stable  $\text{NiO}_x$ -based PSCs. The advantages of  $\text{NiO}_x$  are that it can promote charge transport, separation of electron-hole pairs and decrease the charge recombination [81].

A  $\text{NiO}_x$  HTLs is spin coated on the FTO surface substrate with different concentration between 0.5 M (0.145 g of  $\text{NiO}_x$  powder in 0.933  $\mu\text{l}$  of ethylene glycol and 0.067  $\mu\text{l}$  ethylenediamine) and 1 M (0.290 g of  $\text{NiO}_x$  powder in 0.933  $\mu\text{l}$  of ethylene glycol and 0.067  $\mu\text{l}$  ethylenediamine) and varied spin speed from 4000, 5000, 6000, 7000 and 8000 rpm for 30 s and then baked at high temperature sinter 300 °C for 60 min. The 400 nm thick perovskite film was formed with combination of  $\text{PbI}_2$  film (0.461 g of  $\text{PbI}_2$ /1 ml of DMF (N,N-Dimethylformamide) and DMSO (N,N-Dimethylsulfoxide) with 4:1 ratio) and methyammonium iodide (MAI) solution (0.010 g MAI/1ml IPA). The  $\text{PbI}_2$  solution is stirred on a hot plate at 70 °C for 12 hours while the MAI solution is stirred at room temperature. They are kept in the glovebox under relative humidity (RH) of less than 30%. The  $\text{PbI}_2$  solution plays as the first precursor is covered above the electron transport layer (ETL) at spin speed of 3000 rpm for 30 s and then residual solvent is removed on a hot plate at 70 °C for 20 min. The second precursor solution is the MAI solution that is deposited over the  $\text{PbI}_2$  surface twice at spin speed of 2000 rpm for 20 s and each spin MAI solution is holded on the  $\text{PbI}_2$  film for 30 s (called loading time for 30 s). During the second spin-off of MAI, 50  $\mu\text{l}$  of CB is applied at 5 s elapsed time after spinning the MAI solution and then is annealed at 120 °C for 15 min. The above perovskite film is coated with a 150 nm thick phenyl-C61-butyric acid methyl ester ( $\text{PC}_{61}\text{BM}$ ) as an electron transport layer (ETL) by spin-coating at 3000 rpm for 30 s. All samples are deposited with 80-100 nm thick Au contact by thermal evaporation on HTLs. The  $\text{PC}_{61}\text{BM}$  solution is mixed with 0.02 g of  $\text{PC}_{61}\text{BM}$  powder in 1 ml of chlorobenzene (CB).

#### *Results and discussions of concentration and thickness of $\text{NiO}_x$*

Figures 53 and 54 illustrate the surface morphology and optical transparency of  $\text{NiO}_x$ /FTO with different spin speeds repeatedly. The surface and the transmission of the samples are quite similar. Their energy band gap ( $E_g$ ) of  $\text{NiO}_x$  is 3.5 eV, which is calculated from the knee of transmission graphs at 354 nm.



In addition, figure 55 displays the J-V curve of all conditions of both 0.5 M and 1 M of  $\text{NiO}_x$ , with the spin speed of 5000, 6000, 7000, and 8000 rpm for 30 s, respectively.

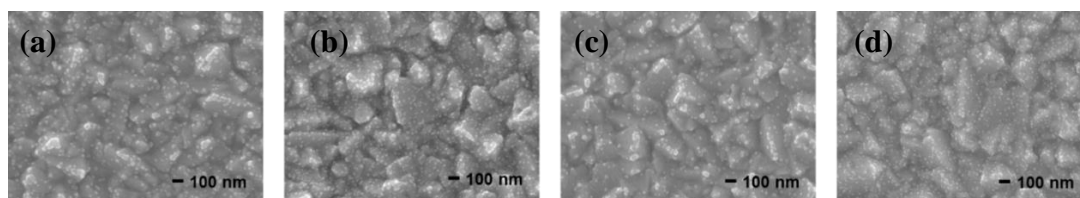


Figure 53. Surface SEM images of 1 M  $\text{NiO}_x$ -covered FTO glass at spin speeds of (a) 5000, (b) 6000, (c) 7000, and (d) 8000 rpm.

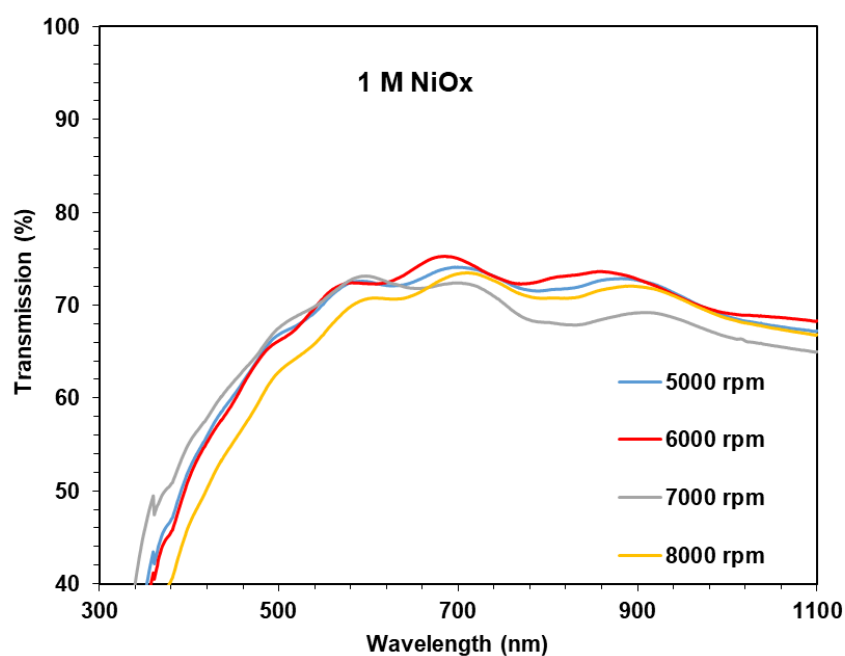


Figure 54. Optical transmission of 1 M  $\text{NiO}_x$  covered FTO glass at spin speeds of 5000 (blue line), 6000 (red line), 7000 (violet line) and 8000 (orange line).

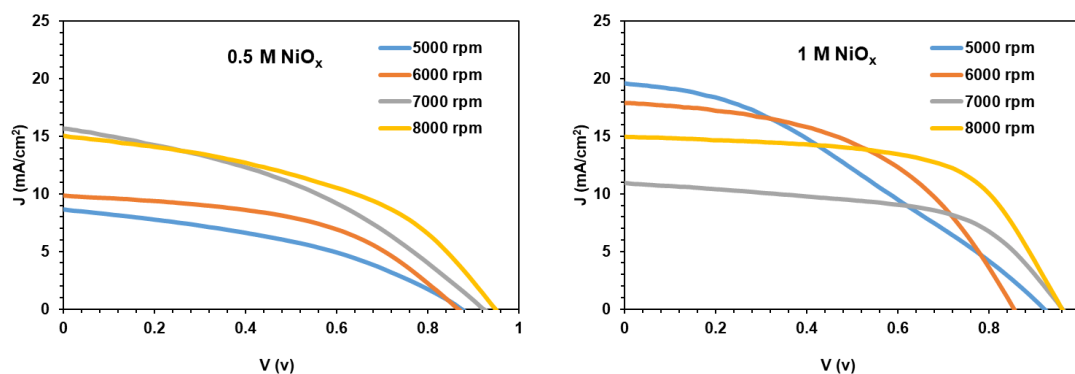


Figure 55. J-V characteristics of the inverted perovskite device with a concentration of 0.5 M (left) and 1 M NiO<sub>x</sub> (right) by using different spin speed between 5000, 6000, 7000, and 8000 rpm for 30 s, respectively.

Table 9. All photovoltaic parameters result by the J-V measurement.

Photovoltaic parameters (active area 0.06 cm <sup>2</sup> )	0.5 M NiO <sub>x</sub>				1 M NiO <sub>x</sub>			
	5000 rpm	6000 rpm	7000 rpm	8000 rpm	5000 rpm	6000 rpm	7000 rpm	8000 rpm
V <sub>oc</sub> (V)	0.9	0.9	0.9	0.9	0.9	0.9	0.8	0.9
J <sub>sc</sub> (mA/cm <sup>2</sup> )	15.7	15.6	15.1	12.7	19.7	10.9	17.9	15.0
FF (%)	41.7	38.6	47.0	44.6	33.8	56.0	48.8	61.2
PCE (%)	5.5	5.6	6.6	6.4	6.1	5.9	7.5	8.8

According to the table 9, V<sub>oc</sub> increase, as the spin speed of both concentrations increase, resulting in a higher PCE of the device. In addition, as the spin speed decrease, which deteriorates the performance of the device. Therefore, an optimal PCE of 8.8% and FF of 61.2% were obtained on the device by using the concentration of 1 M NiO<sub>x</sub> on the device at spin speed at 8000 rpm for 30 s.

#### 5.2.1.2 Different products of PEDOT: PSS

Poly (3,4-ethylene dioxythiophene): poly (styrenesulfonate) (PEDOT: PSS) as the hole transport layer (HTL) in polymer p-i-n structured perovskite solar cells (PSCs). In this work, PEDOT: PSS was chosen to improve fill factor (FF) and increase higher power conversion efficiency (PCE), because it has better conductivity than using NiO<sub>x</sub> as HTL[82]. Also, PEDOT:PSS has good film forming ability, high transparency, and good stability in air [83, 84]. Three products of PEDOT:PSS, which are Al 4083, PH 1000, and HTL solar 3 [85, 86], have been used as an alternative hole selective contact on the inverted devices.

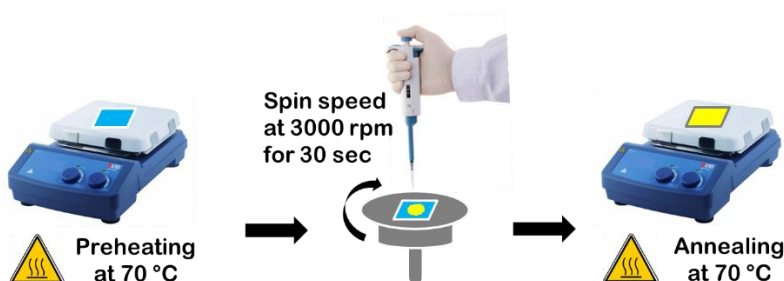
A PEDOT:PSS HTL is coated on the FTO substrate by spin-coating at 5000 and 6000 rpm for 30 s with all types of PEDOT:PSS, and then heated on a hotplate at

180 °C for 15 min. The 400 nm thick perovskite film was formed with a combination of  $\text{PbI}_2$  film (0.461 g of  $\text{PbI}_2$ /1 ml of DMF (N,N-Dimethylformamide) and DMSO (N,N-Dimethylsulfoxide) with a 4:1 ratio) and methyamonium iodide (MAI) solution (0.010 g MAI/1ml IPA). The  $\text{PbI}_2$  solution is stirred on a hot plate at 70 °C for 12 hours while the MAI solution is stirred at room temperature. They are kept in the glovebox at a relative humidity (RH) of less than 30%. The  $\text{PbI}_2$  solution plays as the first precursor is covered above the electron transport layer (ETL) at a spin speed of 3000 rpm for 30 s and then residual solvent is removed on a hot plate at 70 °C for 20 min. The second precursor solution is the MAI solution that is deposited over the  $\text{PbI}_2$  surface twice at a spin speed of 2000 rpm for 20 s, and each spin MAI solution is holed on the  $\text{PbI}_2$  film for 30 s (called loading time for 30 s). During the second spin-off of MAI, 50  $\mu\text{l}$  of CB is applied at 5 s elapsed time after spinning the MAI solution and then is annealed at 120 °C for 10 min. The above perovskite film is coated with a 150 nm thick phenyl-C61-butyric acid methyl ester ( $\text{PC}_{61}\text{BM}$ ) as an electron transport layer (ETL) by spin-coating at 1500 rpm for 40 s and then followed by BCP (0.0005 g/ml in IPA, stirred overnight) at 4000 rpm for 30 s. All samples are deposited with 80–100 nm thick Au contact by thermal evaporation on HTLs. The  $\text{PC}_{61}\text{BM}$  solution is mixed with 0.02 g of  $\text{PC}_{61}\text{BM}$  powder in 1 ml of chlorobenzene (CB). Above, all the steps are shown in figure 56.

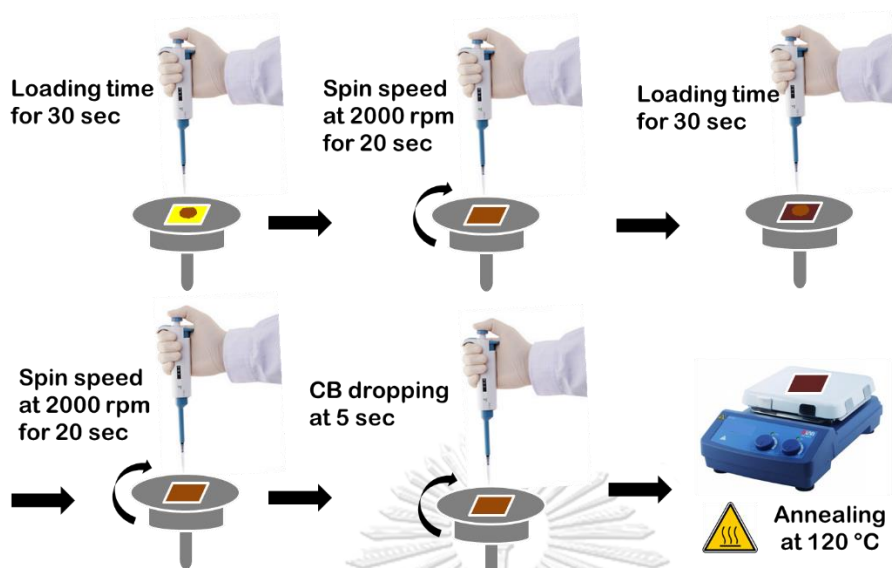
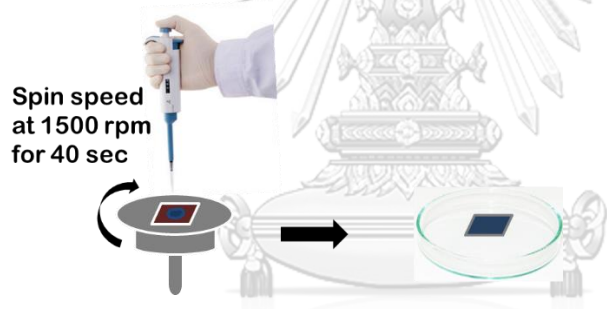
(a) PEDOT: PSS film



(b)  $\text{PbI}_2$  film



## (c) MAI film

(d) PC<sub>61</sub>BM film

## (E) BCP film

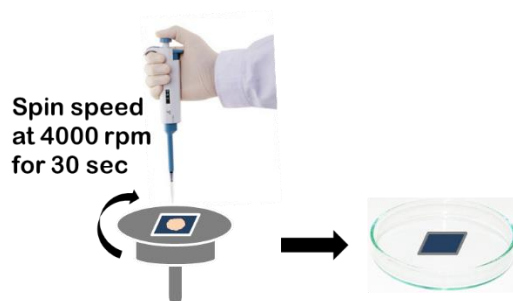


Figure 56. Fabrication of inverted perovskite device processes; (a) PEDOT:PSS film, (b) PbI<sub>2</sub> film, (c) MAI film, (d) PC<sub>61</sub>BM film, and (e) BCP film.

*Results and discussions of different products of PEDOT: PSS*

Table 10, which displays all the photovoltaic parameters of each condition. The best PCE of 12% is obtained when using HTL solar 3 at spin speed of 6000 rpm for 30 s as seen in the violet line in figure 57.

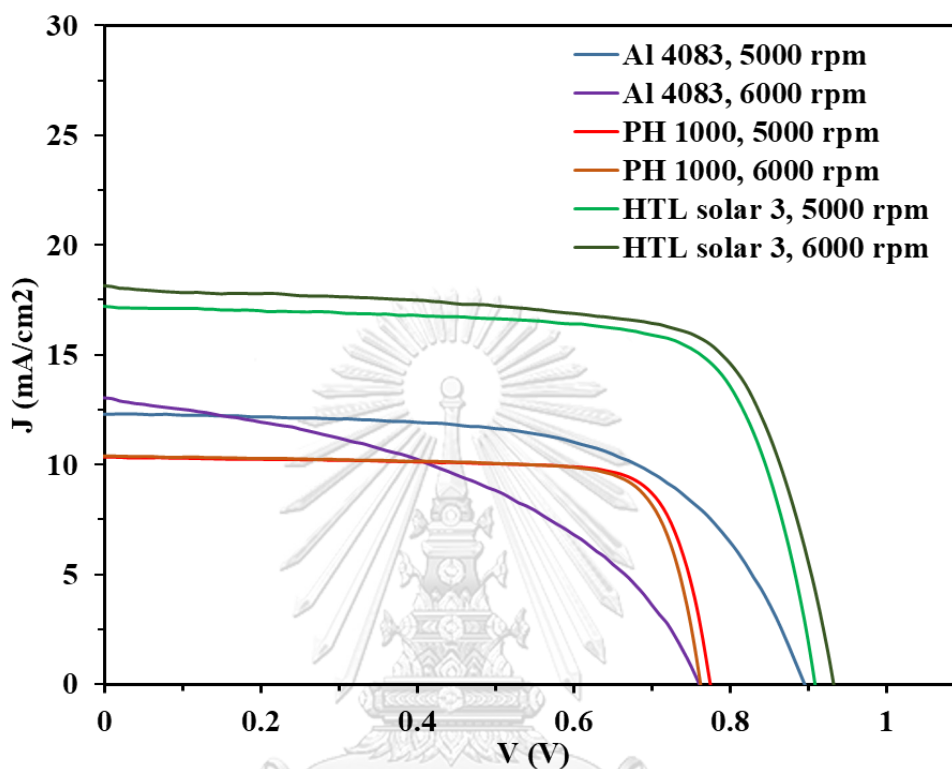


Figure 57. The J-V curve of all types of PEDOT:PSS such as Al 4083, PH 1000, and HTL solar 3 with different spin speeds between 5000 and 6000 rpm for 30 s.

Table 10. All photovoltaic parameters result by the J-V measurement.

Photovoltaic parameters (active area 0.06 cm <sup>2</sup> )	Al 4083		PH 1000		HTL solar 3	
	5000 rpm	6000 rpm	5000 rpm	6000 rpm	5000 rpm	6000 rpm
V <sub>oc</sub> (V)	0.9	0.7	0.8	0.8	0.9	0.9
J <sub>sc</sub> (mA/cm <sup>2</sup> )	12.3	11.2	10.4	10.4	12.3	18.1
FF (%)	61.9	71.7	79.5	78.9	72.8	71.3
PCE (%)	6.9	5.9	6.4	6.3	7.9	12.0

### 5.2.1.3 Suitable condition for PTAA

Due to the low conductivity of NiO<sub>x</sub> and PEDOT:PSS, charge transport is limited and inefficient [87]. To solve this problem, the PTAA was also used for the HTL, which could be used to enhance potential up to 1.1 V, improve the carrier mobility, and increase the higher performance of the PSCs [88]. PTAA can be annealed at a low temperature and dissolved in the solvent as well as be stable in ambient conditions [89].

A PTAA is deposited on the FTO surface substrate by spin-coating at 2000 and 3000 rpm for 30 s and then baked on a hotplate at 105 °C for 10 min. PTAA solution is prepared by mixing 0.007 g of PTAA powder in 1 ml of CB and 0.1 µl of 4-tert-butylpyridine (t-BP) and then adding 0.170 g of lithium bistrifluoromethanesulfonimide (Li-TFSI) salt in 1 ml of acetonitrile. PbI<sub>2</sub> film (0.461 g of PbI<sub>2</sub>/1 ml of DMF (N,N-Dimethylformamide) and DMSO (N,N-Dimethylsulfoxide) with a 4:1 ratio) and methyammonium iodide (MAI) solution (0.010 g MAI/1 ml IPA) were used to form the 400 nm thick perovskite films. The PbI<sub>2</sub> solution is stirred on a hot plate at 70 °C for 12 hours while the MAI solution is stirred at room temperature. They are kept in the glovebox at a relative humidity (RH) of less than 30%. The PbI<sub>2</sub> solution plays as the first precursor is covered above the electron transport layer (ETL) at spin speed of 3000 rpm for 30 s and then residual solvent is removed on a hot plate at 70 °C for 20 min. The second precursor solution is the MAI solution that is deposited over the PbI<sub>2</sub> surface twice at spin speed of 2000 rpm for 20 s, and each spin MAI solution is holded on the PbI<sub>2</sub> film for 30 s (called loading time for 30 s). During the second spin-off of MAI, 50 µl of CB is applied at 5 s elapsed time after spinning the MAI solution and then is annealed at 120 °C for 10 min. The above perovskite film is coated with a 150 nm thick phenyl-C61-butyric acid methyl ester (PC<sub>61</sub>BM) as an electron transport layer (ETL) by spin-coating at 1500 rpm for 40 s. Then BCP is coated onto the PC<sub>61</sub>BM surface at a spin speed of 4000 rpm for 30 s. All samples are deposited with a 120 nm thick Au contact by thermal evaporation on HTLs. The PC<sub>61</sub>BM solution is mixed with 0.02 g of PC<sub>61</sub>BM powder in 1 ml of chlorobenzene (CB).

### *Results and discussions of suitable condition for PTAA*

Figure 58 shows that the PCE of 13% and 15% are obtained by using PTAA as the HTL. The spin speed is 2000 and 3000 rpm, respectively. Additionally, the high improvement of PCE was observed. The PCE of PTAA-based devices is significantly better than that of NiO<sub>x</sub> and PEDOT:PSS base devices. A summary of all photovoltaic parameters is shown in Table 11.

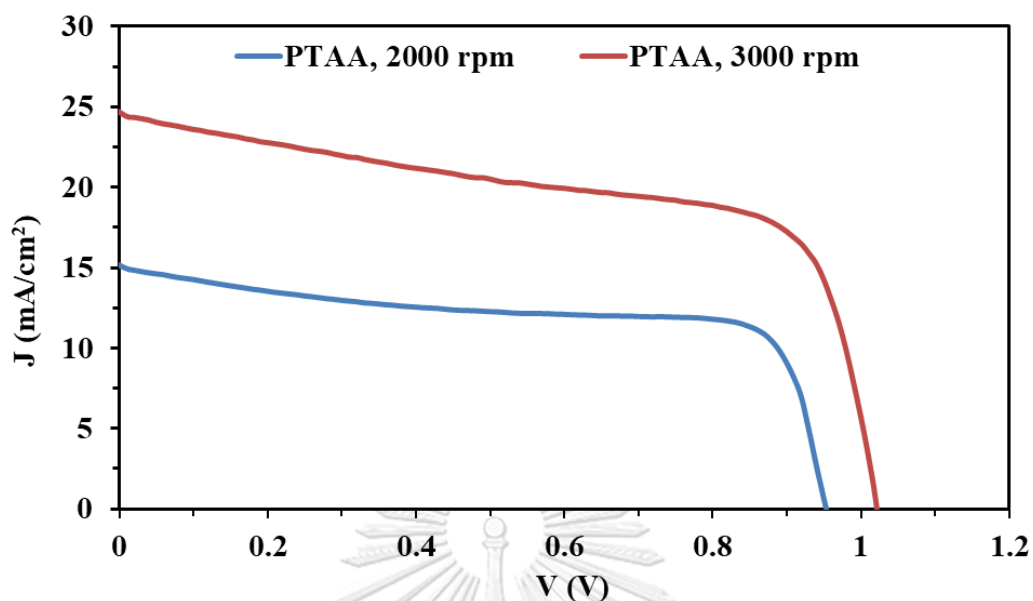


Figure 58. J-V curve of PTAA at spin speed 2000 (blue) and 3000 (red line) rpm for 30 s.

Table 11. Device performance of the inverted perovskite cells using PTAA HTL with different spin speeds between 2000 and 3000 rpm for 30 s.

Photovoltaic parameters (active area 0.06 cm <sup>2</sup> )	PTAA	
	2000 rpm	3000 rpm
V <sub>OC</sub> (V)	0.9	1.0
J <sub>SC</sub> (mA/cm <sup>2</sup> )	15.3	24.9
FF (%)	65.3	61.7
PCE (%)	13.0	15.1

PTAA as HTL can improve the carrier mobility and enhance the efficiency of 15% when using spin speed at 3000 rpm for 30 s, which has a higher PCE than NiO<sub>x</sub> and PEDOT: PSS as HTL, as shown in figure 59.

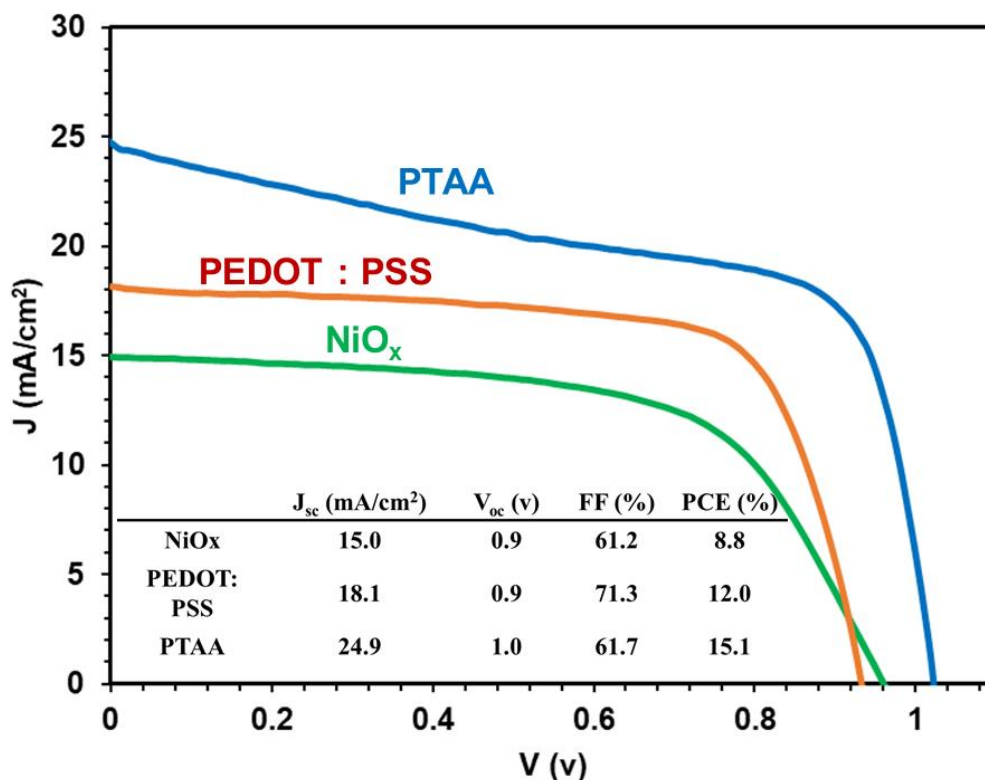


Figure 59. Current-voltage characteristics measured under standard 1 sun condition (AM 1.5 G, 100 mW/cm<sup>2</sup>) of 1 M NiO<sub>x</sub> covered FTO glass at spin speed 5000 rpm (greenline), PEDOT:PSS (HTL solar 3) covered FTO glass at spin speed 6000 rpm (red line), and PTAA covered FTO glass at spin speed 3000 rpm (blue line). The inset shows the solar parameters of different HTMs.

### 5.2.2 Metal contact

The metal contact has a major impact on the electrical properties of the inverted perovskite solar cells (PSCs). The contact is part of the junction of the PSC and must provide lateral charge transport to the terminals, where the metal contact was fabricated by the thermal evaporation technique. It will be investigated the effect of contact on short-circuit current ( $J_{sc}$ ) and power conversion efficiency (PCE). In this part, an experimental study was conducted for various metal contacts, such as aluminum (Al), gold (Au) and silver (Ag).

#### Results and discussions of metal contact

The results of contact as between Au and Ag came out to be a bit different. Al reacts with the underling layer as shown in figure 60.



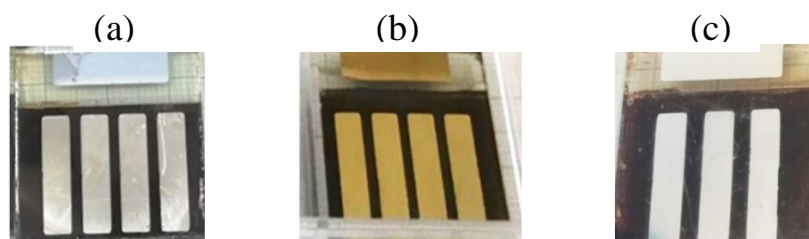


Figure 60. Device fabricated using different contact materials: (a) Al, (b) Au, and (c) Ag.

As shown in Table 12, Au and Ag have a higher work function than Al metal contact, resulting in enhanced PCE. Since Au metal is too expensive, alternative metal contact materials are needed to improve the potential voltage (V) and short-circuit current density of the PSCs. Finally, Ag shows higher performance as contact in the perovskite device architecture. It will be shown in figure 61 and Table 13. By selecting an optimal front contact design, the  $J_{SC}$  and PCE can be increased.

Table 12. Conductivity value for Al, Au and Ag metal [90].

	Al	Au	Ag
conductivity, $\sigma$ (S/cm)	$3.5 \times 10^7$	$4.1 \times 10^7$	$6.3 \times 10^7$

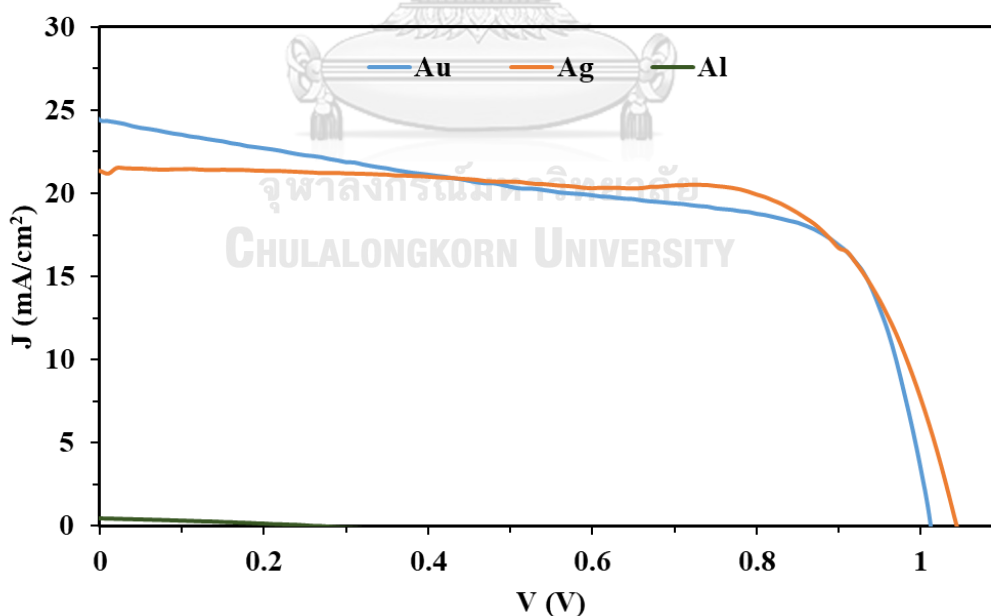


Figure 61. J-V characteristics of the inverted perovskite devices with different metal contacts such as Au (blue line), Ag (red line), and Al (green line).

Table 13. Device performance of the inverted perovskite cells using different metal contacts.

Photovoltaic parameters (active area 0.06 cm <sup>2</sup> )	Metal contact		
	Al	Au	Ag
V <sub>OC</sub> (V)	0.3	1.0	1.0
J <sub>SC</sub> (mA/cm <sup>2</sup> )	0.5	24.9	21.16
FF (%)	30.0	61.7	72.9
PCE (%)	0.035	15.1	15.4

### 5.2.3 Washing surface of PTAA

From 5.2.2, the maximum PCE of 15.4% was obtained, but the larger distributions of the solar cell parameters of the PSCs were observed due to the viscous liquid of the PTAA solution after being spin-coated on the FTO substrates (see figure 62). Thus, the next work will be focused on improving the non-wetting conductive PTAA surface for the deposition of perovskite absorber film.

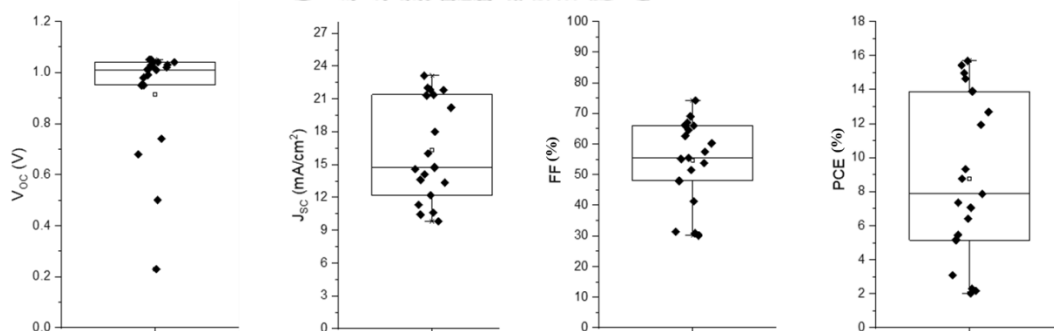
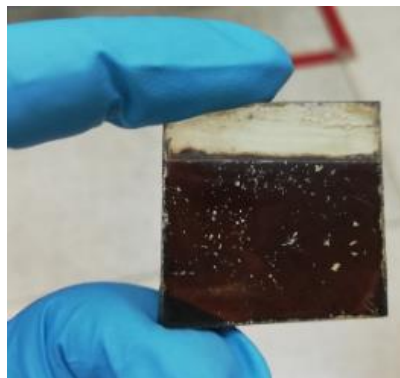


Figure 62. Box chart plots of using PTAA as hole transport material on an inverted structure for 0.06 cm<sup>2</sup> active cell area.

To improve the surface properties of the PTAA films, the surface treatment with dimethylformamide (DMF) and adding some solvents (toluene (TO) and chlorobenzene (CB)) were introduced [92]. But PTAA solution is prepared by mixing 0.007 g of PTAA powder in 1 ml of CB and 0.1  $\mu$ l of 4-tert-butylpyridine (t-BP) and then adding 0.170 g of lithium bistrifluoromethanesulfonimide (Li-TFSI) salt in 1 ml of acetonitrile, which cannot be used after surface treatment with dimethylformamide (DMF) and adding some solvents. Because the PTAA surface might be damaged by the washing process with DMF, or in other words, a reaction might occur on the PTAA surface and perovskite film as shown in figure 63.



*Figure 63. Defection on the PTAA surface from the washing process.*

The PTAA solution (0.0025 g/ml in CB, stirred overnight) was used as a new PTAA solution, which did not react with the washing process. The new PTAA solution was deposited onto the FTO substrates with the spin coating process at a speed of 2000 rpm for 30 s and then heated at 105 °C for 10 min on a hotplate. The wettability of the PTAA films could be improved by washing the PTAA surface with 200  $\mu$ l of DMF and spinning at 4000 rpm for 30 s. In addition, 50  $\mu$ l or 75  $\mu$ l of TO or CB were dropped onto the center of samples at 5 s after the spin-coating of DMF started. The MAPbI<sub>3</sub> perovskite layer was coated on the PTAA layer by a sequential two-step spin-coating process. The first step, PbI<sub>2</sub> solution (0.461 g/ml in volume ratio DMF:DMSO = 4:1, stirred at 70°C overnight), was spin-coated on the PTAA layer at 3000 rpm for 30 s and then baked on a hotplate at 70°C for 20 min. The MAI as second precursor (0.01 g/ml in IPA, stirred overnight) was dropped onto the PbI<sub>2</sub> layer with a 30 s loading time followed by spin-coating at 2000 rpm for 20 s, and repeated again two times for the MAI precursor. Moreover, during the second spin-coating of MAI start, 50  $\mu$ l of CB as anti-solvent was added onto the MAI surface at 5 s. The perovskite layer was baked at 120°C for 10 min on a hotplate. The PC<sub>61</sub>BM as an ETL (0.02 g/ml in CB, stirred overnight) was spin-coated on the perovskite layer at 1500 rpm for 40 s and then followed by BCP (0.0005 g/ml in IPA, stirred overnight) at 4000 rpm for 30 s. The samples were taken out of the glovebox and transferred to the thermal evaporator for the deposition of 120 nm of silver (Ag) counter electrodes. The samples were mechanically scribed into a small active area of 0.06 cm<sup>2</sup>. All layers of PSCs were fabricated in the glovebox, which oxygen and water levels inside below 10 ppm.

The fabrication processes of inverted PSCs are graphically summarized in figure 64. The optical transmission, contact angle, rms surface roughness, and solar cell parameters of perovskite devices are studied to investigate the effects of the treatment on the PTAA surface.

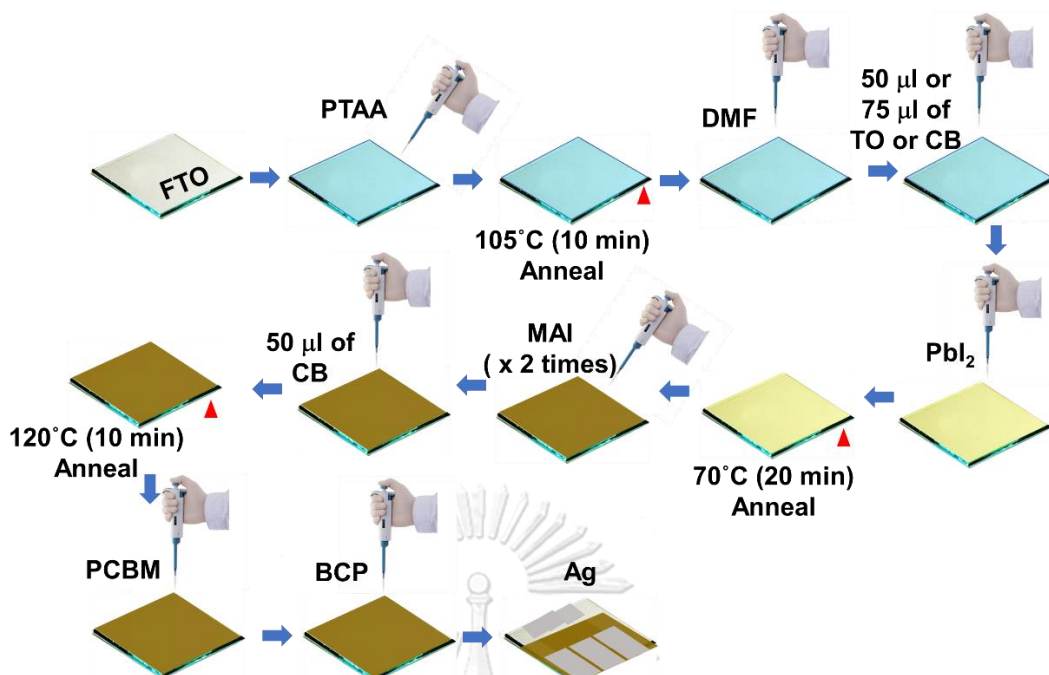


Figure 64. Fabrication procedures of inverted perovskite device.

#### Results and discussions of washing surface of PTAA

The optical transmissions of maximum transmission  $\sim 75\%$  of the pristine and post-treated PTAA samples were investigated in the range of 300–1100 nm as shown in figure 65(left). Furthermore, figure 65(right) shows the transmittance cut-off threshold near 750 nm in all samples, which corresponds to the energy gap ( $E_g$ ) of MAPbI<sub>3</sub> of 1.59 eV. This result confirms that washing with 200 µl DMF and additions of CB or TO on the PTAA surfaces does not affect the optical properties of the PTAA and MAPbI<sub>3</sub> perovskite layers.

Moreover, the contact angles of the pristine and post-treated PTAA surfaces were measured to investigate the wettability of all PTAA surfaces (see figure 66). The 46° contact angle of pristine PTAA surfaces was achieved, which is larger than the post-treated PTAA surfaces. The contact angles of the post-treated PTAA surfaces by washing with 200 µl of DMF and an additional 50 µl of TO significantly decreased to the lowest contact angle of 25°. As a result, applying PbI<sub>2</sub> solution in the two-step spin-coating process for MAPbI<sub>3</sub> perovskite layer gave better coverage on the PTAA surface. Figure 67 displays the morphologies and the surface rms roughness of the pristine and post-treated PTAA surfaces as measured by the AFM. The lowest value of rms roughness for 10 nm of the PTAA surface washed with 200 µl of DMF and an additional 50 µl of TO that responded to the lowest contact angle of 25°, which led to relatively better wettability.

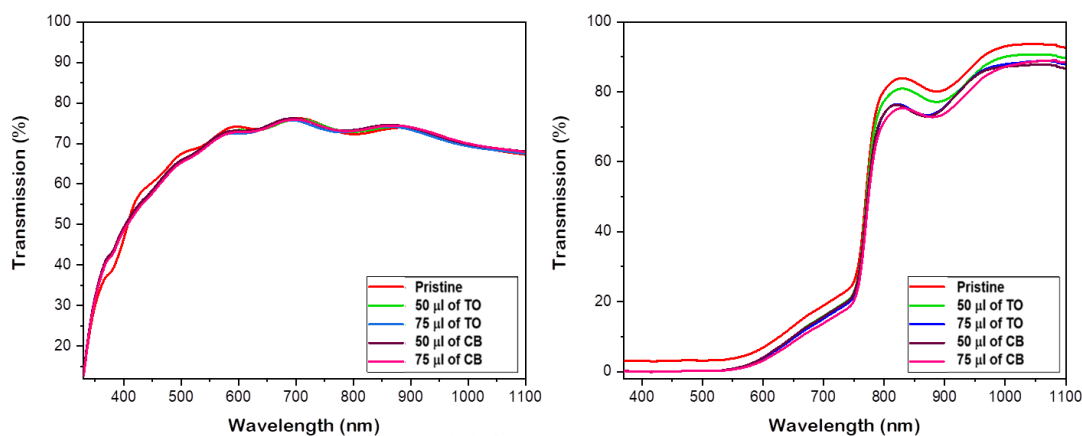


Figure 65. Comparisons of optical transmission spectra of pristine and post-treated PTAA layers (left) and  $\text{MAPbI}_3$  - perovskite on pristine and post-treated PTAA layers (right).



Figure 66. Contact angles of the PTAA films; (a) pristine, and post-treated PTAA by washing with 200  $\mu\text{l}$  of DMF and followed by (b) 50  $\mu\text{l}$  TO, (c) 75  $\mu\text{l}$  TO, (d) 50  $\mu\text{l}$  CB and (e) 75  $\mu\text{l}$  CB.

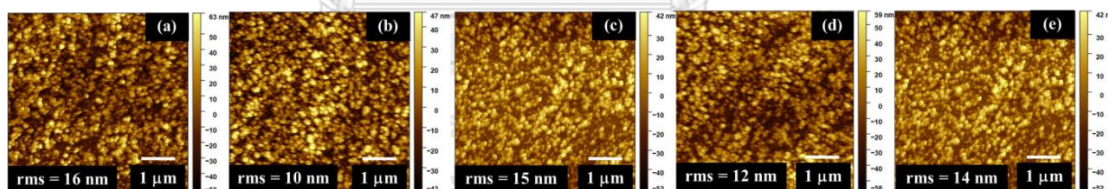


Figure 67. AFM surface morphologies of the PTAA films; (a) pristine, and post-treated PTAA by washing with 200  $\mu\text{l}$  of DMF and followed by (b) 50  $\mu\text{l}$  TO, (c) 75  $\mu\text{l}$  TO, (d) 50  $\mu\text{l}$  CB and (e) 75  $\mu\text{l}$  CB.

The use of this solvent-engineered treatment for the fabrication of inverted PSCs greatly increased the PCE of the device compared to that of the pristine PTAA, contributing to the improved PCE due to the increases in the open-current voltage ( $V_{oc}$ ) and fill factor (FF), as well as leading to small distributions of the solar cell parameters. Figure 68(a) - (e) also included J-V curves and box-chart plots, with data collected from at least 25 cells for each condition. The maximum PCE of 15.4% and the smallest distribution were obtained from washing with 200  $\mu\text{l}$  of DMF and an additional 50  $\mu\text{l}$  of TO onto the PTAA surface. Thus, the post-treated PTAA surface was confirmed from all the data above; it can be reproduced. Table 14 displays the statistical values for the solar cell parameters.

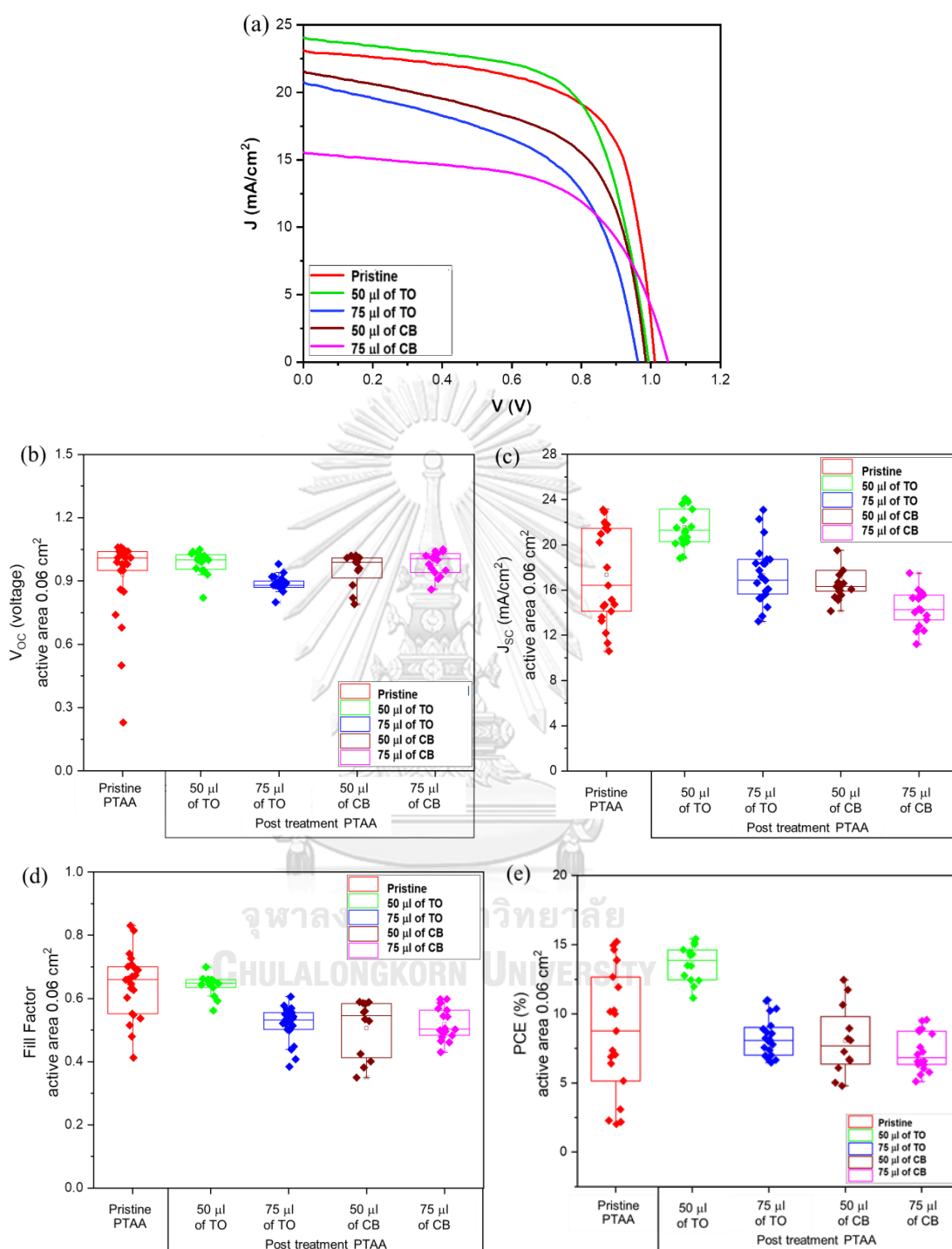


Figure 68. (a)  $J$ - $V$  curves of PSCs for both pristine and post-treated PTAA. Solar cell parameters of PSCs; (b)  $V_{oc}$ , (c)  $J_{sc}$ , (d) Fill Factor and (e) PCE of PSCs comparing between pristine PTAA and post-treated PTAA.

Table 14. Statistical values of solar cell photovoltaic parameters displaying the average values and standard deviations and the maximum values (in the parentheses) of the inverted PSCs fabricated from pristine and post-treated PTAA (batch of 25 devices each).

Photovoltaic parameters (active area 0.06 cm <sup>2</sup> )	Pristine PTAA	Post-treatment PTAA			
		adding 50 $\mu$ l of TO	adding 75 $\mu$ l of TO	adding 50 $\mu$ l of CB	adding 75 $\mu$ l of CB
V <sub>OC</sub> (V)	0.9 $\pm$ 0.2 (1.1)	1.0 $\pm$ 0.1 (1.1)	0.9 $\pm$ 0.1 (1.0)	0.9 $\pm$ 0.1 (1.0)	0.9 $\pm$ 0.1 (1.0)
J <sub>SC</sub> (mA/cm <sup>2</sup> )	14.0 $\pm$ 9.1 (23.1)	21.5 $\pm$ 2.6 (24.1)	17.2 $\pm$ 4.4 (21.6)	17.3 $\pm$ 5.8 (23.1)	14.6 $\pm$ 2.5 (17.5)
FF	0.6 $\pm$ 0.1 (0.7)	0.6 $\pm$ 0.1 (0.7)	0.5 $\pm$ 0.1 (0.6)	0.5 $\pm$ 0.1 (0.6)	0.5 $\pm$ 0.1 (0.6)
PCE (%)	9.3 $\pm$ 4.4 (15.1)	13.6 $\pm$ 1.3 (15.4)	8.1 $\pm$ 2.4 (12.5)	8.3 $\pm$ 1.7 (11.0)	7.3 $\pm$ 1.3 (9.6)

#### 5.2.4 Large active area (0.2 cm<sup>2</sup>) preparation of inverted PSCs for tandem solar cells fabrication

Tandem solar cells was prepared using a combination of Cu(In, Ga)Se<sub>2</sub> (CIGS) solar cells and perovskite solar cells (PSCs), which is the most commonly used in four-terminal (4T) and two-terminal (2T) tandem solar cells. In the previous experiments, the highest PCE of conventional and inverted PSCs were 17.2% and 15.4% for small active area of 0.06 cm<sup>2</sup>. Meanwhile, CIGS bottom cell was obtained PCE of 16.8% in larger active area of 0.515 cm<sup>2</sup>. PSCs need to enhance PCE in larger active area of 0.2 cm<sup>2</sup> close to 16.8% same as CIGS cells to easier electron transport between both solar cells.

Here, using 2,3,5,6-Tetrafluoro-7,7,8,8-tetracyanoquino dimethane (F4-TCNQ) doped PTAA as the HTL was applied to reduce the series resistance of device, which improve the performance of inverted perovskite structure [91, 92], The ratio of F4-TCNQ and PTAA was 0.01wt% [93], they was mixed together in toluene (TO) and heated on hot plate at 70°C overnight. F4-TCNQ doped PTAA solution was spin coated on FTO surface under a spin speed of 4000 rpm for 30 s and then heated at 105°C for 10 min on a hotplate to obtain suitable condition for 0.2 cm<sup>2</sup> large active area of device.

The non-wettability of the PTAA films was reduced by washing with 200  $\mu$ l of DMF by spinning at 4000 rpm for 30 s. In addition, 50  $\mu$ l TO was dropped onto the center of doped PTAA surface at 5 s after the spin-coating of DMF started. PbI<sub>2</sub> (0.461 g/ml in volume ratio DMF:DMSO = 4:1, stirred at 70°C overnight) and MAI (0.01 g/ml in IPA) were sequentially spun on the substrate to make perovskite films at spin speed 3000 rpm for 30 s and 2000 rpm for 20 s, respectively, which MAI was dropped and holded on PbI<sub>2</sub> for 30 s two times, and then they baked on the hotplate at 70°C for 20 s and 120°C for 10 s. In addition, the MAI was spin off of the second

spin-coating at 5 s, 50  $\mu\text{l}$  of CB as anti-solvent was added onto the MAI surface at 5 s. The PC<sub>61</sub>BM as an ETL (0.02 g/ml in CB, stirred overnight) was spin-coated on the perovskite layer at 1500 rpm for 40 s and then followed by BCP (0.0005 g/ml in IPA, stirred overnight) at 4000 rpm for 30 s. The samples were taken out of the glovebox and transferred to the thermal evaporator for the deposition of 120 nm of silver (Ag) electrodes. The samples were mechanically scribed into a large active area of 0.2 cm<sup>2</sup>. All layers of PSCs were fabricated in the glovebox, which oxygen and water levels inside below 10 ppm.

*Results and discussions of large active area (0.2 cm<sup>2</sup>) preparation of inverted PSCs for tandem solar cells fabrication*

The maximum PCE of inverted structure for larger active area of 0.2 cm<sup>2</sup> was 16.8%. The J-V curve and all solar cells parameter were displayed in figure 69 and Table 15.

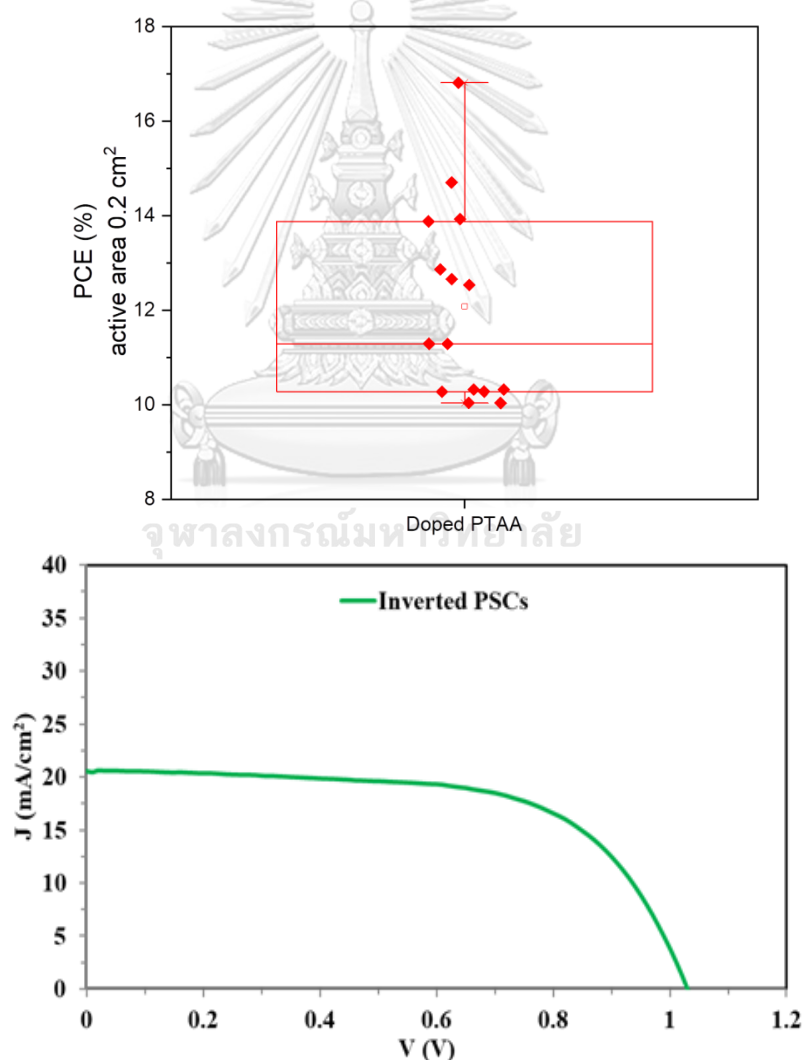


Figure 69. Box chart plots of using F4-TCNQ doped PTAA as hole transport material on inverted structure (above) and the J-V characteristics of F4-TCNQ doped PTAA on inverted PSCs for 0.2 cm<sup>2</sup> active cell area (below).



*Table 15. Statistical values of solar cell photovoltaic parameters displaying the average values and standard deviations and the maximum values (in the parentheses) of the inverted PSCs fabricated from pristine and post-treated PTAA (batch of 15 devices each).*

<b>Photovoltaic parameters (active area 0.2 cm<sup>2</sup>)</b>			
<b>V<sub>oc</sub> (V)</b>	<b>J<sub>sc</sub> (mA/cm<sup>2</sup>)</b>	<b>FF(%)</b>	<b>PCE (%)</b>
1.0 ± 0.1	20.2 ± 2.9	61.5 ± 4.5	13.4 ± 2.2
(1.0)	(25.6)	(63.0)	(16.8)

### 5.3 Four-terminal (4T) PSCs-CIGS tandem solar cells

Among the various photovoltaic (PV) technologies, the tandem solar cells (TSCs) in this work were fabricated using a combination of Cu (In, Ga) Se<sub>2</sub> (CIGS) solar cells and perovskite solar cells (PSCs). The most commonly used TSCs are the four-terminal (4T) and two-terminal (2T) tandem cells (figure 70). A tandem cell, it consists of a narrow-bandgap (NBG; E<sub>g</sub>~1.2 eV) of CIGS as bottom cells and a wide-bandgap (WBG; E<sub>g</sub>~1.6 eV) of perovskite as top cells. ABX<sub>3</sub> perovskite materials are candidates for the development of multi-junction devices aiming to surpass limits associated with stand-alone technologies.

In this thesis, a 4T and 2T PSCs-CIGS tandem solar cells were studied, which is the use of 1.2 eV E<sub>g</sub> of CIGS material that acted as an absorber layer in bottom subcells that has an architecture of Al/ZnO(Al)/i-ZnO/CdS/CIGS/Mo/glass. In fabrication, a perovskite subcells is deposited on CIGS subcells at under 120°C. The MAPbI<sub>3</sub> film acted as a perovskite absorber layer with E<sub>g</sub> of 1.59 eV to fabricate a 4T and 2T perovskite/CIGS tandem.

The substrates for the fabrication of the CIGS solar cells as bottom cells are 3 cm x 3 cm. The 600 nm thick Molybdenum (Mo) film coated soda-lime glass (SLG) substrates by sputtering technique. The total thickness of CIGS absorber layer is around 1.8 μm, which is deposited on Mo film by co-evaporation technique. For a 50 nm thick CdS buffered layer is coated on the CIGS surface by chemical bath deposition (CBD), followed by sputtering of i-ZnO and ZnO(Al) (AZO) window layers of 100 nm and 200 nm thick, respectively. The CIGS devices are completed by the evaporation of Al-grid through the shadow mask and divided into cells of 0.515 cm<sup>2</sup>.

For the inverted perovskite top cells fabrication on 2T and 4T tandem solar cells, F4-TCNQ doped PTAA solution with the ratio of F4-TCNQ and PTAA was 0.01wt% in toluene (TO), which was spin coated on the FTO surface under a spin speed of 4000 for 30 s for a 0.2 cm<sup>2</sup> large active area of device and then heated at 105°C for 10 min on a hotplate. The PTAA surface was treated by washing with 200 μl of DMF at a spin speed of 4000 rpm for 30 s. In addition, 50 μl TO was dropped onto the center of the doped PTAA surface at 5 s after the spin-coating of DMF

started.  $\text{PbI}_2$  (0.461 g/ml in volume ratio DMF:DMSO = 4:1, stirred at 70°C overnight) and MAI (0.01 g/ml in IPA) were sequentially spun on the substrate to make perovskite films at spin speed 3000 rpm for 30 s, and 2000 rpm for 20 s, respectively, which MAI was dropped and holded on  $\text{PbI}_2$  for 30 s two times, and then they baked on the hotplate at 70°C for 20 s and 120°C for 10 s. In addition, the MAI was spun off of the second spin-coating at 5 s, 50  $\mu\text{l}$  of CB as anti-solvent was added onto the MAI surface. The  $\text{PC}_{61}\text{BM}$  as an ETL (0.02 g/ml in CB, stirred overnight) was spin-coated on the perovskite layer at 1500 rpm for 40 s and then followed by BCP (0.0005 g/ml in IPA, stirred overnight) at 4000 rpm for 30 s. The samples were taken out of the glovebox and transferred to the thermal evaporator for the deposition of 120 nm of silver (Ag) electrodes. The samples were mechanically scribed into a large active area of 0.2  $\text{cm}^2$ . All layers of PSCs were fabricated in the glovebox, which oxygen and water levels inside below 10 ppm.

Another top subcell on the 4T tandem device is a normal PSCs. Its ETL is a 50 nm thick Cp-TiO<sub>2</sub> layer and a 300 nm thick Mp-TiO<sub>2</sub> layer, which are deposited on the FTO surface substrate using spin coating at 3000 rpm for 30 s and then baked at 500 °C for 30 minutes.  $\text{PbI}_2$  film (0.461 g of  $\text{PbI}_2$ /1 ml of DMF (N,N-Dimethylformamide) and DMSO (N,N-Dimethylsulfoxide) in a 4:1 ratio) and methyammonium iodide (MAI) solution (0.010 g MAI/1 ml IPA) were used to create the 400 nm thick perovskite films. The  $\text{PbI}_2$  solution is stirred on a hot plate at 70 °C for 12 hours while the MAI solution is stirred at room temperature. They are kept in the glovebox at a relative humidity (RH) of less than 30%. The  $\text{PbI}_2$  solution plays as the first precursor is covered above the electron transport layer (ETL) at a spin speed of 3000 rpm for 30 s and then residual solvent is removed on a hot plate at 70 °C for 20 min. The second precursor solution is the MAI solution that is deposited over the  $\text{PbI}_2$  surface twice at a spin speed of 2000 rpm for 20 s, and each spin MAI solution is holded on the  $\text{PbI}_2$  film for 30 s (called loading time for 30 s). During the second spin off of MAI, anti-solvent is applied and then it is annealed at 120 °C for 15 min. The top of the perovskite film is coated with a 150 nm thick spiro-OMeTAD hole transport layer (HTL) by spin-coating at 3000 rpm for 30 s. All samples are kept in the dry box for 12 hours before the 80-100 nm thick Au contact is thermally evaporated on HTL. Then 0.0723 g of spiro-OMeTAD powder is mixed in 1 ml of CB and 28.8 l of 4-tert-butylpyridine (t-BP), and then 0.520 g of lithium bistrifluoromethanesulfonimide (Li-TFSI) salt is mixed in 1 ml of acetonitrile. In this work, researcher studied the types, the amounts, and the beginning times of toluene (TO) anti-solvents under investigation. After spinning the MAI solution, the amount of anti-solvents is 50  $\mu\text{l}$ , and the elapsed time is 5 seconds.

#### *Results and discussions of four-terminal (4T) PSCs-CIGS tandem solar cells*

The optical property of the normal and inverted perovskite devices are shown in figure 71 where the transmittance cut-off threshold of both devices near 750 nm ( $E_g$  of  $\text{MAPbI}_3$  is 1.59 eV) and the percent transmission is around 70% and 50% for normal and inverted perovskite devices, respectively. In this thesis, the best PCE of 17.2% and 13.3% of normal and inverted perovskite devices were obtained, respectively. Moreover, comparison of the cross-section images of the devices: (a) normal, (b) inverted perovskite device, and (c) tandem solar cells are depicted in figure 72. The

thickness of normal perovskite as top subcells for a 4T tandem device is 491 nm, which is thinner than the 516 nm inverted perovskite, which corresponds to the above transmission results.

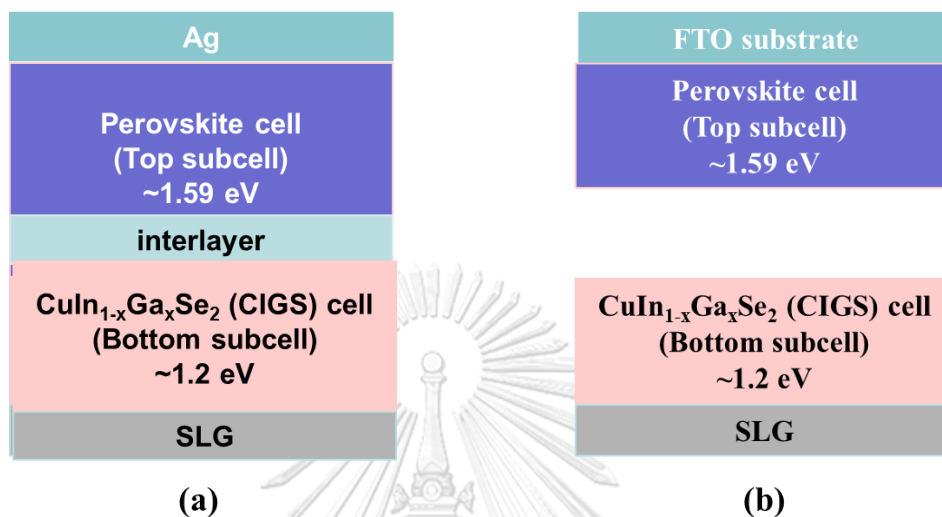


Figure 70. Device schematics of the fabricated (a) two-terminal (2T), (b) four-terminal (4T) perovskite/CIGS tandem solar cells.

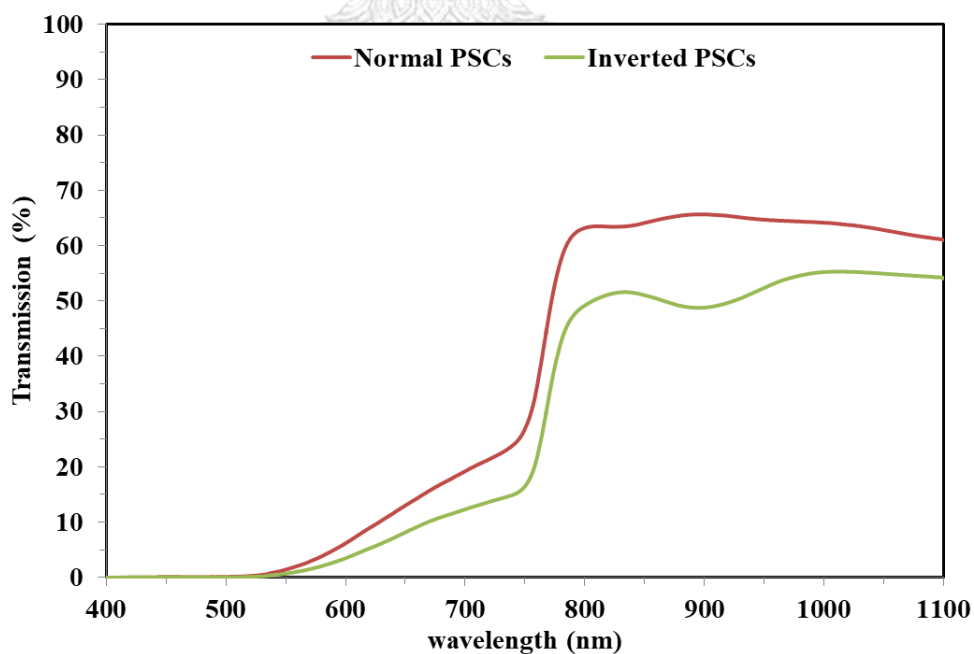


Figure 71. J-V characteristics under illumination of the normal and the inverted perovskite solar cell as indicated in the legend.

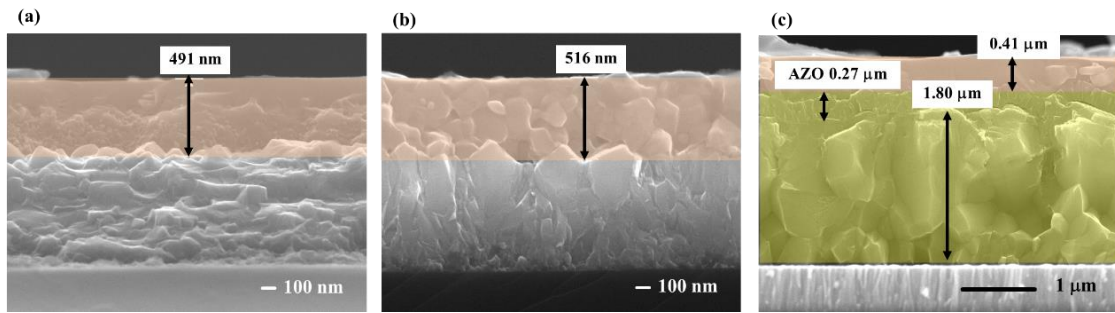


Figure 72. Cross-section images of (a) normal PSCs, (b) inverted PSCs, and (c) two-terminals (2T) inverted perovskite-CIGS tandem solar cells (AZO is ZnO(Al)/i-ZnO).

For the 2T tandem device in this thesis, electrons cannot be transported between the two subcells, which obtained a relatively low PCE of 6.9%. This 2T tandem device has a lower PCE than the PCE of the top and bottom cells, as shown by the J-V curve in figure 73. The obtained  $V_{OC}$  values of 0.67 V are not equal to the sum of the  $V_{OC}$  values of the stand-alone CIGS (0.69 V) and the perovskite top cell (around 1.0 V) (see Table 16), indicating that the two sub-cells are not successfully connected in series in a lossless manner in terms of the photovoltage. The deposition of an interconnecting layer (ICL) is the key to solve this problem, sustain the photocurrent and increasing PCE, consign reduced voltage losses and low resistance [94].

One of the main reasons for this experiment's improvement derives from the fabrication of the 4T tandem device, in which the normal or inverted perovskite structures act as top cells, and the CIGS solar cells act as bottom cells. The 4T tandem device can solve the problem without the ICL on the tandem structure, and J-V measurement can be conducted separately by using 4T. Hence, in the thesis, the 4T tandem structure is also selected to study. Figure 74 demonstrates the external quantum efficiency (EQE) graph of the 4T tandem device with reference to the overall currents by the 4T inverted perovskite-CIGS tandem, 4T normal perovskite-CIGS tandem, CIGS stand alone, and perovskite stand alone. The EQE curve shows the sum of the incident photons for each device. The knee of the EQE graph of filtered with normal PSCs, filtered with inverted PSCs, and PSCs stand-alone devices is demonstrated with the maximum photon absorption at a wavelength of around 750 nm. PSCs could absorb and harvest energy photons in the range of 330 to 800 nm, which is the range of visible light. Whereas the CIGS could generate current from photons in the range of 500 to 1100 nm, where the maximum photon absorption is at a wavelength of about 1100 nm.

Furthermore, figure 75 shows the J-V curve of 4T tandem solar cells. Its PCE is up to 22.6% and 17.6%, when uses normal PSCs and inverted PSCs are employed as top cells, respectively. In this thesis, the PCE of CIGS device, normal PSCs, inverted PSCs, 4T filtered with normal PSCs, and filtered inverted PSCs were obtained 16.8%, 17.2%, 13.3%, 5.4%, and 4.3%, respectively. The photovoltaic parameters of each solar cell are summarized in Table 16.

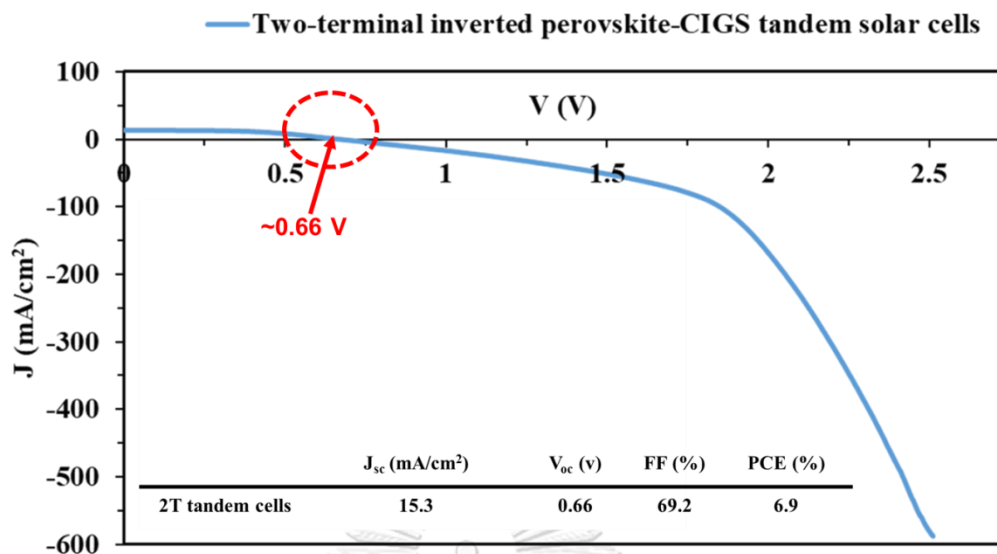


Figure 73. The J-V curve of two-terminal (2T) tandem device. The inset shows the photovoltaic parameters of 2T tandem cells.

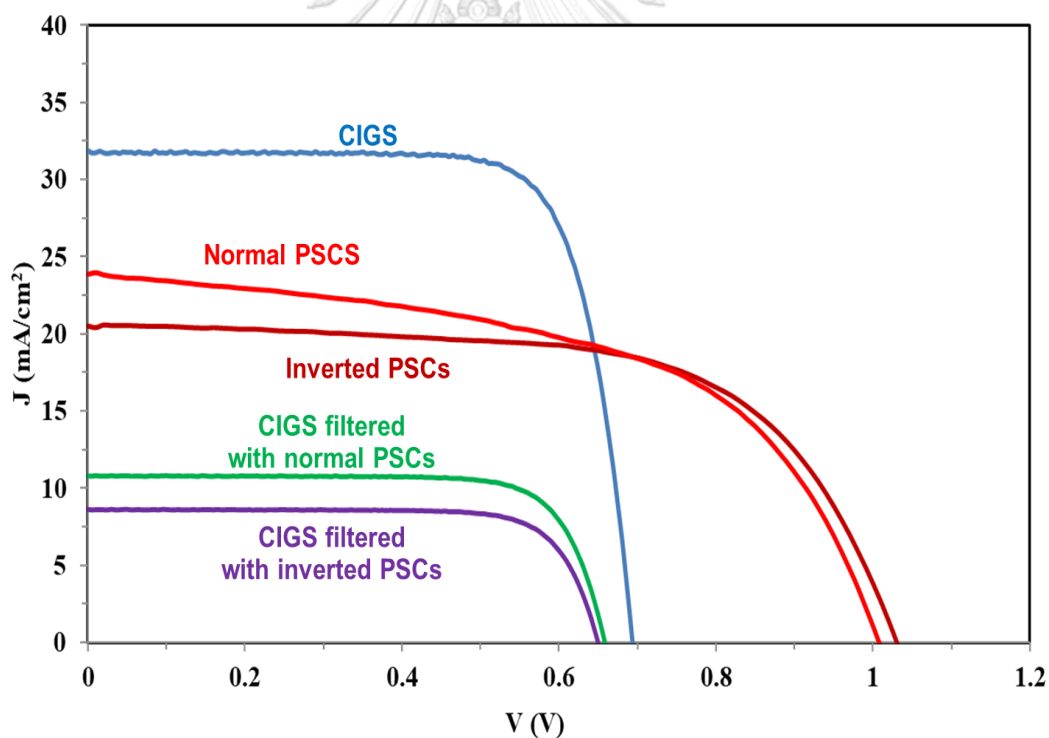


Figure 74. J-V curves of the best-performing tandem device together with CIGS stand-alone (blue line), normal perovskite stand-alone (red line), inverted perovskite stand-alone (light blue line), 4T CIGS filtered with normal perovskite (brown line), and 4T CIGS filtered with inverted perovskite (violent line).

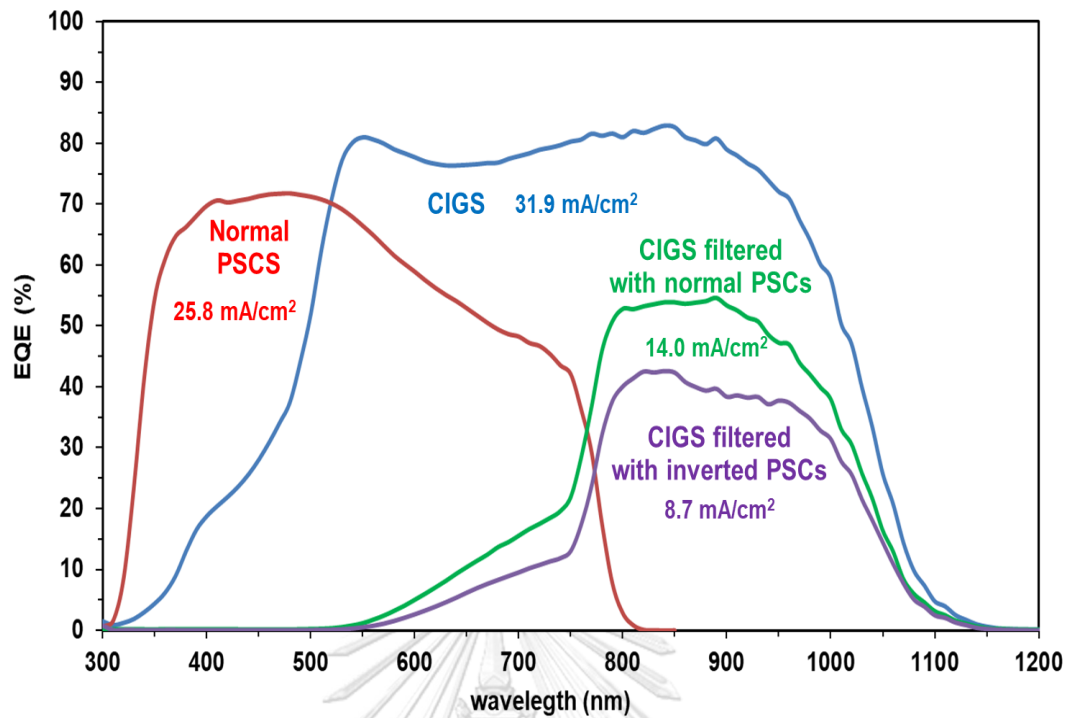


Figure 75. EQE spectra of the perovskite, CIGS subcells and the four-terminal (4T) perovskite-CIGS tandem device.

In 2017, Guchhait et al. suggested a 4T CIGS filtered with normal PSCs tandem solar cells, which the top subcell is PSCs and the bottom subcell is CIGS [95]. Researchers studied the use of an architecture of Al/ZnO(Al)/i-ZnO/CdS/CIGS/Mo/glass. The MAPbI<sub>3</sub> film acted as a perovskite absorber layer with E<sub>g</sub> of 1.59 eV to fabricate a perovskite/CIGS tandem device, which got a PCE of 20.7%. Table 16 shows a comparison between the performance of the 4T tandem device in this thesis and that of Guchhait et al.'s report. Thus, in this thesis, 4T perovskite-based tandem devices can achieve higher PCE than this research group by using a variety of approaches such as the spinning process, annealing, amount of solution, anti-solvent, and washing process. From the knowledge in this research, one can select an alternative way to design a new generation of 4T tandem solar cells in the near future.

*Table 16. Device performances of single-junction and 4T tandem solar cells.*

<b>Photovoltaic parameters</b>	<b>Voc (V)</b>	<b>Jsc (mA/cm<sup>2</sup>)</b>	<b>FF (%)</b>	<b>PCE (%)</b>
CIGS stand alone (this thesis)	0.69	31.9	75.9	16.8
CIGS stand alone (Guchhait et al., 2017)[95]	0.51	38.0	63.8	12.3
Normal perovskite stand alone (this thesis)	0.98	25.8	67.9	17.2
Normal perovskite stand alone (Guchhait et al., 2017)[95]	0.98	20.1	78.1	16.0
Inverted perovskite stand alone (this thesis)	1.01	20.8	64.8	13.3
CIGS filtered with normal PSCs (this thesis)	0.66	14.0	58.5	5.4
CIGS filtered with normal PSCs (Guchhait et al., 2017)[95]	0.47	15.2	64.6	4.7
CIGS filtered with inverted PSCs (this thesis)	0.65	8.7	77.1	4.3
4T normal PSCs-CIGS tandem device (this thesis)				22.6
4T inverted PSCs-CIGS tandem device (Guchhait et al., 2017)[95]				20.7
4T inverted PSCs-CIGS tandem device (this thesis)				17.6

## CHAPTER VI

### CONCLUSIONS

There are many factors such as fabrication processes and materials to increase the performance of normal and inverted PSCs for tandem devices.

In this thesis, the 30NR-D Titania Paste type of  $\text{Mp-TiO}_2$  solution is used to fabricate ETL on normal PSCs with different  $\text{Mp-TiO}_2$  precursor ratios. The best PCE of 9.5% is obtained, which is proposed from 1:7 v/v. The  $\text{Mp-TiO}_2$  ETL was fabricated by the spin coating process in order to achieve a suitable thickness of 189 nm, which can be great for PSCs because a thinner ETL might better facilitate carrier transport to the contact. Moreover, when using 1:7 v/v of  $\text{Mp-TiO}_2$ : Ethanol precursor ratio with spin speed at 3000 rpm for 30 s, the highest PCE of 10.88% was obtained.

In addition, the most important layer for normal PSCs is  $\text{MAPbI}_3$  absorber layer on normal PSCs, which can absorb light and generate electrons.  $\text{MAPbI}_3$  can be proposed from two precursor;  $\text{PbI}_2$  as the first precursor and MAI as the second precursor.  $\text{PbI}_2$  with a different solvent in  $\text{MAPbI}_3$  is selected to increase PCE on PSCs. The suitable solvent for  $\text{PbI}_2$  is using a DMF:DMSO ratio of 4:1, which leads to an increased PCE of 11.9%.

Furthermore, the anti-solvent is one of several techniques chosen to improve the performance of PSCs, which affect the morphology and grain size of the perovskite films. The maximum PCE of 17.2% is achieved from 50  $\mu\text{l}$  of CB anti-solvent applied at 5 s elapsed time after spinning the MAI solution.

Next, the exploration of HTL for inverted PSCs is studied. In the presence of  $\text{NiO}_x$  as HTL can improve PCE and FF when using a concentration of 1 M  $\text{NiO}_x$  on the inverted perovskite device, the spin speed at 8000 rpm for 30 s. The PCE of 8.8% and the FF of 61.2% are obtained.

Additionally, the performance of PSCs with another HTL, PEDOT:PSS was studied. The use of PEDOT:PSS (HTL solar 3) at a spin speed of 6000 rpm for 30 s received the best PCE of 12%.

But the potential of a PEDOT:PSS-based device is only 0.9 V, which is less than PTAA as HTL. To enhance potential up to 1.1 V, PTAA played as HTL on inverted PSCs and can be baked at a low temperature. The high PCE of 15.1% was obtained in inverted PSCs using PTAA, which is significantly better than that of  $\text{NiO}_x$  and PEDOT:PSS-based devices.

From the above results, the metal contact of PSCs is Au contact, but it is too expensive. For an alternative choice of metal contact, Ag contact has been introduced because Ag is cheaper and can increase the photovoltaic parameters of the PSCs. Ag is able to show an optimal front contact design due to a high PCE of 15.4% and a high FF of 72.9%.



For inverted PSCs, the larger distributions of the solar cell parameters were observed because of the viscous liquid of the PTAA solution. To solve non-wetting of the PTAA surface, washing the PTAA surface with 200  $\mu\text{l}$  DMF and adding 50  $\mu\text{l}$  of CB solvents was used. This indicates that the maximum PCE of 15.4% and the smallest distribution were obtained, indicating that the washing method can improve the non-wetting surface. Although, the completely covered small active area of 0.06  $\text{cm}^2$  is successfully achieved with the washing process. But tandem solar cells was prepared using a combination of Cu(In, Ga)Se<sub>2</sub> (CIGS) solar cells and PSCs, which is large active area of 0.515  $\text{cm}^2$ . In this part, the large active area of 0.2  $\text{cm}^2$  on inverted PSCs was improved with F4-TCNQ doped PTAA as the HTL, which required an average PCE of 13.3%.

Finally, the J-V curves of a four-terminal (4T) perovskite/CIGS tandem device together with stand-alone perovskite and CIGS sub-cells were investigated. The maximum tandem device PCE was 22.6%. The detailed spectral response of the tandem cell was characterized by an EQE measurement of each sub cell while keeping the other sub cell current saturated using bias light sources with appropriate spectral in a range of 330 to 1200 nm. The EQE spectra show that the perovskite as top cell and the CIGS as bottom cell generated photocurrents of 25.8 and 31.9  $\text{mA}/\text{cm}^2$ , respectively.

## APPENDICES

### APPENDIX A

#### List of Symbols and Abbreviations

AFM	Atomic force microscopy
Al	Aluminum
Ag	Silver
AM 1.5, AM 0	Air mass 1.5, air mass 0
Ar	Argon
Au	Gold
$b_s(E)$	Incident spectral photon flux density
BCP	Bis(trifluoromethane) sulfonamide lithium salt
Br	Bromine
$C_B$	The conduction band
Cp	Compact
CB	Chlorobenzene
CBD	Chemical bath deposition
CGS	Copper gallium diselenide
$CH_3NH_2$	Methylamine
$CH_3NH_3Cl$	Methylammonium chloride
$CH_3NH_3I$	Methylammonium iodide
$CH_3NH_3PbI_3$	Methylammonium lead iodide
$CH_3NH_3PbI_{3-x}Cl_x$	Methylammonium lead mixed iodide-chloride
CIGS	Copper indium gallium diselenide
CIS	Copper indium diselenide
Cl	Chlorine
Cu	Copper
CVD	Chemical vapor deposition
DC	Direct current
DMF	N, N-Dimethylformamide
DMSO	Dimethyl sulfoxide
E	Energy band
$E_C$	Conduction band energy
$E_F$	Fermi energy
$E_{Fn}$	Fermi energy of N-type semiconductor
$E_{Fp}$	Fermi energy of P-type semiconductor
$E_g$	Energy band gap
$E_V$	Valance band energy
EDS	Energy dispersive X-ray spectroscopy
ETL	Electron transporting layer
ETM	Electron transporting material
EQE	External quantum efficiency
F4-TCNQ	2,3,5,6-Tetrafluoro-7,7,8,8-tetracyanoquino dimethane
FF	Fill factor
FTO	Fluorine doped tin oxide

HCl	Hydrochloric acid
HOMO	Highest occupied molecular orbital
HTM	Hole transporting layer
HTM	Hole transporting material
$I$	Current
I	Iodine
i	Intrinsic
$I_{\text{dark}}(\text{V})$	Dark current
IPA	Isopropyl alcohol
ITO	Indium tin oxide
I-V	Current-Voltage
IQE	Internal quantum efficiency
J	Current density
$J_0$	Saturation current density
$J_{\text{dark}}(\text{V})$	Dark current density
$J_e$	Electron flux
$J_h$	Hole flux
$J_m$	Maximum current density
$J_{\text{SC}}$	Short circuit current density
$k_B$	Boltzmann's constant
Li-TFSI	Lithium bistrifluoromethanesulfonimide
MAI	Methylammonium iodide
$\text{MAPbI}_3$	Methylammonium lead iodide
$\text{MAPbX}_3$	Methylammonium lead halide
MBD	Molecular beam deposition
min	Minute
$M_p$	Mesoporous
NBG	Narrow-bandgap
$\text{NiO}_x$	Nickel (II) oxide
NIR	Near infrared
NREL	National Renewable Energy Laboratory
$\text{O}_2$	Dioxygen
P	Power density
Pb	Lead
$\text{PbCl}_2$	Lead (II) chloride
$\text{PbI}_2$	Lead (II) iodide
$\text{PbX}_2$	Lead halide
$\text{PC}_{61}\text{BM}$	[6,6]-Phenyl-C61-butyric acid methyl ester
PCE	Power conversion efficiency
PEDOT: PSS	Poly(3,4-ethylenedioxythiophene) polystyrene sulfonate
PH 1000	Poly(3,4-ethylenedioxythiophene) polystyrene sulfonate product with PEDOT to PSS weight ratio of 1:2.5
$P_m$	Maximum power
$P_s$	Incident light power density
PVD	Physical vapor deposition
q	Electronic charge
QE	Quantum efficiency

RF	Radio frequency
$R_L$	Load resistance
$R_s$	Series resistance
$R_{sh}$	Shunt resistance
%R	Optical refraction
STC	Standard test conditions
SEM	Scanning electron microscope
SLG	Soda-lime glass
Spiro-OMeTAD	2,2',7,7'-Tetrakis(N,N-di-p-methoxyphenylamine)- 9,9'-spirobifluorene
STC	Standard Test Condition
T	Temperature
$T_{sub}$	Substrate temperature
$T_{pyro}$	Pyrometer temperature
t-BP	4-tert-butylpyridine
TCO	Transparent conducting oxide
Ti	Titanium
$TiO_2$	Titanium dioxide
TO	Toluene
%T	Optical transmission
UV	Ultraviolet
V	Voltage
VIS	Visible
$V_m$	Maximum voltage
$V_{oc}$	Open circuit voltage
$\theta$	Contact angle
$\mu m$	Micrometer
$^{\circ}C$	Degree Celsius
$cm^2$	Square centimeter
$mA/cm^2$	Milliampere per square centimeter
$W/m^2$	Watt per square meter
$\Omega/sq$	Ohm per square, unit of sheet resistance
cm	Centimeter
eV	Electron volt
h	Hour
kHz	Kilohertz
mA	Milliampere
mg/ml	Milligram per milliliter
mol/l	Mole per liter
mol%	Molar percentage
nm	Nanometer
ppm	Parts per million
rpm	Revolutions per minute
rpm/s	Revolutions per minute per second
s	Second
v%	Percentage by volume
$V_B$	The valence band

v/v	volume per volume
WBG	wide-bandgap
wt%	Percentage by weight
$\theta$	Contact angle



## REFERENCES

1. Anaya, M., et al., *ABX<sub>3</sub> Perovskites for Tandem Solar Cells*. Joule, 2017. **1**(4): p. 769-793.
2. He, X., *Perovskite Photovoltaics 2016-2026: Technologies, Markets, Players*. 2016.
3. Dou, L., *Emerging two-dimensional halide perovskite nanomaterials*. J. Mater. Chem. C, 2017. **5**.
4. *NUMERICAL OPTIMIZATION OF ORGANIC AND HYBRID MULTI-JUNCTION AND TANDEM SOLAR CELLS*, in <https://www.fluxim.com/simulation-multi-junction-solar-cells>, u.g.o.a. Model validation and parameter extraction by consistently fitting the experimental current-voltage characteristics of single-junction and tandem cells with Setfos, Editor.
5. *A decade of perovskite photovoltaics*. Nature Energy, 2019. **4**(1): p. 1-1.
6. Singh, M., et al., *Comparing optical performance of a wide range of perovskite/silicon tandem architectures under real-world conditions*. Nanophotonics, 2020. **10**(8): p. 2043-2057.
7. Moradbeigi, M. and M. Razaghi, *Investigation of optical and electrical properties of novel 4T all perovskite tandem solar cell*. Scientific Reports, 2022. **12**(1): p. 6733.
8. Ghorashi, S.M.B., A. Behjat, and R. Ajeian, *The effect of a buffer layer on the performance and optimal encapsulation time of ITO/CuPc/C60/buffer/Cu bilayer cells*. Solar Energy Materials and Solar Cells, 2012. **96**: p. 50–57.
9. Cao, Q., et al., *N-Type Conductive Small Molecule Assisted 23.5% Efficient Inverted Perovskite Solar Cells*. Advanced Energy Materials, 2022. **n/a**(n/a): p. 2201435.
10. Elumalai, N.K., et al., *Perovskite Solar Cells: Progress and Advancements*. Energies, 2016. **9**: p. 861.
11. Li, T.-T., et al., *Two-Terminal Perovskite-Based Tandem Solar Cells for Energy Conversion and Storage*. Small, 2021. **17**(23): p. 2006145.
12. Basumatary, P. and P. Agarwal, *A short review on progress in perovskite solar cells*. Materials Research Bulletin, 2022. **149**: p. 111700.
13. Stoumpos, C.C., C.D. Malliakas, and M.G. Kanatzidis, *Semiconducting Tin and Lead Iodide Perovskites with Organic Cations: Phase Transitions, High Mobilities, and Near-Infrared Photoluminescent Properties*. Inorganic Chemistry, 2013. **52**(15): p. 9019-9038.
14. Liu, Y., Z. Yang, and S. Liu, *Recent Progress in Single-Crystalline Perovskite Research Including Crystal Preparation, Property Evaluation, and Applications*. Advanced Science, 2018. **5**(1): p. 1700471.
15. De Wolf, S., et al., *Organometallic Halide Perovskites: Sharp Optical Absorption Edge and Its Relation to Photovoltaic Performance*. The journal of physical chemistry letters, 2014. **5** **6**: p. 1035-9.
16. Noh, J.H., et al., *Chemical Management for Colorful, Efficient, and Stable Inorganic–Organic Hybrid Nanostructured Solar Cells*. Nano Letters, 2013. **13**(4): p. 1764-1769.
17. Hao, F., et al., *Lead-free solid-state organic–inorganic halide perovskite solar*

- cells. *Nature Photonics*, 2014. **8**(6): p. 489-494.
18. Hao, F., et al., *Anomalous Band Gap Behavior in Mixed Sn and Pb Perovskites Enables Broadening of Absorption Spectrum in Solar Cells*. *Journal of the American Chemical Society*, 2014. **136**(22): p. 8094-8099.
  19. Stoumpos, C.C., et al., *Hybrid Germanium Iodide Perovskite Semiconductors: Active Lone Pairs, Structural Distortions, Direct and Indirect Energy Gaps, and Strong Nonlinear Optical Properties*. *Journal of the American Chemical Society*, 2015. **137**(21): p. 6804-6819.
  20. Levchuk, I., et al., *Brightly Luminescent and Color-Tunable Formamidinium Lead Halide Perovskite FAPbX<sub>3</sub> (X = Cl, Br, I) Colloidal Nanocrystals*. *Nano Letters*, 2017. **17**(5): p. 2765-2770.
  21. Eperon, G.E., et al., *Perovskite-Perovskite Tandem Photovoltaics with Optimized Bandgaps*. *Science*, 2016. **354**: p. 861.
  22. Li, Z., et al., *Stabilizing Perovskite Structures by Tuning Tolerance Factor: Formation of Formamidinium and Cesium Lead Iodide Solid-State Alloys*. *Chemistry of Materials*, 2016. **28**(1): p. 284-292.
  23. Jeon, N.J., et al., *Compositional engineering of perovskite materials for high-performance solar cells*. *Nature*, 2015. **517**(7535): p. 476-480.
  24. Lee, J.-W., et al., *Formamidinium and Cesium Hybridization for Photo- and Moisture-Stable Perovskite Solar Cell*. *Advanced Energy Materials*, 2015. **5**(20): p. 1501310.
  25. Saliba, M., et al., *Cesium-Containing Triple Cation Perovskite Solar Cells: Improved Stability, Reproducibility and High Efficiency*. *Energy Environ. Sci.*, 2016. **9**: p. 1989.
  26. Collavini, S., et al., *Efficient Regular Perovskite Solar Cells Based on Pristine [70]Fullerene as Electron-Selective Contact*. *ChemSusChem*, 2016. **9**(11): p. 1263-1270.
  27. Burschka, J., et al., *Sequential deposition as a route to high-performance perovskite-sensitized solar cells*. *Nature*, 2013. **499**(7458): p. 316-319.
  28. Leydesdorff, L., et al., *Patents as instruments for exploring innovation dynamics: geographic and technological perspectives on "photovoltaic cells"*. *Scientometrics*, 2015. **102**(1): p. 629-651.
  29. Tang, J., et al., *Synthesis of colloidal CuGaSe<sub>2</sub>, CuInSe<sub>2</sub>, and Cu(InGa)Se<sub>2</sub> nanoparticles*. *Chemistry of Materials - CHEM MATER*, 2008. **20**: p. 6906-6910.
  30. Gloeckler, M. and J.R. Sites, *Band-gap grading in Cu(In,Ga)Se<sub>2</sub> solar cells*. *Journal of Physics and Chemistry of Solids*, 2005. **66**: p. 1891-1894.
  31. Nakamura, M., et al., *Cd-Free Cu(In,Ga)(Se,S)<sub>2</sub> thin-film solar cell with record efficiency of 23.35%*. *IEEE Journal of Photovoltaics*, 2019. **9**: p. 1863-1867.
  32. Meillaud, F., et al., *Efficiency limits for single-junction and tandem solar cells*. *Solar Energy Materials and Solar Cells*, 2006. **90**.
  33. Green, M.A., et al., *Solar cell efficiency tables (Version 60)*. *Progress in Photovoltaics: Research and Applications*, 2022. **30**(7): p. 687-701.
  34. Kim, D.H., et al., *Bimolecular Additives Improve Wide-Band-Gap Perovskites for Efficient Tandem Solar Cells with CIGS*. *Joule*, 2019. **3**(7): p. 1734-1745.
  35. Su, P., et al., *Pb-Based Perovskite Solar Cells and the Underlying Pollution behind Clean Energy: Dynamic Leaching of Toxic Substances from Discarded*

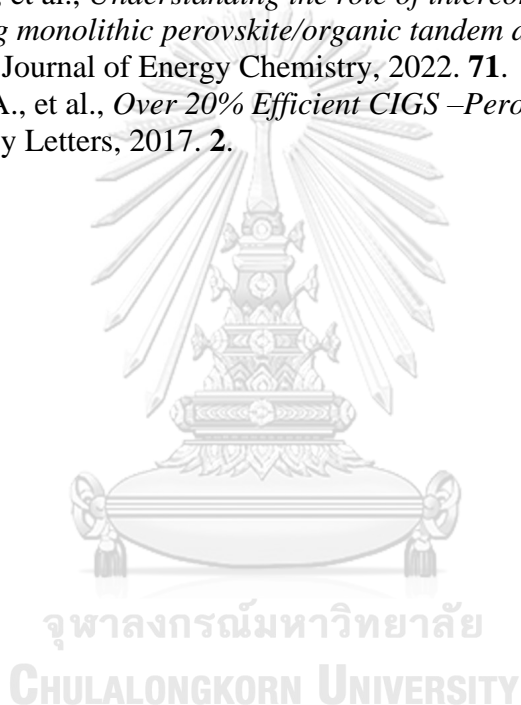
- Perovskite Solar Cells*. The Journal of Physical Chemistry Letters, 2020. **11**(8): p. 2812-2817.
36. Fatema, K. and M.S. Arefin, *Enhancing the efficiency of Pb-based and Sn-based perovskite solar cell by applying different ETL and HTL using SCAPS-ID*. Optical Materials, 2022. **125**: p. 112036.
  37. Bowman, A.R., et al., *Relaxed Current Matching Requirements in Highly Luminescent Perovskite Tandem Solar Cells and Their Fundamental Efficiency Limits*. ACS Energy Letters, 2021. **6**(2): p. 612-620.
  38. Contreras, M., et al., *High efficiency Cu(In,Ga)Se<sub>2</sub>-based solar cells: Processing of novel absorber structures*. Conference Record of the IEEE Photovoltaic Specialists Conference, 2002. **1**.
  39. Bouich, A., et al., *Deposit on different back contacts: to high-quality CuInGaS<sub>2</sub> thin films for photovoltaic application*. Journal of Materials Science: Materials in Electronics, 2019. **30**.
  40. Todorov, T., et al., *Monolithic Perovskite-CIGS Tandem Solar Cells via In Situ Band Gap Engineering*. Advanced Energy Materials, 2015. **5**(23): p. 1500799.
  41. Jeon, N.J., et al., *Solvent engineering for high-performance inorganic-organic hybrid perovskite solar cells*. Nature Materials, 2014. **13**(9): p. 897-903.
  42. Ghosh, S., S. Mishra, and T. Singh, *Antisolvents in Perovskite Solar Cells: Importance, Issues, and Alternatives*. Advanced Materials Interfaces, 2020. **7**(18): p. 2000950.
  43. Lee, K.-M., et al., *Selection of anti-solvent and optimization of dropping volume for the preparation of large area sub-module perovskite solar cells*. Solar Energy Materials and Solar Cells, 2017. **172**: p. 368-375.
  44. Zhao, D., et al., *Four-Terminal All-Perovskite Tandem Solar Cells Achieving Power Conversion Efficiencies Exceeding 23%*. 2018. **3**.
  45. Jošt, M., et al., *Monolithic Perovskite Tandem Solar Cells: A Review of the Present Status and Advanced Characterization Methods Toward 30% Efficiency*. Advanced Energy Materials, 2020. **10**(26): p. 1904102.
  46. Sultana, N., M. Islam, and Z. Mahmood, *Utilization of low cost metals as back contact with Perovskite Solar Cell*. Dhaka University Journal Applied Science & Engineering, 2017. **4**: p. 35-38.
  47. Abdollahi Nejand, B., et al., *Scalable two-terminal all-perovskite tandem solar modules with a 19.1% efficiency*. Nature Energy, 2022. **7**(7): p. 620-630.
  48. Jošt, M., et al., *Perovskite/CIGS Tandem Solar Cells: From Certified 24.2% toward 30% and Beyond*. ACS Energy Letters, 2022. **7**(4): p. 1298-1307.
  49. Prince, K.J., et al., *Complementary interface formation toward high-efficiency all-back-contact perovskite solar cells*. 2021. **2**.
  50. Shalenov, E.O., et al., *Performance evaluation of different designs of back-contact perovskite solar cells*. Solar Energy Materials and Solar Cells, 2022. **234**: p. 111426.
  51. Dutta, M., L. Thirugnanam, and N. Fukata, *Si Nanowire Solar Cells: Principles, Device Types, Future Aspects, and Challenges*. 2018. p. 299-329.
  52. Lee, S., et al., *Robust nanoscale contact of silver nanowire electrodes to semiconductors to achieve high performance chalcogenide thin film solar cells*. Nano Energy, 2018. **53**: p. 675-682.
  53. Barkat, L., et al., *Efficient hole-transporting layer MoO<sub>3</sub>:CuI deposited by co-*



- evaporation in organic photovoltaic cells. *physica status solidi (a)*, 2016. **214**.
54. Bedia, F.Z., et al., *Influence of Al-doped ZnO Transparent Contacts Deposited by a Spray Pyrolysis Technique on Performance of HIT Solar Cells*. *Energy Procedia*, 2014. **50**: p. 853-861.
  55. Zhong, Y., et al., *Role of PCBM in the Suppression of Hysteresis in Perovskite Solar Cells*. *Advanced Functional Materials*, 2020. **30**: p. 1908920.
  56. Mustafa, R., et al., *Environmental Impacts on the Performance of Solar Photovoltaic Systems*. *Sustainability*, 2020. **12**: p. 608.
  57. Van Dyk, E. and E.L. Meyer, *Analysis of the effect of parasitic resistances on the performance of photovoltaic modules*. *Renewable Energy*, 2004. **29**: p. 333-344.
  58. Lu, H., et al., *Mechanical Writing of Ferroelectric Polarization*. *Science (New York, N.Y.)*, 2012. **336**: p. 59-61.
  59. Zhang, T., et al., *Understanding the Relationship between Ion Migration and the Anomalous Hysteresis in High-Efficiency Perovskite Solar Cells: A Fresh Perspective from Halide Substitution*. *Nano Energy*, 2016. **26**.
  60. Lee, J.-W., et al., *The Interplay between Trap Density and Hysteresis in Planar Heterojunction Perovskite Solar Cells*. *Nano Letters*, 2017. **17**.
  61. Vahlman, H., et al., *CAPACITIVE EFFECTS IN HIGH-EFFICIENCY SOLAR CELLS DURING I-V CURVE MEASUREMENT: CONSIDERATIONS ON ERROR OF CORRECTION AND EXTRACTION OF MINORITY CARRIER LIFETIME*. 2018.
  62. Elumalai, N.K. and A. Uddin, *Hysteresis in organic-inorganic hybrid perovskite solar cells*. *Solar Energy Materials and Solar Cells*, 2016. **157**: p. 476-509.
  63. Kim, Y.Y., et al., *Roll-to-roll gravure-printed flexible perovskite solar cells using eco-friendly antisolvent bathing with wide processing window*. *Nature Communications*, 2020. **11**(1): p. 5146.
  64. Lao, Y., et al., *The preparation method of double-blade coating to 'write' high efficiency perovskite solar cells*. *Organic Electronics*, 2022. **100**: p. 106374.
  65. Patidar, R., et al., *Slot-die coating of perovskite solar cells: An overview*. 2019. **22**: p. 100808.
  66. Seo, Y.-H., et al., *Temperature-controlled slot-die coating for efficient and stable perovskite solar cells*. *Journal of Power Sources*, 2022. **539**: p. 231621.
  67. Bishop, J.E., J.A. Smith, and D.G. Lidzey, *Development of Spray-Coated Perovskite Solar Cells*. *ACS Applied Materials & Interfaces*, 2020. **12**(43): p. 48237-48245.
  68. Bishop, J.E., et al., *High-Efficiency Spray-Coated Perovskite Solar Cells Utilizing Vacuum-Assisted Solution Processing*. *ACS Applied Materials & Interfaces*, 2018. **10**(46): p. 39428-39434.
  69. Fourati, N., et al., *Chemical and Biological Sensors from Conducting and Semiconducting Polymers*, in *Reference Module in Materials Science and Materials Engineering*. 2016, Elsevier.
  70. Tongpool, R. and S. Yoriya, *Kinetics of nitrogen dioxide exposure in lead phthalocyanine sensors*. *Thin Solid Films*, 2005. **477**(1): p. 148-152.
  71. Hamukwaya, S.L., et al., *A Review of Recent Developments in Preparation Methods for Large-Area Perovskite Solar Cells*. *Coatings*, 2022. **12**(2).
  72. Lee, H.-K., S.-I. Chang, and E. Yoon, *A Flexible Polymer Tactile Sensor:*

- Fabrication and Modular Expandability for Large Area Deployment*. Microelectromechanical Systems, Journal of, 2007. **15**: p. 1681-1686.
73. Refaei, M., *Modeling and Simulation of III-Nitride-Based Solar Cells using Nextnano®*. 2017.
  74. Nickheslat, A., et al., *Phenol Photocatalytic Degradation by Advanced Oxidation Process under Ultraviolet Radiation Using Titanium Dioxide*. Journal of environmental and public health, 2013. **2013**: p. 815310.
  75. Sun, L., et al., *Synthesis and Applications of Molecularly Imprinted Polymers Modified TiO<sub>2</sub> Nanomaterials: A Review*. Polymers, 2018. **10**: p. 1248.
  76. Godbert, N., T. Mastropietro, and T. Poerio, *Mesoporous TiO<sub>2</sub> Thin Films: State of the Art*. 2018.
  77. Li, H., et al., *High-Efficiency and Stable Perovskite Solar Cells Prepared Using Chlorobenzene/Acetonitrile Antisolvent*. ACS Applied Materials & Interfaces, 2019. **11**(38): p. 34989-34996.
  78. Butsriruk, K., T. Taychatanapat, and S. Chatraphorn, *Effects of anti-solvent in the two-step fabrication of absorber layer in perovskite solar cells*. Journal of Physics: Conference Series, 2019. **1380**.
  79. Tress, W., et al. *The role of the hole-transport layer in perovskite solar cells - reducing recombination and increasing absorption*. in *2014 IEEE 40th Photovoltaic Specialist Conference (PVSC)*. 2014.
  80. Li, S., et al., *A brief review of hole transporting materials commonly used in perovskite solar cells*. Rare Metals, 2021. **40**(10): p. 2712-2729.
  81. Jin, Z., et al., *Modification of NiOx hole transport layer for acceleration of charge extraction in inverted perovskite solar cells*. RSC Advances, 2020. **10**(21): p. 12289-12296.
  82. Zhao, X., et al., *Photoconductive NiOx hole transport layer for efficient perovskite solar cells*. Chemical Engineering Journal, 2022. **435**: p. 135140.
  83. Xia, Y. and S. Dai, *Review on applications of PEDOTs and PEDOT:PSS in perovskite solar cells*. Journal of Materials Science: Materials in Electronics, 2020: p. 1-12.
  84. Sun, K., et al., *Review on application of PEDOTs and PEDOT:PSS in energy conversion and storage devices*. Journal of Materials Science: Materials in Electronics, 2015. **26**: p. 4438-4462.
  85. Kim, D.H., et al., *Tailoring PEDOT:PSS polymer electrode for solution-processed inverted organic solar cells*. Solid-State Electronics, 2020. **169**: p. 107808.
  86. Mansour, A., et al., *Conductive polymer work function changes due to residual water: impact of water's temperature dependent dielectric constant*. Advanced Electronic Materials, 2020. **6**.
  87. Afzal, A.M., et al., *Highly efficient self-powered perovskite photodiode with an electron-blocking hole-transport NiOx layer*. Scientific Reports, 2021. **11**(1): p. 169.
  88. Zhao, Q., et al., *Achieving efficient inverted planar perovskite solar cells with nondoped PTAA as a hole transport layer*. Organic Electronics, 2019. **71**: p. 106-112.
  89. Wang, Y., et al., *PTAA as Efficient Hole Transport Materials in Perovskite Solar Cells: A Review*. Solar RRL, 2022. **n/a**(n/a): p. 2200234.

90. Senthilkumar, R., S. Vaidyanathan, and B. Sivaraman, *Thermal Analysis of Heat Pipe Using Taguchi Method*. International Journal of Engineering Science and Technology, 2010. **2**.
91. Liu, M., et al., *Beyond hydrophobicity: how F4-TCNQ doping of the hole transport material improves stability of mesoporous triple-cation perovskite solar cells*. Journal of Materials Chemistry A, 2022. **10**(21): p. 11721-11731.
92. Hu, L., et al., *High efficiency perovskite solar cells with PTAA hole transport layer enabled by PMMA:F4-TCNQ buried interface layer*. Journal of Materials Chemistry C, 2022. **10**(26): p. 9714-9722.
93. Wang, Q., C. Bi, and J. Huang, *Doped hole transport layer for efficiency enhancement in planar heterojunction organolead trihalide perovskite solar cells*. Nano Energy, 2015. **15**: p. 275-280.
94. Xie, Y.-M., et al., *Understanding the role of interconnecting layer on determining monolithic perovskite/organic tandem device carrier recombination properties*. Journal of Energy Chemistry, 2022. **71**.
95. Guchhait, A., et al., *Over 20% Efficient CIGS –Perovskite Tandem Solar Cells*. ACS Energy Letters, 2017. **2**.





จุฬาลงกรณ์มหาวิทยาลัย  
**CHULALONGKORN UNIVERSITY**

## VITA

**NAME** Kwanruthai Butsriruk

**DATE OF BIRTH** 11 May 1989

**PLACE OF BIRTH** Roi-Et, Thailand

**INSTITUTIONS  
ATTENDED** Chulalongkorn University

**AWARD RECEIVED** An outstanding poster entitled of Siam Physics Congress 2019 in the topic of Effects of anti-solvent in the two-step fabrication of absorber layer in perovskite solar cells.



จุฬาลงกรณ์มหาวิทยาลัย  
CHULALONGKORN UNIVERSITY